A DIFFUSIVE CRACK MODEL FOR FIBER REINFORCED POLYMER COMPOSITES

A THESIS SUBMITTED TO
THE GRADUATE SCHOOL OF NATURAL AND APPLIED SCIENCES
OF
MIDDLE EAST TECHNICAL UNIVERSITY

BY

FUNDA AKSU DENLI

IN PARTIAL FULFILLMENT OF THE REQUIREMENTS
FOR
THE DEGREE OF DOCTOR OF PHILOSOPHY
IN
MECHANICAL ENGINEERING

JULY 2020

Approval of the thesis:

A DIFFUSIVE CRACK MODEL FOR FIBER REINFORCED POLYMER COMPOSITES

submitted by **FUNDA AKSU DENLI** in partial fulfillment of the requirements for the degree of **Doctor of Philosophy in Mechanical Engineering Department, Middle East Technical University** by,

Prof. Dr. Halil Kalıpçılar
Dean, Graduate School of **Natural and Applied Sciences** ______________

Prof. Dr. M. A. Sahir Arıkan
Head of Department, **Mechanical Engineering** ______________

Assoc. Prof. Dr. Hüsnü Dal
Supervisor, **Mechanical Engineering, METU** ______________

Examining Committee Members:

Prof. Dr. Demirkan Çöker
Aerospace Engineering Dept., METU ______________

Assoc. Prof. Dr. Hüsnü Dal
Mechanical Engineering Dept., METU ______________

Assoc. Prof. Dr. Ercan Gürses
Aerospace Engineering Dept., METU ______________

Assist. Prof. Dr. Omer Music
Mechanical Engineering Dept., TED University ______________

Assist. Prof. Dr. Eralp Demir
Faculty of Engineering and Natural Sciences, Sabancı University ______________

Date:

I hereby declare that all information in this document has been obtained and presented in accordance with academic rules and ethical conduct. I also declare that, as required by these rules and conduct, I have fully cited and referenced all material and results that are not original to this work.

Name, Surname: Funda Aksu Denli

Signature :

ABSTRACT

A DIFFUSIVE CRACK MODEL FOR FIBER REINFORCED POLYMER COMPOSITES

Aksu Denli, Funda
Ph.D., Department of Mechanical Engineering
Supervisor: Assoc. Prof. Dr. Hüsnü Dal

July 2020, 98 pages

Recently, classical fracture mechanics approaches based on Griffith type sharp crack topologies have left the stage to diffusive crack approaches or the so called phase field models. Crack initiation and propagation is based on the variational principles for energy minimization leading to symmetric set of algebraic equations.

In this thesis, which is the first attempt to model failure of engineered composites using an anisotropic crack phase–field approach, Fiber Reinforced Polymer (FRP) specific anisotropic phase field model is developed in the light of the previous studies on isotropic brittle materials and anisotropic materials like biological tissues. It started with the continuous formulation of the variational principle for the multi-field problem manifested through the deformation map and the crack phase-field at finite strains which leads to the Euler–Lagrange equations of the coupled problem. In particular, the coupled balance equations derived render the evolution of the anisotropic crack phase-field and the balance of linear momentum. In addition, a novel energy-based anisotropic failure criterion is proposed which regulates the evolution of the crack phase-field. Distinct failure processes for the ground matrix and the fibers are mod-

elled by additively decomposing the energetic force, driving force for the damage, into isotropic and anisotropic parts. Distinct fracture energies were introduced for isotropic and anisotropic parts and anisotropic damage field interpretation is used for the dispersed damage field. In addition, an anisotropic geometric resistance expression has been added to the theory, which regulates the crack length scale distribution in different directions, to ensure that geometric constraints are taken into account in the direction of crack propagation. The coupled problem is solved using a one-pass operator-splitting algorithm composed of a mechanical predictor step that updates the displacement field and a crack evolution step that updates the damage field.

Representative numerical examples are devised for crack initiation and propagation in Carbon-Fiber-Reinforced Polymeric (CFRP) composites. Model parameters are obtained by fitting the set of experimental data reported in the literature to the predicted model response; the finite element results capture the effect of anisotropy in stiffness and strength both qualitatively and quantitatively. The proposed approach and its algorithmic implementation validated by Mixed Mode Bending (MMB) test results of APC2-prepreg unidirectional (UD) laminate. The success of the model in capturing different modes of failure and the ability to simulate interface effects have been demonstrated for double fix–end supported CFRP composite beam subjected to transverse load.

Keywords: fracture, failure, fiber–reinforced polymers, FRP composites, crack phase–field model, anisotropic failure criterion

ÖZ

LİFLE GÜÇLENDİRİLMİŞ POLİMER KOMPOZİTLER İÇİN YAYGIN ÇATLAK MODELİ GELİŞTİRİLMESİ

Aksu Denli, Funda
Doktora, Makina Mühendisliği Bölümü
Tez Yöneticisi: Doç. Dr. Hüsnü Dal

Temmuz 2020 , 98 sayfa

Son yıllarda Griffith teorisine bağlı keskin çatlak modeline dayalı kırıllma mekaniği teorileri yerini yaygın çatlak modellerine bırakmaya başlamıştır. Yaygın çatlak teorileri yırtılmanın başlangıcının ve ilerlemesinin global enerji minimasyonu prensiplerine bağlı olarak hesaplanmasina dayanir. Yaygın çatlak modelleri arasında faz alani modeli; modüler olması, sürekli ortamlar mekaniği problemlerinin çözümünde sıkça kullanılan sonlu elemanlar yöntemi ile rahatça modellenebilmesi, varyasyonel prensiplere dayanması ve çözüm algoritmalarının simetrik cebirsel sistemlerden oluşması itibariyle ilgi çekmektedir.

Anizotropik çatlak faz alanı yaklaşımı kullanılarak, üretilmiş kompozitlerin kopmasını modellemeye yönelik ilk girişim olan bu tezde, geçmişte izotropik kırılgan malzemeler ve anizotrop biyolojik dokular üzerine geliştirilmiş yaygın çatlak modelleri temel alınarak lifle güçlendirilmiş polimer kompozit yapılara özel faz alanı çatlak modeli geliştirilmiştir. Öncelikle, sonlu uzamalardaki deformasyonlardan ve çatlak faz alanından kaynaklı çok alanlı problemin varyasyonel prensibinin sürekli formulasyonu ve buna bağlı Euler-Lagrange denklemleri elde edilmiştir. Özellikle, türetilen

birleştirilmiş denge denklemleri, anizotropik çatlak faz alanının oluşumunu ve doğrusal momentum dengesini vermektedir. Ek olarak, çatlak faz alanının oluşumunu düzenleyen enerji bazlı yeni bir anizotropik kopma kriteri önerilmiştir. Bu bağlamda matris ve liflerin yırtılma/kopma durumları enerjetik kuvvetin (hasara sebep olan kuvvet) izotropik ve anizotropik kısımlara ayrılması ile modellenmiştir. İzotropik ve anizotropik kısımlar için farklı kırılma enerjileri takdim edilmiş, ve yaygın çatlak alanı lif yönünü dikkate alacak şekilde anizotropik olarak modellenmiştir. Ayrıca çatlak ilerleme yönünde geometrik kısıtların da dikkate alınmasını sağlamak amacıyla koda geometrik direnç ifadesi ve farklı yönlerde çatlak uzunluğu ölçek dağılımını düzenleyen anizotropi parametresi de eklenmiştir. Birleştirilmiş problem, mekanik bir öngörme adımı ve bir çatlak oluşumu adımından oluşan tek geçişli bir operatör-bölme algoritması kullanılarak çözülmektedir.

Kod sonlu eleman uygulamalarında kullanılabilir hale getirildikten sonra, karbon fiber takviyeli polimer kompozitlerde çatlak başlangıcı ve yayılımı için örnek niteliğindeki sayısal örnekler geliştirilmiştir. Ayrıca, kodun geçerliliği, tek yönlü APC2-prepreg katmanlarından oluşmuş kompozite ait karışık mod bükme test sonuçlarına göre kontrol edilmiştir. Modelin farklı çatlak yayılma modlarını yakalamadaki başarısı ve arayüz etkilerini simüle etme yeteneği ise lifle güçlendirilmiş polimer kompozit krişin enine yükleme testi ve analiz sonuçları arasındaki benzerlik ile kanıtlanmıştır.

Anahtar Kelimeler: çatlak, kopma, lifle güçlendirilmiş polimer, FRP kompozitler, yaygın çatlak modeli, anizotrop kopma kriteri

To my family

ACKNOWLEDGMENTS

The study presented in this thesis was carried out between 2016-2020. On this occasion, I would like to thank the people who supported me in different ways during this time. First of all, I would like to express my sincere gratitude to my advisor Assoc. Prof. Dr. Hüsnü Dal for his support and guidance besides his patience and encouragement. I would like to extend my deep thanks to Prof. Dr. Mustafa İlhan Gökler, who encouraged me to join METU for my PhD. studies and for his guidence in all matters. I would like to thank Prof. Dr. Demirkan Çöker and Assoc. Prof. Dr. Ercan Gürses for accepting to be in my thesis monitoring committee and for their interest.

I would like to thank to my colleagues at the Institute, Osman Gültekin and Kemal Açıkgöz for their team work and support, and I also want to thank to Latif Karacar from student affairs for his help and care during these eight years.

I want to thank all my colleagues at work (ATB team) for their friendship, mental support and peaceful and pleasant working environment they provide, they have a very special place in my heart.

Last but not least, I would like to express my sincere gratitude to my parents, Belma and Kamil Aksu, for their endless support. It was really hard to work full-time in the industry, having two children and an officer husband who was mostly away from home because of the duty and managing my doctoral studies, I would never have been able to do this without their support. Mum you are the best. I would like to thank my husband, even though he was away he tried to support me every step I take and helped me as much as he can and special thanks to my children, Deniz and Derin Denli, for adding purpose and happiness to my life, I love you so much.

TABLE OF CONTENTS

LIST OF TABLES

TABLES

LIST OF FIGURES

FIGURES

LIST OF ABBREVIATIONS

Multi-Word Terms

FRP	Fiber reinforced polymer
CFRP	Carbon fiber reinforced polymer
MMB	Mixed mode bending
UD	Uni–directional
1D	One-dimensional
3D	Three-dimensional

Operators

$\mathrm{Arg}[\bullet]$	Argument of a function
$\mathrm{cof}[\bullet]$	Cofactor
$\det[\bullet]$	Determinant
$\mathrm{div}[\bullet]$	Divergence in spatial domain
$\mathrm{DIV}[\bullet]$	Divergence in material domain
$\Delta[\bullet]$	Laplacian
$\inf[\bullet]$	Infimum of a set of quantities
$\sup[\bullet]$	Supremum of a set of quantities
$\mathrm{sym}\,[\bullet]$	Symmetric part of a tensor, i.e. $\mathrm{sym}[\bullet] = \frac{1}{2}[[\bullet] + [\bullet]^T]$
$\mathrm{skw}\,[\bullet]$	Skew part of a tensor, i.e. $\mathrm{skw}[\bullet] = \frac{1}{2}[[\bullet] - [\bullet]^T]$
$\mathrm{tr}[\bullet]$	Trace operator
$\langle[\bullet]\rangle^2$	Macaulay brackets
$\mathscr{L}_v[\bullet]$	Lie derivative
$\delta_{[\bullet]}$	Variation with respect to $[\bullet]$
$\partial_{[\bullet]}$	Differential operator, i.e. differentiation with respect to $[\bullet]$

$\nabla[\bullet]$	Gradient operator
$\nabla_X[\bullet]$	Gradient operator with respect to reference $\boldsymbol{X}$ coordinates
$\nabla_x[\bullet]$	Gradient operator with respect to spatial $\boldsymbol{x}$ coordinates
$\boldsymbol{\varphi}^*[\bullet]$	Pull–back operator
$\boldsymbol{\varphi}_*[\bullet]$	Push–forward operator
$[\bullet]^T$	Transpose operator
$[\bullet]^{-1}$	Inverse operator
$\cdot$	Dot product
$:$	Double contraction, a.k.a double dot product
$\times$	Vector product
$\otimes$	Dyadic product

Continuum Mechanics and Constitutive Modelling

$\mathcal{B}$	Unloaded state of the body (reference configuration)
$\partial\mathcal{B}$	Boundary of unloaded body
$\mathcal{S}$	Loaded state of the body (current configuration)
$\partial\mathcal{S}$	Boundary of loaded body
$\boldsymbol{G}$	Reference metric tensor
$\boldsymbol{g}$	Spatial metric tensor
$\boldsymbol{X}$	Position vector at reference state
$\boldsymbol{x}$	Position vector at current state
$\boldsymbol{\varphi}_t$	Deformation function
$\boldsymbol{F}$	Deformation gradient
$\boldsymbol{R}$	Rotation tensor
$\boldsymbol{U}$	Right stretch tensor
$\boldsymbol{V}$	Left stretch tensor
J	Determinant of deformation gradient
$\mathrm{d}\boldsymbol{X}$	Lagrangian line element

$\mathrm{d}\boldsymbol{x}$	Eulerian line element
$\mathrm{d}\boldsymbol{A}$	Area vector of material surface
$\mathrm{d}\boldsymbol{a}$	Area vector of spatial surface
dV	Reference volume element
dv	Spatial volume element
$\boldsymbol{C}$	Right Cauchy–Green tensor
$\boldsymbol{b}$	Left Cauchy–Green tensor
$\boldsymbol{E}$	Green–Lagrangian strain tensor
$\boldsymbol{A}$	Almansi strain tensor
λ_α	Principle stretch
$\boldsymbol{N}_\alpha$	Lagrangian eigenvector
$\boldsymbol{n}_\alpha$	Lagrangian eigenvector
$\boldsymbol{I}_\alpha$	Invariants
$\boldsymbol{f}_0$	Reference unit vector for the fiber orientation
$\boldsymbol{f}'_0$	Reference unit vector for the fiber orientation of second fiber family
$\boldsymbol{f}$	Spatial vector for the fiber orientation
$\boldsymbol{f}'$	Spatial vector for the fiber orientation of second fiber family
$\boldsymbol{A}$	Lagrangian structure tensor
$\boldsymbol{A}'$	Lagrangian structure tensor for second fiber family
$\boldsymbol{A}_f$	Eulerian structure tensor
$\boldsymbol{A}'_f$	Eulerian structure tensor for second fiber family
λ_f	Stretch of the fiber
$\boldsymbol{L}$	Material velocity gradient
$\boldsymbol{l}$	Spatial velocity gradient
$\boldsymbol{d}$	Rate of deformation tensor
$\boldsymbol{w}$	Spin tensor

$\boldsymbol{u}$	Displacement
$\boldsymbol{v}$	Velocity
$\boldsymbol{a}$	Acceleration
$\boldsymbol{\varepsilon}$	Strain tensor
dA	Undeformed area element
da	Deformed area element
$\boldsymbol{N}$	Unit outward normal in material configuration
$\boldsymbol{n}$	Unit outward normal in spatial configuration
$\boldsymbol{t}$	Traction vector
$\boldsymbol{\sigma}$	Cauchy stress tensor
$\boldsymbol{\tau}$	Kirchhoff stress tensor
$\overline{\boldsymbol{T}}$	Nominal traction vector
$\boldsymbol{P}$	First Piola–Kirchhoff stress tensor
$\boldsymbol{S}$	Second Piola–Kirchhoff stress tensor
$\boldsymbol{T}$	Lagrangian traction vector
$\boldsymbol{q}$	Heat flux vector
h	Heat flux
r	Heat source per unit mass
m	Mass
ρ	Density
$\boldsymbol{b}$	Body forces
$\mathcal{I}$	Linear momentum
$\mathcal{D}_0$	Angular momentum
K	Kinetic energy
E	Internal energy per unit mass
H	Entropy per unit mass
Γ	Entropy production per unit mass

e	Internal energy
η	Entropy
γ	Entropy production
ρ_0	Material density
R	Material heat generation
$\boldsymbol{B}$	Material body loads
$\boldsymbol{Q}$	Material heat flux vector
θ	Temperature
$\mathcal{D}$	Dissipation
$\mathcal{D}_{loc}$	Local dissipation
$\mathcal{D}_{con}$	Conductive (non–local) dissipation
Ψ	Helmholtz free energy
d	Crack phase–field
$\Gamma(d)$	Sharp crack surface
$\Gamma_l(d)$	Regularized crack surface
$\delta(x)$	Kronecker delta function
l	Length scale parameter
$\gamma(d, \nabla d)$	Isotropic crack surface density function
$\gamma(d, \nabla d; \boldsymbol{\mathcal{L}})$	Anisotropic crack surface density function
$\boldsymbol{\mathcal{L}}$	Anisotropic structure tensor
w_{f_0}	Anisotropy parameter
w'_{f_0}	Anisotropy parameter for second fiber family
Π_η	Viscous rate–type potential
$\mathcal{E}$	Rate of energy storage functional
f	Scalar energetic force
$g(d)$	Degradation function
$\mathcal{D}_\eta$	Viscous regularized dissipation functional

η	Artificial viscosity
χ	Scalar viscous over–stress functional
β	Local driving force
$\mathcal{P}$	External power functional
$\overline{\mathcal{H}}$	Crack driving source term
g_{c}	Critical fracture energy
λ	First Lamé constant
μ	Second Lamé constant (shear modulus)
μ_{f}	Stress–like parameter associated with fibrous content
μ'_{f}	Stress–like parameter associated with fibrous content of second fiber family
$\mathbb{C}$	Elasticity tensor
$\mathbb{M}$	Fourth–order structure tensor
g_{c}^{iso}	Critical fracture energy of the ground matrix
g_{c}^{ani}	Critical fracture energy of the fibrous content
$g_{\mathrm{c}}^{\prime ani}$	Critical fracture energy of the fibrous content of second fiber family

CHAPTER 1

INTRODUCTION

The aim of this study is to present a crack phase–field approach for anisotropic continua to model, in particular, fracture of FRP composites. Starting with the variational formulation of the multi–field problem of fracture in terms of the deformation and the crack phase–fields, the governing equations feature the evolution of the anisotropic crack phase–field and the balance of linear momentum, presented for finite and small strains. A recently proposed energy–based anisotropic failure criterion is incorporated into the model with a constitutive threshold function regulating the crack initiation in regard to the matrix and the fibers in a superposed framework. Representative numerical examples are shown for the crack initiation and propagation in UD FRP composites under Mode–I, Mode–II, MMB and transverse static loading. Mode–I and Mode-II analyses are performed mainly to show the influence of the fiber orientation to the failure load and the crack path. Then the method is validated by a real MMB test where we also demonstrate the effect of anisotropy parameter, details of these studies are published in [16] and [17]. Then, to illustrate the interface effects and the crack formations between different composite layups transverse loading of a CFRP beam analysis is performed. In all analyses model parameters are obtained from experimental data. The associated finite element results are able to capture anisotropic crack initiation and growth in UD fiber-reinforced composite laminates.

1.1 Overview and Background

FRP composites consist of matrix and fiber and, as the name suggests, are polymer materials reinforced with fibers such as glass, carbon or aramid fiber. Matrix is a polymeric substance and works as a binder keeping fibers together by surrounding them, and it also provides the fibers protection from environmental damages [12, 30].

In FRP composites, fibers carry the loads and matrix distributes the loads to the fibers and transfer the stresses inbetween. Mechanical properties of the FRP composites depend on *(i) type of fiber and matrix (their modulus and compatibility), (ii) properties of the interface between the fiber and the matrix resin, (iii) resin content or fiber volume fraction, and (iv) orientations of fibers.* If the resin amount is high, "resin rich", composite can crack due to lack of enough fiber support. On the other hand, if the composite is a "resin starved" there can be void zones which weaken the composite [30, 54]. The sequence and orientations of the fibers also effect the strength of the FRP composite. For example; in UD FRP composites the longitudinal stiffness is much higher than the transverse stiffness. The longitudinal modulus is more influenced by fiber modulus and increases proportional to fiber volume fraction. In transverse direction, fibers are not the primary load carrying members and due to this, the transverse modulus is more influenced by matrix modulus. For UD FRP composites transverse modulus is always lower than the longitudinal modulus [32].

Compared to metals, FRP composites are seen to demonstrate much more complex mechanical behaviour. While the conventional materials used in industry are homogeneous and isotropic, FRP composites have heterogeneous micro-structure, large differences between constituent material properties, interfaces between constituents and plies and an anisotropy related to directions of the reinforcements. FRP composites generally exhibit brittle material response where the failure occurs at low strain values without any significant macroscopic yielding. They show very different and variable fracture and failure modes under various loading conditions. Failure can happen by fiber breakage, matrix crazing and cracking, fiber-matrix de-bonding, de-lamination and inter-ply separation [20, 32, 54]. Fiber breakage happens when the FRP composite lamina is tensioned in fiber/longitudinal direction. After fiber breakage different micro-failure modes such as de-bonding and matrix cracking and breakage of other fibers can follow. When the lamina is loaded in tension in transverse direction fibers are no longer the main load carrying members and due to this, the main failure modes are the matrix and fiber-matrix interface cracking. For compressive loading of lamina in longitudinal direction the most commonly seen failure mode is the matrix shear parallel to the fiber direction, and for compressive loading in traverse direction the matrix cracks which move around the fibers [32, 54]. De-lamination failure mode happens when more than one lamina stack together (laminate) and experience cyclic fatigue loading or impact that leads to the separation of laminas from each other [41–43, 48]. Some of those failure modes demonstrated in Fig. 1.1, Fig. 1.2 and Fig. 1.3.

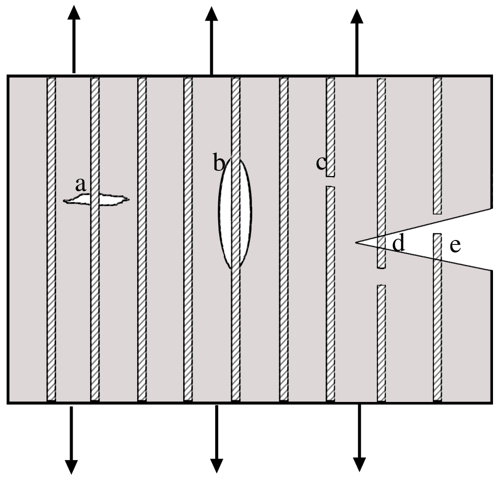

Figure 1.1: Possible micro-failure modes in longitudinal tension; a)matrix-crack, b) matrix-debonding, c)fiber-cracture, d)bridging e)fiber-pull-out

Since the introduction of composite materials in the 1960's great success has been achieved in estimating the effective micromechanical properties of composites, the respective homogenized response and the plate theories for laminates. However, theories pertaining to the fracture of composite materials are not on par with the afore–mentioned theories in terms of their applicability and accuracy. Although a lot of efforts have been made over five decades, the prediction of composite failure still remains largely unsolved with plenty of uncertainties, as reviewed by Talreja [55].

Regarding FRPs, the failure mechanisms are, in general, related to *(i) the mechanical behavior of the individual lamina and laminate as a whole and (ii) the direction of the loading.* Compared with steel and other more conventional materials, the failure mechanism of FRP composites is much more complex and its prediction presents a tremendous challenge for engineers and researchers as they possess an inherent heterogeneity with distinct interfaces in their structure. The model approaches for

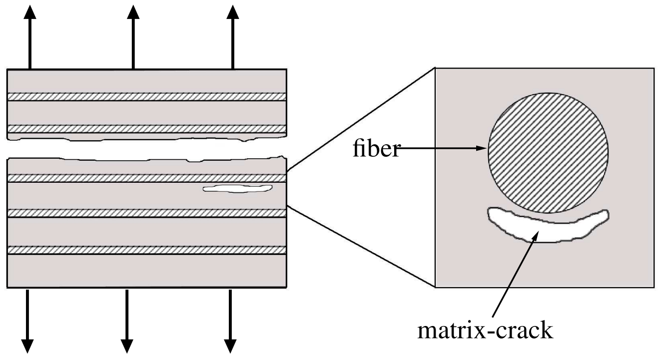

Figure 1.2: Possible micro-failure modes for transverse tensile loading

the crack initiation and progression in composite materials can be divided into two categories: one is based on strength criteria (i.e., failure at a material point) and the other one is based on energy criteria (i.e., surface formation), see, e.g., Talreja & Singh [54].

According to strength–based criteria, micro-cracks form when the local stress (strain) state in a ply reaches a critical level. To date, several strength–based failure criteria that are rooted in metal fracture have been proposed for composite materials namely, Tsai–Hill [6,27], Tsai–Wu [56], Hashin [25] and Cuntze [15], just to mention a few. Expressed by quadratic polynomials, they involve strength values as material constants that need to be determined from experimental data. In principle, failure manifests when the elastic response in any combination of the stress components that exceed a threshold given by the respective criterion. Unlike the early maximum stress and strain criteria, the theories by Tsai–Hill, Tsai–Wu and Hashin take into account the possible stress interactions at failure. However, their use also leads to other issues. The Tsai–Hill criterion is based on the Hill criterion, which is basically an anisotropic extension of the von–Mises [39] yield theory developed for isotropic materials such as metals. The predicted yield stress therein is the same in tension and compression, an appropriate conclusion for orthotropic metal sheets; however, such an assumption is far–fetched in regard to UD composites as the mechanisms characterizing the

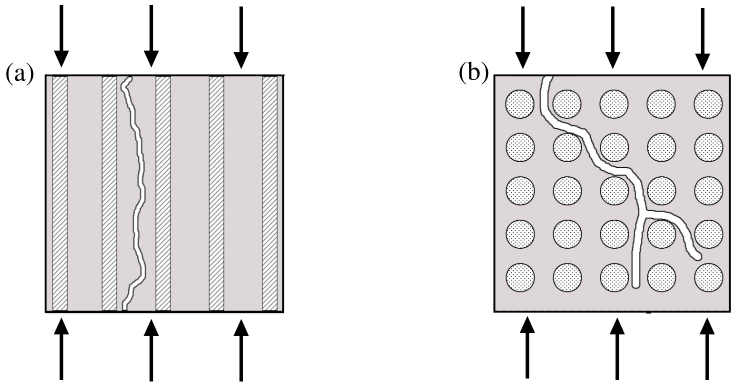

Figure 1.3: Shear failure (a) in longitudinal compression and (b) in transverse compression

failure under tension and compression are quite different from each other. In fact, a cluster of failed fibers in a cross–section is involved under tension and accompanied by some splits of fibers linking the neighboring cross–sections, whereas a local kink band facilitated by the micro–buckling deformation modes results in the failure of the composite under compressive loads, see, e.g., Argon [5]. Tsai-Wu account for unequal strengths in tension and compression that evokes the Bauschinger effect. This criterion assumes a scalar–valued function of stress components in regard to the failure surface characterized by an ellipsoid. The problem associated with this criterion is how to determine the inclination of the ellipsoid as the biaxial components of the strength tensor do not have a unique value, but hinge on the stress state. To overcome this difficulty, Hashin suggested many piece-wise smooth surfaces, each representing a distinct failure mode. In fact, the fiber failure in the criterion is decoupled from the matrix failure. Yet the problem of ascertaining the strength constants for compressive modes render the theory rather impractical. Later, Puck & Schürmann [45] proposed a more justifiable failure theory in the sense of model constants.

All of the afore–mentioned criteria regard the failure as a single event and consider composites as homogeneous solids. Besides, the failure plane is not explicitly influenced by the existence of fibers, i.e. the crack does not cut across the fibers. Nor do the distribution of fibers (uniform or nonuniform) and the nature of the matrix–fiber bond alter the critical tractions and the orientation of the crack surface. Furthermore, they are created on the basis of the traditional strength of the materials approach from the structural design aspect, and can only impart knowledge about the critical design points where the failure may occur. They fall short of describing differences in the crack initiation (as a material point failure process) and the crack propagation (as a surface growth process). As a consequence, the effect of ply thickness on the transverse cracking cannot be properly accounted by such criteria. Other problems are the impossibility of analytical characterization of local stress states except for a few cases and the conflict between the experimental data and the strength–based estimations, see Talreja & Singh [54].

Energy–based criteria originate from linear elastic fracture mechanics where the crack starts to grow when the energy release rate G reaches a critical value G_c expressed by the equilibrium $G = G_c$, as introduced by Griffith [21]. In a multiple cracking of a composite laminate, the progression of a crack located in between the plies is arrested at the interface and any further input of energy to the laminate leads to the formation of more ply cracks occurring elsewhere. In such a case, the conventional fracture mechanics approach requires modifications, e.g., the concept of finite fracture mechanics and variational stress analysis, which was among others presented by Hashin [26] and Nairn [40]. Aside from that, a strain energy–based failure criterion was suggested by Wolfe & Butalia [59] for a wide variety of UD and symmetric laminates under biaxial loading.

The cohesive zone modeling (CZM) appears to be one of the most prevalent approaches used to mimic the mechanical failure of laminae which was presented by many including Turon et al. [57], Yang & Cox [60], Naghipour et al. [41] and Zhao et al. [62] for uni– and multi–directional composite laminates in Mode–I and Mode–II fracture. Likewise, there have been several successful applications of the extended finite element method (XFEM) by, e.g., Grogan et al. [22], Wang et al. [58] and Yazdani et al. [61] on the delamination of composite materials. Recent revelations by Dal et al. [16], Reinoso et al. [47], Alessi & Freddi [2] and Arterio et al. [4] highlight an alternative approach, namely the crack phase–field modeling to predict damage and failure of composite laminates. In contrast to CZM and XFEM, the crack phase–

field approach utterly ignores the realization of discontinuities as the 2D crack surface smears out in a volume domain in 3D, which is determined by a specific field equation alongside the balance of linear momentum describing the elasticity of the solid. The well-known limitations of the classical fracture mechanics, e.g., curvilinear crack paths, crack kinking, branching angles, and multiple cracking are surmounted through a variational principal of the minimum energy, see Francfort & Marigo [19].

1.2 Phase–Field Approach

The thermodynamically consistent and algorithmically robust formulations of phase–field models were introduced in the seminal works by Miehe et al. [34, 35]. The approach is modular and can be applied to non–standard solids exhibiting complex cracking mechanisms under multiphysics phenomena, see, e.g., Miehe et al. [36–38]. Ductile failure of elastoplastic materials is treated in Ambati et al. [3] and Borden et al. [8]. Anisotropic crack phase–field evolution has recently been considered by, e.g., Li et al. [31] and Teichtmeister et al. [53], which is based on the extended Cahn-Hilliard model, see Cahn and Hilliard [11], to account for the anisotropic surface energy emanating from the preferred directions in materials. Apart from that Clayton and Knap [13] and Nguyen et al. [44] proposed anisotropic phase–field models for polycrystals. The approach of Schreiber et al. [49] uses an anisoptropic geometric resistance to failure in the sense of Gültekin et al. [23].

1.3 Motivation and Contribution

For materials such as soft biological tissues and composite laminates, the anisotropic fracture is not only a geometrical phenomenon but also a mechanical event arisen from the fibrous content embedded in an otherwise isotropic matrix material, necessitating the use of an anisotropic crack driving force apart from directional geometric resistance. Hence, the current study continuation of Dal et al. [16] and follows the footsteps of the previous contributions by Gültekin et al. [23, 24] in which the anisotropic crack phase–field at finite strains was introduced. Incorporated was also a novel energy–based failure criterion based on the distinction of fibrous and matrix contributions to the elastic mechanical response. The current study, however, examines the fracture of the FRPs composed of a polymer matrix reinforced with fibers.

1.4 Scope and Outline

This thesis is organized as follows. Basics of continuum mechanics along with the local balance laws and local and non–local dissipation equations are given in chapter 2. Chapter 3 outlines the primary field variables with the corresponding finite strain kinematics and the diffusive features of the anisotropic crack phase–field. Chapter 4 is concerned with the rate–dependent variational formulation of the multi–field problem of fracture, both for finite and small–strain, resulting in the coupled balance equations. Chapter 5 focuses on the anisotropic hyperelastic constitutive response reflecting the elastic mechanical behavior of the composite in the Eulerian framework then by the linearization of the constitutive model, small strain equations are derived, too. A brief account of the energy–based anisotropic failure criterion is also provided. In chapter 6, the representative numerical examples exhibit the capabilities of the model with regard to a standard problem of a transversely isotropic single edge–notched specimen under Mode–I and Mode–II loading scenarios and a realistic test case for a UD laminate withstanding MMB and CFRP beam with $[0_5/90_3]_s$ configuration carrying the transverse load. Finally, chapter 7 summarizes the thesis work.

CHAPTER 2

BASICS OF CONTINUUM MECHANICS

This chapter gives basic concepts and interpretations in continuum mechanics such as basic deformation maps, deformation measures, strain and stress definitions and the invariant descriptions used in this study. Balance laws of thermomechanics and their local forms are reviewed, then the local and non-local definitions of the dissipation is given.

2.1 Kinematics

In this section some key notations related to the large stain kinematics of the continuum deformation and the small strain kinematic will be summarized.

2.1.1 Large Strain Kinematics

Here we start with the definition of reference configuration and spatial configuration of a body. In continuum mechanics, a body which is not subjected to any surface tractions or any body forces is defined as an unloaded body or a material body. This unloaded state of the body is considered as its reference configuration and denote by $\mathcal{B}$. This configuration is also called as Lagrangian configuration. Likewise the deformed state of the body at time t due to the applied loads is define as the current, spacial or Eulerian configuration of the body and denote by $\mathcal{S}$. $\partial\mathcal{B}$ and $\partial\mathcal{S}$ are the notations used for the boundaries of the unloaded and loaded bodies.

One can locally furnish coordinate systems for both reference and spatial configurations. These coordinate systems are generally non-orthogonal but equipped with the reference metric $\boldsymbol{G} = G_{AB}$ and the spatial metric $\boldsymbol{g} = g_{ab}$. Here upper-case letter indices used for Lagrangian entity where lower-case letter used for Eulerian entity. The both metric tensors reduce to the Kronecker deltas $\boldsymbol{G} = \delta_{AB}$ and $\boldsymbol{g} = \delta_{ab}$ in the case of Cartesian coordinate systems which is the case for this study.

$$\boldsymbol{G} = \delta_{AB}\boldsymbol{E}^A \otimes \boldsymbol{E}^B, \qquad \boldsymbol{g} = \delta_{ab}\boldsymbol{e}^a \otimes \boldsymbol{e}^b \tag{2.1}$$

An unloaded body $\mathcal{B}$ composed of infinitely number of material points. These points occupy geometrical positions in 3D Euclidean Space R^3 and any arbitrary point on the unloaded body can be labelled by with its position vector $\boldsymbol{X}$, and its new position on the current state at time t by $\boldsymbol{x}$. The deformation function $\boldsymbol{\varphi}_t$ is one–to–one and maps the material point $\boldsymbol{X}$ on its deformed spatial configuration $\boldsymbol{x} = \boldsymbol{\varphi}_t(\boldsymbol{X})$ at time t.

While $\boldsymbol{\varphi}_t$ maps the point position, the deformation gradient $\boldsymbol{F} = \nabla\boldsymbol{\varphi}_t(\boldsymbol{X})$, maps the infinitesimal Lagrangian line element $\mathrm{d}\boldsymbol{X}$ onto its Eulerian counterpart $\mathrm{d}\boldsymbol{x} = \boldsymbol{F}\mathrm{d}\boldsymbol{X}$, see Figure 2.1. The gradient operators $\nabla(\bullet)$ and $\nabla_x(\bullet)$ denote the gradient operator with respect to the reference $\boldsymbol{X}$ and the spatial $\boldsymbol{x}$ coordinates, respectively. $\boldsymbol{F}$ is a two–point tensor that contains both Eulerian and Lagrangian points and its components are written as $F_{aA} = \partial x_a / \partial X_A$. Since $\boldsymbol{F}$ is a second order tensor, it works as a operator. It can both rotate, lengthen and shorten the line element it operates on. Thus, the deformation gradient can be decomposed into pure stretch and pure rotation, which is called as the polar decomposition of the deformation gradient.

$$\boldsymbol{F} = \boldsymbol{R}\boldsymbol{U} = \boldsymbol{V}\boldsymbol{R} \tag{2.2}$$

where $\boldsymbol{R}$ is an orthogonal tensor describing rotation, $\boldsymbol{U}$ and $\boldsymbol{V}$ are the symmetric positive definite right and left stretch tensors, respectively. Similar to $\boldsymbol{F}$, $\boldsymbol{R}$ is a two–point tensor and right $\boldsymbol{U}$ and left $\boldsymbol{V}$ stretch tensors are Lagrangian and Eulerian objects. This means that a line element can be first stretched in the Lagrangian domain and then rotated to its position in the Eulerian domain or it can be first rotated to its position on the Eulerian domain, then stretched. The related maps are shown as following:

$$\begin{aligned} \text{Two point maps } (T_X\mathcal{B} \to T_x\mathcal{S}) : &\qquad \boldsymbol{F}, \boldsymbol{R} \\ \text{Lagrangian map } (T_X\mathcal{B} \to T_X\mathcal{B}) : &\qquad \boldsymbol{U} \\ \text{Eulerian map } (T_x\mathcal{S} \to T_x\mathcal{S}) : &\qquad \boldsymbol{V}. \end{aligned} \tag{2.3}$$

The determinant of $\boldsymbol{F}$ is taken to be positive ($J := \det \boldsymbol{F} > 0$) due to the fact that $\boldsymbol{\varphi}_t(\boldsymbol{X})$ is one–to–one function and the interpenetration of the material is ruled out throughout

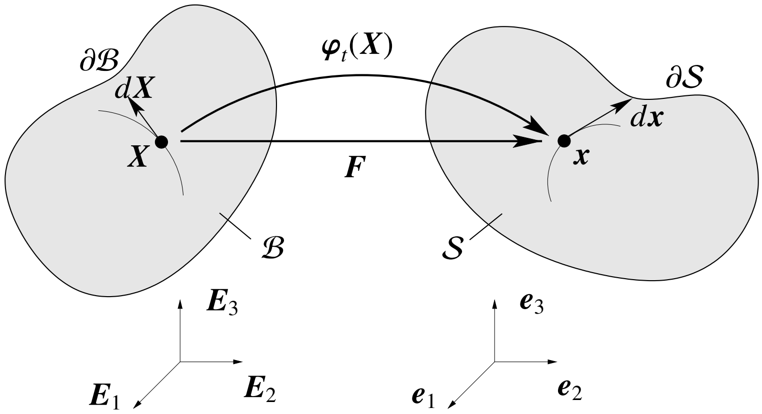

Figure 2.1: Left-hand side is the (undeformed) reference configuration $\mathcal{B}$ with a boundary description $\partial\mathcal{B}$, right-hand side is the deformed configuration $\mathcal{S}$ with a boundary $\partial\mathcal{S}$ as a result of deformation $\boldsymbol{\varphi}$.

the motion. J is the standard notion used for the determinant of $\boldsymbol{F}$. The fundamental maps in continuum mechanics, shown in Figure 2.2, are defined as *tangent map*, *area map* and *volume map* and their descriptions are:

$$\boldsymbol{F} : T_X\mathcal{B} \rightarrow T_x\mathcal{S} \qquad \mathrm{d}\boldsymbol{X} \mapsto \mathrm{d}\boldsymbol{x} = \boldsymbol{F}\mathrm{d}\boldsymbol{X} \tag{2.4}$$

$$\mathrm{cof}\,\boldsymbol{F} : T^*_X\mathcal{B} \rightarrow T^*_x\mathcal{S} \qquad \mathrm{d}\boldsymbol{A} \mapsto \mathrm{d}\boldsymbol{a} = \mathrm{cof}[\boldsymbol{F}]\mathrm{d}\boldsymbol{A} = J\boldsymbol{F}^{-T}\mathrm{d}\boldsymbol{A} \tag{2.5}$$

$$J : \mathcal{R}_+ \rightarrow \mathcal{R}_+ \qquad \mathrm{dV} \mapsto \mathrm{dv} = \det[\boldsymbol{F}]\mathrm{dV} = J\mathrm{dV}. \tag{2.6}$$

Here, the deformation gradient $\boldsymbol{F}$ linearly maps the line element $\mathrm{d}\boldsymbol{X}$ onto its spatial counterpart $\mathrm{d}\boldsymbol{x}$. Thus, $\boldsymbol{F}$ is termed as the *tangent map*. The cofactor $\mathrm{cof}[\boldsymbol{F}] = J\boldsymbol{F}^{-T}$ of the deformation gradient $\boldsymbol{F}$ given in equation 2.5 maps area vectors $\mathrm{d}\boldsymbol{A}$ of material surfaces onto area vectors $\mathrm{d}\boldsymbol{a}$ of the associated deformed spatial surfaces and this define as the *area map*. Finally, the third map given in equation 2.6 is the *volume map* and $J = \det \boldsymbol{F}$ characterizes the map of an infinitesimal reference volume element dV onto the associated spatial volume element dv. For a volume preserving (no volume change) deformation J is equal to 1 and if a material is defined as incompressible material the constraint $J = 1$ must be satisfied at each material point.

Stretch λ is another important kinematical quantity which define as the ratio of the length of the spatial vector $\mathrm{d}\boldsymbol{x}$ to the length of the its material counterpart $\mathrm{d}\boldsymbol{X}$.

$$\lambda = \frac{\|\,\mathrm{d}\boldsymbol{x}\,\|}{\|\,\mathrm{d}\boldsymbol{X}\,\|} = \frac{\sqrt{\mathrm{d}\boldsymbol{x}\cdot\mathrm{d}\boldsymbol{x}}}{\sqrt{\mathrm{d}\boldsymbol{X}\cdot\mathrm{d}\boldsymbol{X}}} = \frac{\sqrt{(\boldsymbol{F}\mathrm{d}\boldsymbol{X})\cdot(\boldsymbol{F}\mathrm{d}\boldsymbol{X})}}{\sqrt{\mathrm{d}\boldsymbol{X}\cdot\mathrm{d}\boldsymbol{X}}} = \frac{\sqrt{\mathrm{d}\boldsymbol{X}\cdot(\boldsymbol{F}^T\boldsymbol{F}\mathrm{d}\boldsymbol{X})}}{\sqrt{\mathrm{d}\boldsymbol{X}\cdot\mathrm{d}\boldsymbol{X}}} \tag{2.7}$$

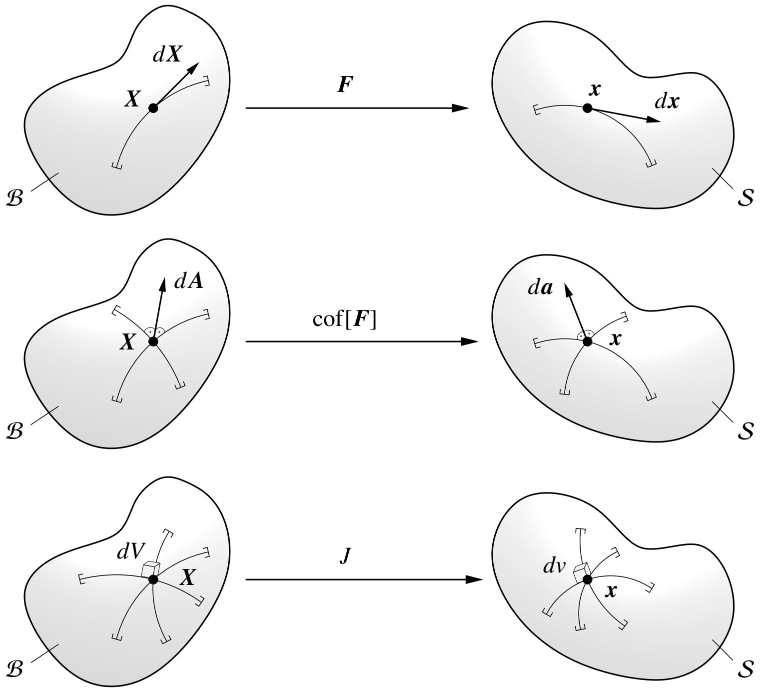

Figure 2.2: Fundamental maps

If $\mathrm{d}\boldsymbol{X}$ is chosen as a unit vector, the stretch can be expressed as;

$$\lambda = \sqrt{\mathrm{d}\boldsymbol{x} \cdot \mathrm{d}\boldsymbol{x}} = \sqrt{\mathrm{d}\boldsymbol{X} \cdot (\boldsymbol{F}^T \boldsymbol{F} \mathrm{d}\boldsymbol{X})} = \sqrt{\mathrm{d}\boldsymbol{X} \cdot \boldsymbol{C} \mathrm{d}\boldsymbol{X}} \tag{2.8}$$

where the product of $\boldsymbol{F}^T \boldsymbol{F}$ is the right Cauchy–Green tensor, denoted by $\boldsymbol{C}$.

The same expression in equation 2.8 can be written by using a metric tensor,

$$\begin{aligned} \lambda &= \sqrt{\mathrm{d}\boldsymbol{x} \cdot \boldsymbol{g} \mathrm{d}\boldsymbol{x}} = \sqrt{(\mathrm{d}x^a \boldsymbol{g}_a) \cdot g_{kl}(\boldsymbol{g}^k \otimes \boldsymbol{g}^l) \cdot (\mathrm{d}x^b \boldsymbol{g}_b)} = \sqrt{\mathrm{d}x^a g_{ab} \mathrm{d}x^b} \\ &= \sqrt{F^a_A \mathrm{d}X^A g_{ab} F^b_B \mathrm{d}X^B} = \sqrt{\mathrm{d}X^A F^a_A g_{ab} F^b_B \mathrm{d}X^B} \\ &= \sqrt{\mathrm{d}X^A C_{AB} \mathrm{d}X^B}, \end{aligned} \tag{2.9}$$

and since it is in the indicial form, the Cartesian components of $\boldsymbol{C}$ can be defined as $C_{AB} = F^a_A g_{ab} F^b_B$. This is the Lagrangian approach to define the stretch, and it also shows that $\boldsymbol{C}$ is a Lagrangian entity.

Similarly, the inverse stretch λ^{-1} can be defined by taking $\mathrm{d}\boldsymbol{x}$ as a unit vector and

$\| \mathrm{d}\boldsymbol{x} \| = 1$, which gives the Eulerian approach used to express the stretch.

$$
\begin{aligned}
\lambda^{-1} = \| \mathrm{d}\boldsymbol{X} \| = \sqrt{\mathrm{d}\boldsymbol{X} \cdot \boldsymbol{G}\mathrm{d}\boldsymbol{X}} &= \sqrt{\mathrm{d}X^A G_{AB} \mathrm{d}X^B} \\
&= \sqrt{\mathrm{d}x^a (F^{-1})^A_a G_{AB} (F^{-1})^B_b \mathrm{d}x^b} \\
&= \sqrt{\mathrm{d}x^a b^{-1}_{ab} \mathrm{d}x^b}
\end{aligned}
\tag{2.10}
$$

Equation 2.10 yields the left Cauchy–Green tensor $b^{-1}_{ab} = (F^{-1})^A_a G_{AB} (F^{-1})^B_b$, which is an Eulerian entity. Thus, the right and left Cauchy–Green tensors expressed by metric tensors are given as;

$$
\boldsymbol{C} = \boldsymbol{F}^T \boldsymbol{g} \boldsymbol{F}, \qquad \boldsymbol{b} = \boldsymbol{F} \boldsymbol{G}^{-1} \boldsymbol{F}^T. \tag{2.11}
$$

Even though the metric tensors are identity for Cartesian system, it is necessary to utilize these metric tensors as the maps from the tangent to normal spaces of the Lagrangian and Eulerian configurations to make the geometrical meaning of the right and left Cauchy Green Tensors more clear.

From geometrical point of view the right Cauchy Green tensor is interpreted as the pull back of current metric $\boldsymbol{g}$, and the inverse left Cauchy Green tensor as the push forward of the reference metric $\boldsymbol{G}$. Both are defined as following;

$$
\boldsymbol{C} = \boldsymbol{\varphi}^*(\boldsymbol{g}), \qquad \boldsymbol{b}^{-1} = \boldsymbol{\varphi}_*(\boldsymbol{G}) \tag{2.12}
$$

where superscript $\boldsymbol{\varphi}^*(\bullet)$ denote the pull–back and subscript $\boldsymbol{\varphi}_*(\bullet)$ denote the push–forward. The pull–back and push–forward operations are described as:

$$
\boldsymbol{\varphi}^*(\bullet) = \boldsymbol{F}^T(\bullet)\boldsymbol{F} \qquad \boldsymbol{\varphi}_*(\bullet) = \boldsymbol{F}^{-T}(\bullet)\boldsymbol{F}^{-1} \tag{2.13}
$$

As seen in the Figure 2.3, in Lagrangian setting, while the reference metric is $\boldsymbol{G}$, the current metric is defined by $\boldsymbol{C}$. On the other hand in the Eulerian setting, the reference metric is given by $\boldsymbol{b}^{-1}$ while the current metric is defined by $\boldsymbol{g}$. The comparison of these metric tensors in one configuration gives the strain definition at the related configuration. Thus, Green–Lagrangian and Almansi strain tensors are defined as:

$$
\begin{aligned}
\boldsymbol{E} &= \frac{1}{2}[\boldsymbol{C} - \boldsymbol{1}] \quad : \ \text{Green-Lagrangian Strain (Lagrangian setting)} \\
\boldsymbol{A} &= \frac{1}{2}[\boldsymbol{1} - \boldsymbol{b}^{-1}] \quad : \ \text{Almansi Strain (Eulerian setting)}
\end{aligned}
\tag{2.14}
$$

for the Lagrangian and Eulerian settings respectively. And each can be described as pull–back or push–forward of each other.

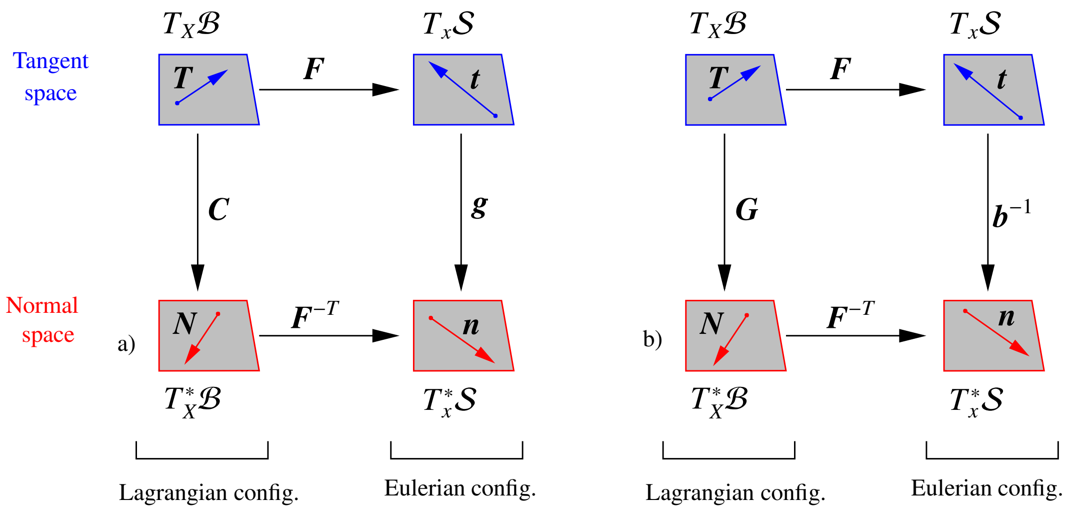

Figure 2.3: Definition of metric tensors. a) current metric in Lagrangian configuration $\boldsymbol{C} = \boldsymbol{F}^T \boldsymbol{g}\boldsymbol{F}$; b) reference metric in Eulerian configuration $\boldsymbol{b}^{-1} = \boldsymbol{F}^{-T}\boldsymbol{G}\boldsymbol{F}^{-1}$.

Cayley–Hamilton Theorem

The eigenvalues of an any second order tensor $\boldsymbol{A}$ can be obtained from its characteristic equation, which is the solution of the eigenvalue problem. The eigenvalue problem states that:

$$\boldsymbol{A}\boldsymbol{N}_\alpha = \lambda_\alpha \boldsymbol{N}_\alpha, \tag{2.15}$$

where $\boldsymbol{A}$ is the n × n matrix, $\boldsymbol{N}_\alpha$ is the eigenvectors (column vector) and λ_α is the eigenvalues (scalar) that can satisfy this equation. To solve this equation both sides will be multiplied by the identity matrix $\mathbf{1}$ and then regrouped in the following form:

$$[\boldsymbol{A} - \lambda_\alpha \mathbf{1}]\boldsymbol{N}_\alpha = \mathbf{0}. \tag{2.16}$$

In order to have a solution of the equation 2.16 other than $\boldsymbol{N}_\alpha = \mathbf{0}$, $[\boldsymbol{A} - \lambda_\alpha \mathbf{1}]$ should not have an inverse, so its determinant must be equal to zero. Thus, the equality is non-trivially satisfied for $\det[\boldsymbol{A} - \lambda_\alpha \mathbf{1}] = 0$ and this gives the characteristic equation of $\boldsymbol{A}$ which is the n^{th}–order polynomial equation in λ. For $n = 3$ the polynomial equation is expressed as:

$$\lambda_\alpha^3 - I_1\lambda_\alpha^2 + I_2\lambda_\alpha - I_3 = 0, \tag{2.17}$$

which is the general form for 3 × 3 matrices, where the coefficients $I_{i=1,2,3}$ are the principal invariants and are defined as:

$$I_1 = \mathrm{tr}[\boldsymbol{A}], \qquad I_2 = \tfrac{1}{2}\,[I_1^2 - \mathrm{tr}(\boldsymbol{A}^2)], \qquad I_3 = \det[\boldsymbol{A}]. \tag{2.18}$$

The Cayley–Hamilton theorem states that every second–order tensor satisfies its own characteristic equation. Thus, the equation 2.17 can be expressed in the following form

$$\boldsymbol{A}^3 - I_1\boldsymbol{A}^2 + I_2\boldsymbol{A} - I_3 = \boldsymbol{0}. \tag{2.19}$$

Spectral Representation of the Deformation Tensors

Generalized eigenvalue problem of the deformation gradient $\boldsymbol{F}$ is defined by

$$\boldsymbol{F}\boldsymbol{N}_\alpha = \lambda_\alpha \boldsymbol{n}_\alpha \tag{2.20}$$

where, $\boldsymbol{N}_\alpha$, $\boldsymbol{n}_\alpha$ are principle directions in Lagrangian and Eulerian settings, respectively. Here, Lagrangian eigenvector $\boldsymbol{N}_\alpha$ is mapped on to the Eulerian principle stretch vector $\lambda_\alpha \boldsymbol{n}_\alpha$. By inserting 2.2 into 2.20, the following equation is obtained:

$$\boldsymbol{F}\boldsymbol{N}_\alpha = \boldsymbol{R}\boldsymbol{U}\boldsymbol{N}_\alpha = \boldsymbol{R}\lambda_\alpha\boldsymbol{N}_\alpha = \lambda_\alpha\boldsymbol{R}\boldsymbol{N}_\alpha = \lambda_\alpha\boldsymbol{n}_\alpha \tag{2.21}$$

where, $\boldsymbol{U}\boldsymbol{N}_\alpha = \lambda_\alpha\boldsymbol{N}_\alpha$ since $\boldsymbol{U}$ is the Lagrangian stretch tensor and $\boldsymbol{R}\boldsymbol{N}_\alpha = \boldsymbol{n}_\alpha$ since $\boldsymbol{R}$ is the two–point rotation tensor.

Here the right stretch tensor $\boldsymbol{U}$ can be expressed in spectral form by dyadic product of both sides of the term $\boldsymbol{U}\boldsymbol{N}_\alpha = \lambda_\alpha\boldsymbol{N}_\alpha$ with $\boldsymbol{N}_\alpha$;

$$[\boldsymbol{U}\boldsymbol{N}_\alpha = \lambda_\alpha\boldsymbol{N}_\alpha] \otimes \boldsymbol{N}_\alpha \quad \rightarrow \quad \boldsymbol{U} = \sum_{\alpha=1}^{3} \lambda_\alpha \boldsymbol{N}_\alpha \otimes \boldsymbol{N}_\alpha \tag{2.22}$$

and as a result $\boldsymbol{U}$ can be written in terms of principle stretches in principle directions of the Lagrangian eigenvectors, where $\sum_{\alpha=1}^{3} \boldsymbol{N}_\alpha \otimes \boldsymbol{N}_\alpha = \boldsymbol{1}$. Hence, the rotation vector $\boldsymbol{R}$ and the deformation gradient $\boldsymbol{F}$ can be expressed as:

$$[\boldsymbol{R}\boldsymbol{N}_\alpha = \boldsymbol{n}_\alpha] \otimes \boldsymbol{N}_\alpha \quad \rightarrow \quad \boldsymbol{R} = \sum_{\alpha=1}^{3} \boldsymbol{n}_\alpha \otimes \boldsymbol{N}_\alpha, \tag{2.23}$$

$$\boldsymbol{F} = \boldsymbol{R}\boldsymbol{U} = \sum_{\alpha=1}^{3} \lambda_\alpha \boldsymbol{R}\boldsymbol{N}_\alpha \otimes \boldsymbol{N}_\alpha = \sum_{\alpha=1}^{3} \lambda_\alpha \boldsymbol{n}_\alpha \otimes \boldsymbol{N}_\alpha, \tag{2.24}$$

and similarly the left stretch tensor $\boldsymbol{V}$ can be defined as:

$$\boldsymbol{V} = \boldsymbol{F}\boldsymbol{R}^T = (\sum_{\alpha=1}^{3} \lambda_\alpha \boldsymbol{n}_\alpha \otimes \boldsymbol{N}_\alpha)\boldsymbol{R}^T = \sum_{\alpha=1}^{3} \lambda_\alpha \boldsymbol{n}_\alpha \otimes \boldsymbol{R}\boldsymbol{N}_\alpha = \sum_{\alpha=1}^{3} \lambda_\alpha \boldsymbol{n}_\alpha \otimes \boldsymbol{n}_\alpha. \tag{2.25}$$

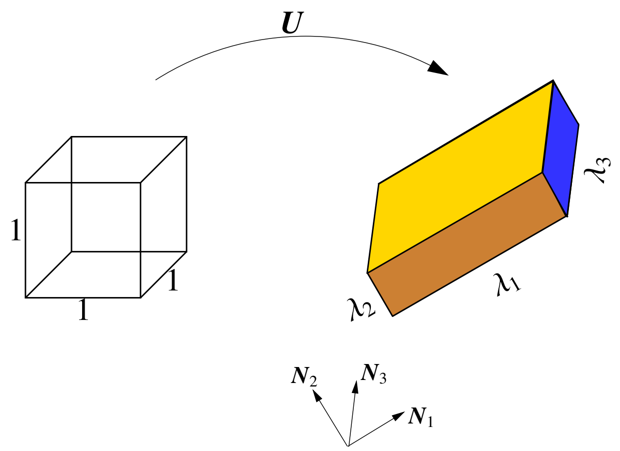

Figure 2.4: Deformation of unit volume element

Moreover the right and left Cauchy–Green tensors can be represented as:

$$\begin{aligned} \boldsymbol{C} &= \boldsymbol{F}^T\boldsymbol{F} = \boldsymbol{U}^T\boldsymbol{R}^T\boldsymbol{R}\boldsymbol{U} = \boldsymbol{U}^T\boldsymbol{1}\boldsymbol{U} \quad \rightarrow \quad \boldsymbol{C} = \boldsymbol{U}^2 = \sum_{\alpha=1}^{3} \lambda_\alpha^2 \boldsymbol{N}_\alpha \otimes \boldsymbol{N}_\alpha \\ \boldsymbol{b} &= \boldsymbol{F}\boldsymbol{F}^T = \boldsymbol{V}\boldsymbol{R}\boldsymbol{R}^T\boldsymbol{V}^T = \boldsymbol{V}\boldsymbol{1}\boldsymbol{V}^T \quad \rightarrow \quad \boldsymbol{b} = \boldsymbol{V}^2 = \sum_{\alpha=1}^{3} \lambda_\alpha^2 \boldsymbol{n}_\alpha \otimes \boldsymbol{n}_\alpha, \end{aligned} \tag{2.26}$$

where $\boldsymbol{U} = \boldsymbol{U}^T$ and $\boldsymbol{V} = \boldsymbol{V}^T$ since both tensors are symmetric, and $\boldsymbol{R}\boldsymbol{R}^T = \boldsymbol{1}$ since $\boldsymbol{R}$ is an orthogonal tensor.

In spectral representation both $\boldsymbol{C}$ and $\boldsymbol{b}$ turn into diagonal matrices which have same principal invariants defined by in terms of the principle stretches:

$$I_1 = \lambda_1{}^2 + \lambda_2{}^2 + \lambda_3{}^2\,, \tag{2.27}$$

$$I_2 = \lambda_1{}^2\lambda_2{}^2 + \lambda_2{}^2\lambda_3{}^2 + \lambda_3{}^2\lambda_1{}^2\,, \tag{2.28}$$

$$I_3 = \lambda_1{}^2\lambda_2{}^2\lambda_3{}^2. \tag{2.29}$$

The energy stored in a hyperelastic isotropic material is characterized by these three invariants of $\boldsymbol{b}$ and $\boldsymbol{C}$, which are also defined as

$$I_1 = \mathrm{tr}\boldsymbol{b}, \qquad I_2 = \frac{1}{2}\left[I_1^2 - \mathrm{tr}(\boldsymbol{b}^2)\right], \qquad I_3 = \det\boldsymbol{b}, \tag{2.30}$$

I_1 : Elongation measure $\qquad$ I_2 : Surface area measure $\qquad$ I_3 : Volume measure,

or in terms of principle stretches shown in Figure 2.4. While I_1 gives the elongation of the element, I_2 can be defined as the area measure, and I_3 gives the change in its volume.

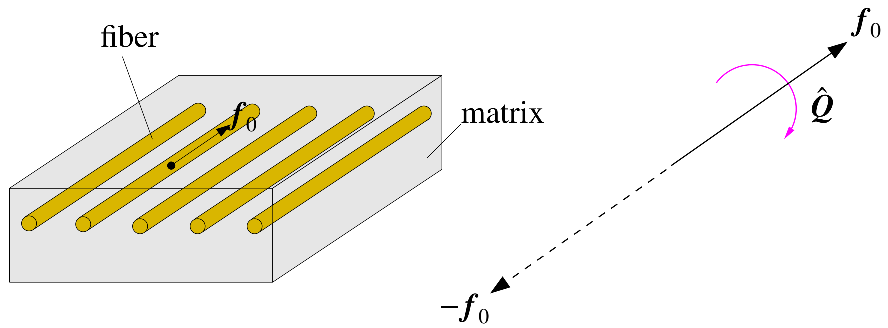

Figure 2.5: Fiber orientation in UD FRP composite with the direction of transverse isotropy $\boldsymbol{f}_0$ and rotation tensor $\hat{\boldsymbol{Q}}$ around $\mp\boldsymbol{f}_0$.

The anisotropic response of a UD FRP composite requires the description of an additional invariant. To this end, a reference unit vector $\boldsymbol{f}_0$ for the fiber orientation in the reference configuration and its spatial counterpart $\boldsymbol{f}$ is introduced as:

$$\boldsymbol{f} = \boldsymbol{F}\boldsymbol{f}_0, \tag{2.31}$$

which idealizes the micro-structure of the UD FRP composite. The related Lagrangian and Eulerian forms of the structure tensors $\boldsymbol{A}$ and $\boldsymbol{A}_f$ can be expressed as follows

$$\boldsymbol{A} = \boldsymbol{f}_0 \otimes \boldsymbol{f}_0 \quad \text{and} \quad \boldsymbol{A}_f = \boldsymbol{f} \otimes \boldsymbol{f}. \tag{2.32}$$

Since it is assumed that the material response is isotropic along the perpendicular directions to the fibers, the structure tensor represents the anisotropy of the material, shows the preferred directions in the material and gives information about its anisotropy. This study focus on UD FRP composites so as shown in Figure 2.5 there is only one group of fibers that causes anisotropy and only one structure tensor. Thus, locally the material is assumed to be transversely isotropic in the direction of $\boldsymbol{f}_0$. This means the material properties are invariant with respect to any rotation $\hat{\boldsymbol{Q}}$ around $\mp\boldsymbol{f}_0$.

In this case, the stretch of the fiber can be determined with the similar approach used in the isotropic material by taking $\boldsymbol{f}_0$ as a unit vector and $\| \boldsymbol{f}_0 \| = 1$. Then, the stretch of the fiber λ_f is defined as:

$$\begin{aligned} \lambda_\mathrm{f}^2 &= \boldsymbol{f} \cdot \boldsymbol{g}\boldsymbol{f} = f^a g_{ab} f^b \\ &= F^a_A {f_0}^A g_{ab} F^b_B {f_0}^B = {f_0}^A F^a_A g_{ab} F^b_B f_{0B} \\ &= {f_0}^A C_{AB} {f_0}^B = \boldsymbol{f}_0 \cdot \boldsymbol{C}\boldsymbol{f}_0, \end{aligned} \tag{2.33}$$

Since $\boldsymbol{C} = \boldsymbol{U}^2$, it is independent from rotation part of the deformation tensor and not affected from a rigid body rotation, the same can be said for the λ_{f}. Finally, the concept of defining the energy stored in a isotropic hyperelastic solid based on invariants can be extended to UD FRP composites by adding a physically meaningful additional fourth–invariant

$$I_4 = \boldsymbol{f} \cdot \boldsymbol{g} \boldsymbol{f} = \lambda_{\mathrm{f}}^2, \tag{2.34}$$

which equals the square of the stretch along the mean fiber direction in the UD FRP composite. In literature for transversely isotropic materials, it is preferred to use an additional fifth–invariant $I_5 = \boldsymbol{f}_0 \cdot \boldsymbol{C}^2 \boldsymbol{f}_0$, but the problems, which discussed in this study, are mainly bending-dominated problems, shear deformations have low energetic contribution. Therefore, it is assumed that the longitudinal and transverse shear responses are nearly identical. So, we keep our model simple and adopt only the fourth–invariant in the subsequent treatment. However, extension of the model to the most general setting is straight forward.

Material and Spatial Velocity Gradients

The tangent map of a material line element $\mathrm{d}\boldsymbol{X}$ on to spacial line element $\mathrm{d}\boldsymbol{x}$ is already defined as $\mathrm{d}\boldsymbol{x} = \boldsymbol{F}\mathrm{d}\boldsymbol{X}$ and derived from this the time derivative of $d\boldsymbol{x}$ is written as:

$$\mathrm{d}\dot{\boldsymbol{x}} = \dot{\boldsymbol{F}}\mathrm{d}\boldsymbol{X} = \boldsymbol{L}\mathrm{d}\boldsymbol{X} \quad \rightarrow \quad \boldsymbol{L} = \dot{\boldsymbol{F}} \tag{2.35}$$

where $\boldsymbol{L}$ is the time derivative of deformation gradient and it maps the material line element $\mathrm{d}\boldsymbol{X}$ on to the time derivative of its spatial counterpart. $\boldsymbol{L}$ is called as the material velocity gradient. Another form of equation 2.35 can be expressed by inserting $\mathrm{d}\boldsymbol{X} = \boldsymbol{F}^{-1}\mathrm{d}\boldsymbol{x}$;

$$\mathrm{d}\dot{\boldsymbol{x}} = \dot{\boldsymbol{F}}\mathrm{d}\boldsymbol{X} = \dot{\boldsymbol{F}}\boldsymbol{F}^{-1}\mathrm{d}\boldsymbol{x} = \boldsymbol{l}\mathrm{d}\boldsymbol{x} \quad \rightarrow \quad \boldsymbol{l} = \dot{\boldsymbol{F}}\boldsymbol{F}^{-1} \tag{2.36}$$

and introducing the spatial velocity gradient $\boldsymbol{l}$. As shown in Figure 2.6, the material and spatial velocity gradients can be described as the maps

$$\begin{aligned} \text{Two point map } (T_X\mathcal{B} \rightarrow T_x\mathcal{S}) : &\qquad \boldsymbol{L}(\boldsymbol{X}, t) \\ \text{Eulerian map } (T_x\mathcal{S} \rightarrow T_x\mathcal{S}) : &\qquad \boldsymbol{l}(\boldsymbol{x}, t). \end{aligned} \tag{2.37}$$

The spatial velocity gradient $\boldsymbol{l}$ can be decomposed into a symmetric and a skew part:

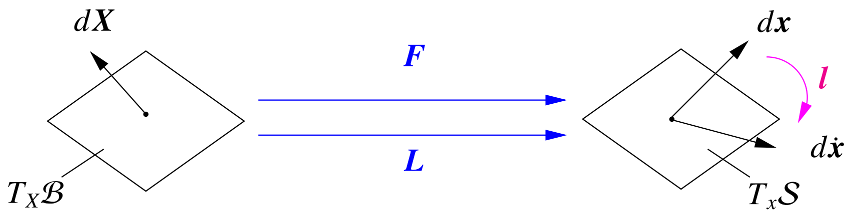

Figure 2.6: Material and spatial velocity gradient mapping.

$$
\begin{aligned}
\boldsymbol{l} &= \boldsymbol{d} + \boldsymbol{w}\,, & (2.38)\\
\boldsymbol{d} &= \mathrm{sym}(\boldsymbol{l}) = \frac{1}{2}[\boldsymbol{l} + \boldsymbol{l}^T]\,, & (2.39)\\
\boldsymbol{w} &= \mathrm{skew}(\boldsymbol{l}) = \frac{1}{2}[\boldsymbol{l} - \boldsymbol{l}^T], & (2.40)
\end{aligned}
$$

where the symmetric part $\boldsymbol{d}$ is called the rate of deformation tensor, the skew part is called the spin tensor. In case that equation 2.36 is rewritten in the decomposed form:

$$
\mathrm{d}\dot{\boldsymbol{x}} = \boldsymbol{l}\mathrm{d}\boldsymbol{x} = (\boldsymbol{d} + \boldsymbol{w})\mathrm{d}\boldsymbol{x} = \boldsymbol{d}\mathrm{d}\boldsymbol{x} + \boldsymbol{w}\mathrm{d}\boldsymbol{x} \tag{2.41}
$$

the first term describes the rate of stretching (stretch velocity) and the last term the rate of rotation (rotational velocity).

$$
\begin{aligned}
\mathrm{d}\dot{\boldsymbol{x}} &= \mathrm{d}\dot{\boldsymbol{x}}_{str} + \mathrm{d}\dot{\boldsymbol{x}}_{rot}\,, & (2.42)\\
\mathrm{d}\dot{\boldsymbol{x}}_{str} &= \boldsymbol{d}\mathrm{d}\boldsymbol{x}\,, & (2.43)\\
\mathrm{d}\dot{\boldsymbol{x}}_{rot} &= \boldsymbol{w}\mathrm{d}\boldsymbol{x}, & (2.44)
\end{aligned}
$$

Lagrangian strain tensor $\boldsymbol{E}$ is defined in equation 2.14. And the time derivative of $\boldsymbol{E}$ is given as:

$$
\dot{\boldsymbol{E}} = \frac{1}{2}\dot{\boldsymbol{C}}, \tag{2.45}
$$

where $\dot{\boldsymbol{C}} = \dot{\boldsymbol{F}}^T\boldsymbol{F} + \boldsymbol{F}^T\dot{\boldsymbol{F}}$. The time derivative of the $\boldsymbol{C}$ can also be written as:

$$
\dot{\boldsymbol{C}} = \dot{\boldsymbol{F}}^T\boldsymbol{F} + \boldsymbol{F}^T\dot{\boldsymbol{F}} = \boldsymbol{F}^T(\dot{\boldsymbol{F}}\boldsymbol{F}^{-1} + \boldsymbol{F}^{-T}\dot{\boldsymbol{F}}^T)\boldsymbol{F} = \boldsymbol{F}^T(2\boldsymbol{d})\boldsymbol{F}. \tag{2.46}
$$

Inserting equation 2.46 into 2.45

$$
\dot{\boldsymbol{E}} = \frac{1}{2}\dot{\boldsymbol{C}} = \boldsymbol{F}^T(\boldsymbol{d})\boldsymbol{F} = \varphi(\boldsymbol{d})^*, \tag{2.47}
$$

implies that $\dot{\boldsymbol{E}}$ is the pull–back of the rate of deformation tensor $\boldsymbol{d}$, see Figure 2.7. And $\boldsymbol{d}$ is the push–forward of $\dot{\boldsymbol{E}} = \frac{1}{2}\dot{\boldsymbol{C}}$.

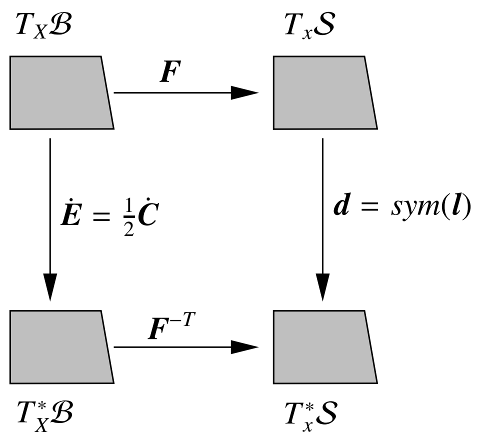

Figure 2.7: Rates of deformation and strain measures.

The Lie Derivatives of Spatial Objects

The Lie derivative of a spatial object $\boldsymbol{f}(\boldsymbol{x}, t)$ describes its relative change with respect to time and provides easy attainment of the time derivatives. It is performed in three steps. First of all, the spatial object is converted into its material counterpart via pull–back operation, then its derivative is taken and finally push–forward operation is performed.

$$\mathscr{L}_v \boldsymbol{f}(\boldsymbol{x}, t) = \boldsymbol{\varphi}_*\{\frac{d}{dt}[\boldsymbol{\varphi}^*(\boldsymbol{f}(\boldsymbol{x}, t))]\} \tag{2.48}$$

2.1.2 Small Strain Kinematics

The continuous body in small strain define as $\mathcal{B} \subset \mathbb{R}^3$ and $\mathcal{T} \subset \mathbb{R}$ is the time interval. The displacement field $\boldsymbol{u} = \boldsymbol{x} - \boldsymbol{X}$ describe the displacement of the material point $\boldsymbol{X} \in \mathcal{B} \subset \mathbb{R}^3$ and at time $t \in \mathcal{T}$ (see Figure 2.8), i.e.

$$\boldsymbol{u}(\boldsymbol{X}, t) : \begin{cases} \mathcal{B} \times \mathcal{T} & \rightarrow \quad \mathbb{R}^3, \\ (\boldsymbol{X}, t) & \mapsto \quad \boldsymbol{u}(\boldsymbol{X}, t). \end{cases} \tag{2.49}$$

Here, $\boldsymbol{u}(\boldsymbol{X}, t)$ can be referred as the displacement map describing the displacement field of a material point. Related velocity and acceleration fields are defined as;

$$\boldsymbol{v}(\boldsymbol{X}, t) = \frac{\partial \boldsymbol{u}(\boldsymbol{X}, t)}{\partial t} = \dot{\boldsymbol{u}}(\boldsymbol{X}, t), \tag{2.50}$$

$$\boldsymbol{a}(\boldsymbol{X}, t) = \frac{\partial \boldsymbol{v}(\boldsymbol{X}, t)}{\partial t} = \ddot{\boldsymbol{u}}(\boldsymbol{X}, t), \tag{2.51}$$

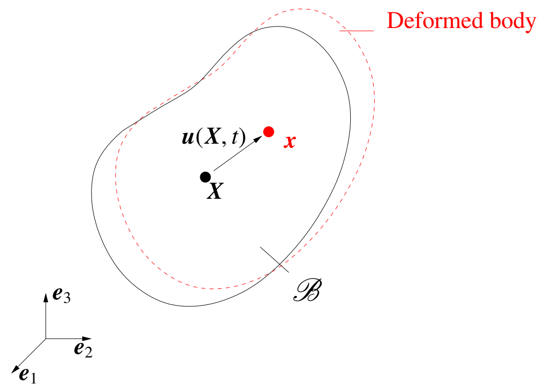

Figure 2.8: Displacement map. The continuum body is denoted as $\mathscr{B}$ and the displacement field is shown as $\boldsymbol{u}(\boldsymbol{X}, t)$.

and the linear strain tensor at material point $\boldsymbol{X} \in \mathcal{B}$ is given by

$$\boldsymbol{\varepsilon} = \text{sym}[\nabla \boldsymbol{u}] = \frac{1}{2}[\nabla \boldsymbol{u} + \nabla \boldsymbol{u}^T], \tag{2.52}$$

where $\nabla \boldsymbol{u} := \dfrac{\partial \boldsymbol{u}_i}{\partial X_j} \boldsymbol{e}_i \otimes \boldsymbol{e}_j$ in an orthonormal system e_i and $i = 1, 2, 3$ with

$$\boldsymbol{e}_i \cdot \boldsymbol{e}_j = \delta_{ij} \quad \text{and} \quad [\boldsymbol{e}_1, \boldsymbol{e}_2, \boldsymbol{e}_3] = 1. \tag{2.53}$$

Vectors and tensors are presented by their Cartesian coordinates as follows:

$$\boldsymbol{u}(\boldsymbol{X}, t) = u_i(\boldsymbol{X}, t)\boldsymbol{e}_i \quad ; \quad \boldsymbol{\varepsilon}(\boldsymbol{X}, t) = \varepsilon_{ij}(\boldsymbol{X}, t)\boldsymbol{e}_i \otimes \boldsymbol{e}_j. \tag{2.54}$$

The trace of the strain tensor

$$e = \text{tr}[\boldsymbol{\varepsilon}] = \varepsilon_{ii} = \varepsilon_{11} + \varepsilon_{22} + \varepsilon_{33} \tag{2.55}$$

describes the volumetric strain (dilatation), while the deviator of $\boldsymbol{\varepsilon}$

$$\text{dev}[\boldsymbol{\varepsilon}] = \boldsymbol{\varepsilon}' = \boldsymbol{\varepsilon} - \frac{1}{3}\,\text{tr}[\boldsymbol{\varepsilon}]\mathbf{1} \tag{2.56}$$

describes the isochoric (volume preserving) part of the deformation. Some examples of volumetric and isochoric deformations are given in Figure 2.9.

2.2 Stress Measures

2.2.1 Stress Measures in Large Strain Setting

The applied loads such as surface tractions or body loads are the reasons for the deformation of a body. And inside the body these forces are described in terms of

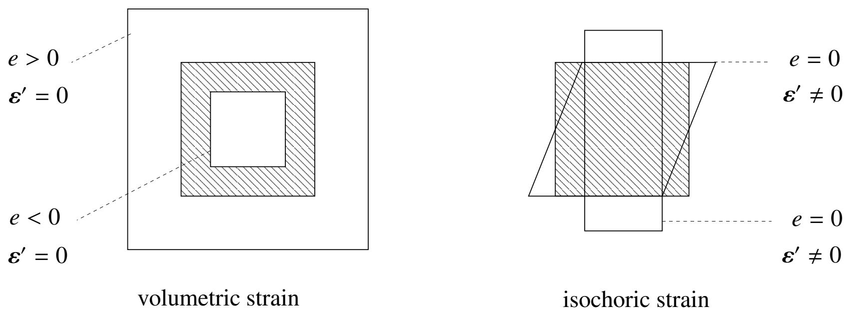

Figure 2.9: Volumetric and isochoric deformations.

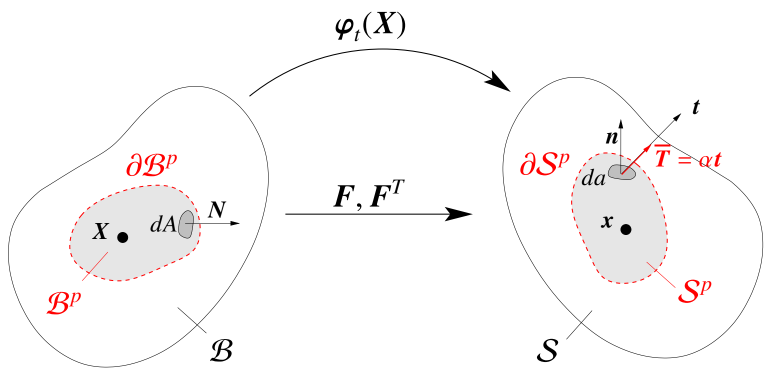

Figure 2.10: Left-hand side is the cut–out $\mathcal{B}^p$ of the body $\mathcal{B}$, right-hand side is its counterpart $\mathcal{S}^p$ in deformed configuration. The surfaces of the cut–out parts are denoted as $\partial\mathcal{B}^p$ and $\partial\mathcal{S}^p$.

stresses. To be able to define these stress descriptions a cut–out part of a Lagrangian body $\mathcal{B}^p$ and its Eulerian counterpart $\mathcal{S}^p$ are introduced here. The cut–out bodies and their related surfaces $\partial\mathcal{B}^p$ and $\partial\mathcal{S}^p$, the undeformed area element dA and its deformed configuration da on the cut–out surfaces and their related unit outward normals $\boldsymbol{N}$ and $\boldsymbol{n}$ are depicted in Figure 2.10. Here the traction vector $\boldsymbol{t}$ represents the surface force acting on da due to its contact with its surrounding environment, and it is defined as force per unit deformed area. According to Cauchy's stress theorem this traction vector in current configuration linearly depends on the outward normal $\boldsymbol{n}$ of the surface da and it is given as:

$$\boldsymbol{t}(\boldsymbol{x}, t, \boldsymbol{n}) = \boldsymbol{\sigma}(\boldsymbol{x}, t)\boldsymbol{n} \quad \Rightarrow \quad t_i = \sigma_{ij} n_j, \tag{2.57}$$

where $\boldsymbol{\sigma}$ denotes the symmetric Eulerian Cauchy (true) stress tensor. As for the Newton's third law of action and reaction $\boldsymbol{t}(\boldsymbol{x}, t, \boldsymbol{n}) = -\boldsymbol{t}(\boldsymbol{x}, t, -\boldsymbol{n})$ for all unit vectors $\boldsymbol{n}$. If the traction vector $\boldsymbol{t}$ thought as a tangent vector, the Cauchy stress tensor $\boldsymbol{\sigma}$ can be defined as a mapping of normal vector on the tangent vector, which both lay in the Eulerian domain.

$$\boldsymbol{\sigma}(\boldsymbol{x}, \mathrm{t}, \boldsymbol{n}) : \begin{cases} T_x^*\mathcal{S} \to T_x\mathcal{S} \\ \boldsymbol{n} \mapsto \boldsymbol{t} = \boldsymbol{\sigma}\boldsymbol{n} \end{cases} \tag{2.58}$$

Different stress measures are obtained from Cauchy stress tensor and the Lagrangian counterpart of the Cauchy stress theorem. The Kirchhoff stress tensor $\boldsymbol{\tau}$, which is also an Eulerian entity, is obtained by

$$\boldsymbol{\tau} = J\boldsymbol{\sigma} \tag{2.59}$$

where $J = \det \boldsymbol{F}$. To define the alternative representation of the Eulerian Cauchy theorem the nominal traction vector $\overline{\boldsymbol{T}}$, which is associated with the underformed area, is presented as a scalar multiple of $\boldsymbol{t}$

$$\overline{\boldsymbol{T}} = \alpha \boldsymbol{t} \tag{2.60}$$

where $\alpha = \dfrac{\mathrm{da}}{\mathrm{dA}}$. Thus, as shown in Figure 2.10 $\overline{\boldsymbol{T}}$ and $\boldsymbol{t}$ are parallel to each other and their relation can also be expressed as:

$$\boldsymbol{t}\mathrm{da} = \overline{\boldsymbol{T}}\mathrm{dA}. \tag{2.61}$$

Then the alternative representation of the Cauchy theorem reads

$$\overline{\boldsymbol{T}} = \boldsymbol{P}\boldsymbol{N}, \tag{2.62}$$

where $\boldsymbol{P}$ denotes the first Piola–Kirchhoff stress tensor. Since $\overline{\boldsymbol{T}}$ in Eulerian domain and $\boldsymbol{N}$ is in the Lagrangian domain $\boldsymbol{P}$ is a two point tensor. Its relation with the Cauchy stress is obtained from equation 2.61 and 2.62 besides recalling area map equation 2.5 as follows

$$\boldsymbol{P}\boldsymbol{N}\mathrm{dA} = \boldsymbol{\sigma}\boldsymbol{n}\mathrm{da} \quad \text{with} \quad \boldsymbol{n}\mathrm{da} = J\boldsymbol{F}^{-T}\boldsymbol{N}\mathrm{dA} \tag{2.63}$$

$$\boldsymbol{P}\boldsymbol{N}\mathrm{dA} = \boldsymbol{\sigma}J\boldsymbol{F}^{-T}\boldsymbol{N}\mathrm{dA} \quad \Rightarrow \quad \boldsymbol{P} = J\boldsymbol{\sigma}\boldsymbol{F}^{-T} = \boldsymbol{\tau}\boldsymbol{F}^{-T}. \tag{2.64}$$

Although $\boldsymbol{\sigma}$ and $\boldsymbol{\tau}$ are symmetric tensors ($\boldsymbol{\sigma}^T = \boldsymbol{\sigma}$ and $\boldsymbol{\tau}^T = \boldsymbol{\tau}$), the first Piola–Kirchhoff stress $\boldsymbol{P}$ is not a symmetric tensor. Since $\boldsymbol{P}\boldsymbol{F}^T = \boldsymbol{\tau}$ it can be written as:

$$\boldsymbol{P}\boldsymbol{F}^T = \boldsymbol{F}\boldsymbol{P}^T. \tag{2.65}$$

Finally purely Lagrangian stress description is defined by transforming nominal

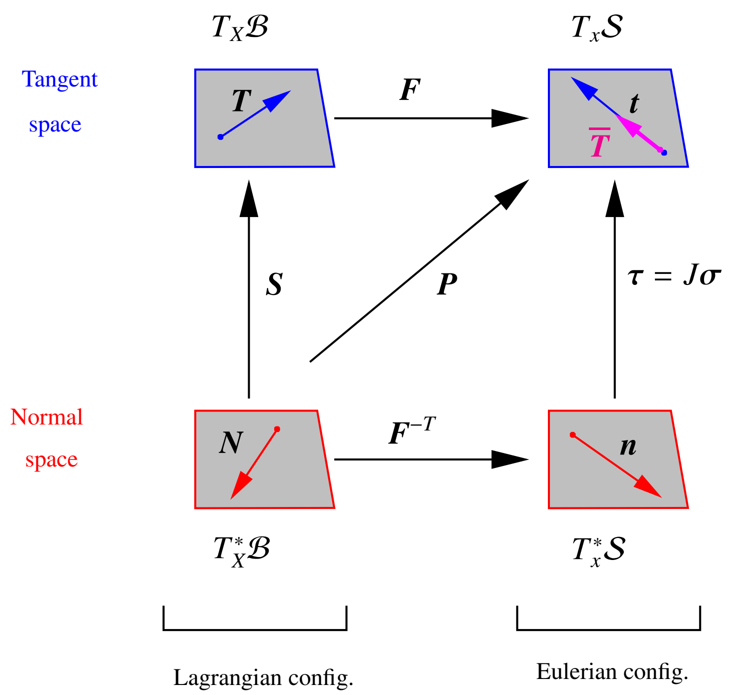

Figure 2.11: Definition of stress tensors and traction vectors in large strain.

traction vector $\overline{\boldsymbol{T}}$ from Eularian to Lagrangian domain,

$$\boldsymbol{T} = \boldsymbol{F}^{-1}\overline{\boldsymbol{T}}, \tag{2.66}$$

then postulating purely Lagrangian counterpart of the Eulerian Cauchy theorem as follows

$$\boldsymbol{T} = \boldsymbol{S}\boldsymbol{N}, \tag{2.67}$$

where $\boldsymbol{S}$ is the second Piola–Kirchhoff stress. From equations 2.62, 2.66 and 2.62 the relationship between $\boldsymbol{P}$ and $\boldsymbol{S}$ reads

$$\boldsymbol{F}^{-1}\boldsymbol{P} = \boldsymbol{S}, \tag{2.68}$$

and with $\boldsymbol{P} = \boldsymbol{\tau}\boldsymbol{F}^{-T}$ the second Piola–Kirchhoff stress can be defined as the pull–back of Kirchhoff stress

$$\boldsymbol{S} = \boldsymbol{\varphi}^*(\boldsymbol{\tau}) = \boldsymbol{F}^{-1}\boldsymbol{\tau}\boldsymbol{F}^{-T}. \tag{2.69}$$

Note that, since $\boldsymbol{\tau}$ is a symmetric tensor $\boldsymbol{S}$ is also symmetric and it acts as a map from Lagrangian normal domain to Lagrangian tangent domain. All these relations between the stresses and maps are summarized in Figure 2.11.

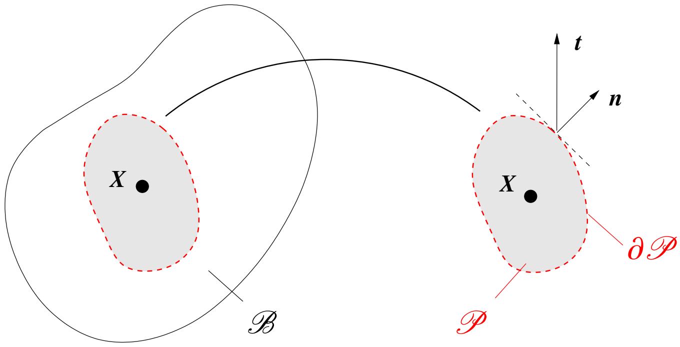

Figure 2.12: Left-hand side is the body $\mathscr{B}$, right-hand side is the cut–out part $\mathscr{P} \subset \mathscr{B}$ of the body. The surface of the cut–out part is denoted as $\partial\mathscr{P}$.

2.2.2 Stress Measure in Small Strain Setting

Eulers cut principle is also applied here and a finite volume of $\mathcal{P} \subset \mathcal{B}$ is cut-out from the body $\mathcal{B}$ depicted in Figure 2.12. The action of the rest of the body on $\mathcal{P}$ is replaced by the traction field $\boldsymbol{t}(\boldsymbol{X}, t, \boldsymbol{n})$ on the cut–surface $\partial\mathcal{P}$ with the surface normal $\boldsymbol{n}$. And the stress tensor is defined as

$$\boldsymbol{t}(\boldsymbol{X}, t, \boldsymbol{n}) = \boldsymbol{\sigma}(\boldsymbol{X}, t)\boldsymbol{n} \tag{2.70}$$

by the Cauchy theory. The stress tensor is visualized in Figure 2.13 by taking an infinitesimal volume element $\mathrm{d}V \in \mathcal{B}$ with the surface normals which are all aligned in the Cartesian coordinates $\{\boldsymbol{e}_i\}_{i=1,2,3}$. Traction vectors acting on the surfaces of $\mathrm{d}V$ with the surface normals $\boldsymbol{e}_i$ define as

$$\begin{aligned} \boldsymbol{t}_1 &= \sigma_{11}\,\boldsymbol{e}_1 + \sigma_{12}\,\boldsymbol{e}_2 + \sigma_{13}\,\boldsymbol{e}_3 \\ \boldsymbol{t}_2 &= \sigma_{21}\,\boldsymbol{e}_1 + \sigma_{22}\,\boldsymbol{e}_2 + \sigma_{23}\,\boldsymbol{e}_3 \\ \boldsymbol{t}_3 &= \sigma_{31}\,\boldsymbol{e}_1 + \sigma_{32}\,\boldsymbol{e}_2 + \sigma_{33}\,\boldsymbol{e}_3. \end{aligned} \tag{2.71}$$

With indicial notation the equation 2.71 can be expressed as:

$$\boldsymbol{t}_i = \sigma_{ij}\,\boldsymbol{e}_j \tag{2.72}$$

where there is a summation over j, and the stress tensor can be define as:

$$\sigma_{ij} = \boldsymbol{t}_i\,\boldsymbol{e}_j. \tag{2.73}$$

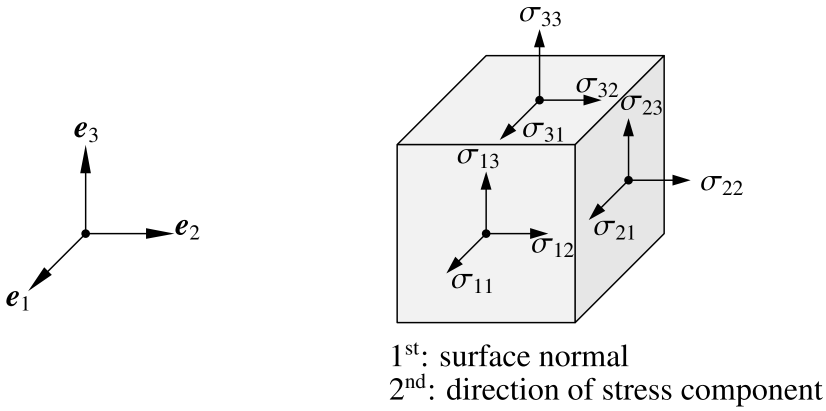

Figure 2.13: Stress components on the surfaces of the cube. The first indice of the stress component indicates the surface normal, second indice defines the direction of the stress component.

2.3 Balance Laws of Continuum Thermomechanics

As mentioned before a cut–out part of a continuum can be loaded by volume and surface loads. The thermomechanical surface loads define as traction $\boldsymbol{t}$ and the heat flux vector $\boldsymbol{q}$ with heat flux $h = \boldsymbol{q} \cdot \boldsymbol{n}$, and the volume loads define as body forces $\boldsymbol{b}$ and the heat source r (per unit mass) which may caused by a chemical reaction. The cut–out part has also the following basic physical quantities which are define as mass m, linear momentum $\mathcal{I}$, angular momentum $\mathcal{D}_0$, kinetic energy K, internal energy E (per unit mass), entropy H (per unit mass), and entropy production Γ (per unit mass). These physical quantities are given in the Table 2.1 where $\rho(\boldsymbol{X}, t)$ is the density, $\boldsymbol{v}(\boldsymbol{X}, t)$ is the velocity, $e(\boldsymbol{X}, t)$ is the internal-energy along with $\eta(\boldsymbol{X}, t)$ and $\gamma(\boldsymbol{X}, t)$ are defined as the entropy and entropy-production respectively.

The fundamental balance laws of continuum mechanics set the relationship between these physical fields and the global quantities like mechanical force, moment and power associated with the loads on the cut–out body. With the Tables 2.1 and 2.2 at hand, the global forms of the balance equations of continuum mechanics are intro-

Table 2.1: Physical quantities of the cut–out $\mathcal{P} \subset \mathcal{B}$.

Mass	$m := \int_{\mathcal{P}} \rho \mathrm{d}V$
Linear momentum	$\mathcal{I} := \int_{\mathcal{P}} \rho \boldsymbol{v} \mathrm{d}V$
Angular momentum	$\mathcal{D}_0 := \int_{\mathcal{P}} \boldsymbol{X} \times \rho \boldsymbol{v} \mathrm{d}V$
Kinetic energy	$K := \frac{1}{2} \int_{\mathcal{P}} \rho \boldsymbol{v} \cdot \boldsymbol{v} \mathrm{d}V$
Internal energy	$E := \int_{\mathcal{P}} \rho e \mathrm{d}V$
Entropy	$H := \int_{\mathcal{P}} \rho \eta \mathrm{d}V$
Entropy production	$\Gamma := \int_{\mathcal{P}} \rho \gamma \mathrm{d}V$

Table 2.2: Loading quantities of the cut–out $\mathcal{P} \subset \mathcal{B}$.

Mechanical force	$\boldsymbol{F} := \int_{\mathcal{P}} \rho \boldsymbol{b} \mathrm{d}V + \int_{\partial\mathcal{P}} \boldsymbol{t} \mathrm{d}A$
Mechanical couple	$\boldsymbol{M}_0 := \int_{\mathcal{P}} \boldsymbol{X} \times \rho \boldsymbol{b} \mathrm{d}V + \int_{\partial\mathcal{P}} \boldsymbol{X} \times \boldsymbol{t} \mathrm{d}A$
Mechanical power	$P := \int_{\mathcal{P}} \rho \boldsymbol{b} \cdot \boldsymbol{v} \mathrm{d}V + \int_{\partial\mathcal{P}} \boldsymbol{t} \cdot \boldsymbol{v} \mathrm{d}A$
Thermal power	$Q := \int_{\mathcal{P}} \rho r \mathrm{d}V - \int_{\partial\mathcal{P}} h \mathrm{d}A$
Entropy power	$S := \int_{\mathcal{P}} \rho \frac{r}{\theta} \mathrm{d}V - \int_{\partial\mathcal{P}} \frac{h}{\theta} \mathrm{d}A$

duced as:

$$
\begin{array}{lll}
\text{(i) Conservation of mass} & \dfrac{\mathrm{d}}{\mathrm{d}t}m = 0 & \\
\text{(ii) Conservation of linear momentum} & \dfrac{\mathrm{d}}{\mathrm{d}t}\boldsymbol{\mathcal{I}} = \boldsymbol{F} & \\
\text{(iii) Conservation of angular momentum} & \dfrac{\mathrm{d}}{\mathrm{d}t}\boldsymbol{\mathcal{D}}_0 = \boldsymbol{M}_0 & \\
\text{(iv) Conservation of energy (}1^{st}\text{ law)} & \dfrac{\mathrm{d}}{\mathrm{d}t}[K + E] = P + Q & \\
\text{(v) Conservation of entropy (}2^{nd}\text{ law)} & \dfrac{\mathrm{d}H}{\mathrm{d}t} - S \geq 0 &
\end{array}
\tag{2.74}
$$

The local forms of the balance equations are obtained by inserting Cauchy theorems $\boldsymbol{t} = \boldsymbol{\sigma} \cdot \boldsymbol{n}$ and $h = \boldsymbol{q} \cdot \boldsymbol{n}$, then transforming surface integrals in volume integrals by Gauss–theorem, and finally applying the localization theorem, which states that, if the volume integral is equal to zero, the term inside the integral should also be equal to zero. Thus, the local forms of the balance equations for the small strain assumption read:

$$
\begin{array}{ll}
\text{(i) mass} & \dot{\rho} = 0 \\
\text{(ii) linear momentum} & \rho\dot{\boldsymbol{v}} = \operatorname{div}\boldsymbol{\sigma} + \rho\boldsymbol{b} \\
\text{(iii) angular momentum} & \boldsymbol{\sigma}^T = \boldsymbol{\sigma} \\
\text{(iv) energy (}1^{st}\text{ law)} & \dot{e} = \boldsymbol{\sigma} : \dot{\boldsymbol{\varepsilon}} - \operatorname{div}\boldsymbol{q} + r \\
\text{(v) entropy (}2^{nd}\text{ law)} & \rho\gamma := \rho\dot{\eta} - \dfrac{1}{\theta}(r - \operatorname{div}\boldsymbol{q}) - \dfrac{1}{\theta^2}\boldsymbol{q} \cdot \nabla\theta \geq 0
\end{array}
\tag{2.75}
$$

For the large strain approach there are both spatial(Eulerian) and material (Lagrangian) forms of the balance laws. The local forms of the balance equations in spatial and material configurations is summarized as:

$$
\begin{aligned}
&\text{(i) mass balance}\\
&\quad \textit{material}: \quad \dot{\rho}_0 = 0 \quad \text{and} \quad J\rho = \rho_0(\boldsymbol{X})\\
&\quad \textit{spatial}: \quad \dot{\rho} + \rho\,\mathrm{div}[\boldsymbol{v}] = 0\\
&\text{(ii) linear momentum balance}\\
&\quad \textit{material}: \quad \rho_0\dot{\boldsymbol{V}} = \mathrm{DIV}\boldsymbol{P} + \rho_0\boldsymbol{B}\\
&\quad \textit{spatial}: \quad \rho\dot{\boldsymbol{v}} = \mathrm{div}\,\boldsymbol{\sigma} + \rho\boldsymbol{b}\\
&\text{(iii) angular momentum balance}\\
&\quad \textit{material}: \quad \boldsymbol{S}^T = \boldsymbol{S} \quad \text{and} \quad \boldsymbol{F}^{-1}\boldsymbol{P} = \boldsymbol{P}^T\boldsymbol{F}^{-T}\\
&\quad \textit{spatial}: \quad \boldsymbol{\sigma}^T = \boldsymbol{\sigma} \quad \text{and} \quad \boldsymbol{\tau}^T = \boldsymbol{\tau} \quad \text{and} \quad \boldsymbol{P}\boldsymbol{F}^T = \boldsymbol{F}\boldsymbol{P}^T\\
&\text{(iv) energy balance } (1^{st} \text{ law})\\
&\quad \textit{material}: \quad \rho_0\dot{e} = \boldsymbol{P} : \dot{\boldsymbol{F}} - \mathrm{DIV}\boldsymbol{Q} + \rho_0 R\\
&\quad \textit{spatial}: \quad \rho\dot{e} = \boldsymbol{\sigma} : \boldsymbol{d} - \mathrm{div}\,\boldsymbol{q} + \rho r\\
&\text{(v) entropy inequality } (2^{nd} \text{ law})\\
&\quad \textit{material}: \quad \rho_0\gamma := \rho_0\dot{\eta} - \frac{1}{\theta}(\rho_0 R - \mathrm{DIV}\boldsymbol{Q}) - \frac{1}{\theta^2}\boldsymbol{Q}\cdot\nabla_X\theta \geq 0\\
&\quad \textit{spatial}: \quad \rho\gamma := \rho\dot{\eta} - \frac{1}{\theta}(\rho r - \mathrm{div}\,\boldsymbol{q}) - \frac{1}{\theta^2}\boldsymbol{q}\cdot\nabla_{\boldsymbol{x}}\theta \geq 0
\end{aligned}
\tag{2.76}
$$

where material density $\rho_0(\boldsymbol{X}) = J\rho(\boldsymbol{x}, t)$, material velocity $\boldsymbol{V} = \dfrac{\mathrm{d}}{\mathrm{d}t}\varphi(\boldsymbol{X}, t) = \boldsymbol{v}(\boldsymbol{x}, t) \circ \boldsymbol{\varphi}_t(\boldsymbol{X})$, material heat generation $R(\boldsymbol{X}, t) = r(\boldsymbol{x}, t) \circ \boldsymbol{\varphi}_t(\boldsymbol{X})$, material body loads $\boldsymbol{B}(\boldsymbol{X}, t) = \boldsymbol{b}(\boldsymbol{x}, t) \circ \boldsymbol{\varphi}_t(\boldsymbol{X})$ and material heat flux vector $\boldsymbol{Q} = J\boldsymbol{q}\boldsymbol{F}^{-T}$.

2.4 Principle of Irreversibility

Constitutive equations of the materials are formulated such that the 2^{nd} law of thermodynamics is always satisfied, so that the constitutive equations are said to be thermodynamically consistent. In other words the conservation of entropy equations given in 2.75 and 2.85, which are also called as "Clausius–Duhem Inequality", serves as a restriction on the constitutive equations. To this end, the dissipation

$$\mathcal{D} = \theta\gamma \geq 0 \tag{2.77}$$

is introduced.

In small strain setting, by multiplying the conservation of entropy equation with θ and blending the energy balance law in to the equation, the dissipation equation turns into

$$\rho\mathcal{D} = \rho\theta\gamma = \boldsymbol{\sigma} : \dot{\boldsymbol{\varepsilon}} - \rho\dot{e} + \rho\theta\dot{\eta} - \frac{1}{\theta}\boldsymbol{q} \cdot \nabla\theta \geq 0, \tag{2.78}$$

which is called as the "Modified Clausius–Duhem Inequality". In equation 2.78 the first three terms have time derivatives, thus this terms can be defined as local terms. Forth term in 2.78 has a gradient operator which makes the term non-local. Consequently, the Clausius–Duhem Inequality can decomposed into local and non-local (conductive) parts

$$\rho\mathcal{D} = \rho\mathcal{D}_{loc} + \rho\mathcal{D}_{con}, \tag{2.79}$$

which can be define as:

$$\rho\mathcal{D}_{loc} = \boldsymbol{\sigma} : \dot{\boldsymbol{\varepsilon}} - \rho\dot{e} + \rho\theta\dot{\eta} \geq 0 \quad : \quad \text{Clausius–Planck inequality ,} \tag{2.80}$$

$$\rho\mathcal{D}_{con} = -\frac{1}{\theta}\boldsymbol{q} \cdot \nabla\theta \geq 0 \quad : \quad \text{Fourier inequality,} \tag{2.81}$$

and they have to satisfy the inequality separately. In solid mechanics, Helmholtz free energy Ψ, which is equal to

$$\Psi = e - \theta\eta, \tag{2.82}$$

is mostly utilized instead of internal energy e, and the time derivative of Ψ reads

$$\dot{\Psi} = \dot{e} - \theta\dot{\eta} - \dot{\theta}\eta. \tag{2.83}$$

The equation 2.83 can be rearranged as $\dot{\Psi} + \dot{\theta}\eta = \dot{e} - \theta\dot{\eta}$ and inserted into equation 2.81. This gives the alternative form of Clausius–Planck Inequality (CPI)

$$\rho\mathcal{D}_{loc} = \boldsymbol{\sigma} : \dot{\boldsymbol{\varepsilon}} - \rho\dot{\Psi} - \rho\dot{\theta}\eta \geq 0 \quad : \quad \text{Alternative form of CPI} \tag{2.84}$$

For the large strain approach the inequalities 2.81 and 2.84 can also be expressed in their material(Lagrangian) and spatial(Eulerian) forms

$$
\begin{aligned}
&\text{Claudius–Planck inequality} && \\
&\quad \textit{material}: && \rho_0 \mathcal{D}_{loc} = \boldsymbol{P} : \dot{\boldsymbol{F}} - \rho_0 \dot{\Psi} - \rho_0 \eta \dot{\theta} \geq 0 \\
&\quad \textit{spatial}: && \rho \mathcal{D}_{loc} = \boldsymbol{\sigma} : \dot{\boldsymbol{d}} - \rho \dot{\Psi} - \rho \eta \dot{\theta} \geq 0 \\
&\text{Fourier inequality} && \\
&\quad \textit{material}: && -\frac{1}{\theta} \boldsymbol{Q} \cdot \nabla_{\boldsymbol{X}} \theta \geq 0 \\
&\quad \textit{spatial}: && -\frac{1}{\theta} \boldsymbol{q} \cdot \nabla_{\boldsymbol{x}} \theta \geq 0
\end{aligned}
\tag{2.85}
$$

<u>Coleman's Exploitation Method</u>

If the problem is restricted to be thermoelastic, the only dissipation will be due to heat conduction and the local dissipation will be zero ($\mathcal{D}_{loc} = 0$). Then the local time derivative of the Helmholtz free energy $\Psi = \hat{\Psi}(\boldsymbol{\varepsilon}, \theta, \nabla\theta)$,

$$\dot{\Psi} = \partial_{\boldsymbol{\varepsilon}} \hat{\Psi} : \dot{\boldsymbol{\varepsilon}} + \partial_\theta \hat{\Psi} \dot{\theta} + \partial_{\nabla\theta} \hat{\Psi} \cdot \dot{\nabla}\theta, \tag{2.86}$$

is inserted in the equation 2.84 and the local dissipation equation becomes

$$\rho \mathcal{D}_{loc} = [\boldsymbol{\sigma} - \rho \partial_{\boldsymbol{\varepsilon}} \hat{\Psi}] : \dot{\boldsymbol{\varepsilon}} - \rho[\eta + \partial_\theta \hat{\Psi}] \dot{\theta} - \rho \partial_{\nabla\theta} \hat{\Psi} \cdot \dot{\nabla}\theta = 0. \tag{2.87}$$

Following the Coleman's assumption, bracket should vanish for arbitrary rates $\dot{\boldsymbol{\varepsilon}}$, $\dot{\theta}$, $\dot{\nabla}\theta$. one obtains the constitutive equations

$$\boldsymbol{\sigma} = \rho \partial_{\boldsymbol{\varepsilon}} \hat{\Psi}(\boldsymbol{\varepsilon}, \theta) \quad \text{and} \quad \eta = -\partial_\theta \hat{\Psi}(\boldsymbol{\varepsilon}, \theta) \tag{2.88}$$

with $\partial_{\nabla\theta} \hat{\Psi} = 0$, which shows that the free energy is not a function of temperature gradient $\nabla\theta$.

CHAPTER 3

FUNDAMENTALS OF THE MULTI-FIELD PROBLEM OF FRACTURE

This chapter lays bare the primary field variables, namely the crack phase–field d and the deformation map $\boldsymbol{\varphi}$ governing the diffusive crack evolution and the balance of linear momentum in a coupled manner. The framework is provided for the finite and small–strain settings which cover both the mechanical and phase–field problems. The details of the framework is also provided by [16], [17] which are the published works throughout the thesis study.

3.1 The Primary Field Variables

Lets consider a continuum body at time $t_0 \in \mathcal{T} \subset \mathbb{R}$, which is referred as the reference configuration, as designated by $\mathcal{B} \subset \mathbb{R}^3$, with the material point $\boldsymbol{X} \in \mathcal{B}$. Similarly, the deformed body at current time $t \in \mathcal{T} \subset \mathbb{R}$, which is referred as the spatial configuration, is denoted by $\mathcal{S} \subset \mathbb{R}^3$ with the spatial point $\boldsymbol{x} \in \mathcal{S}$ mapped via the deformation field $\boldsymbol{\varphi}$ as shown in Figure 3.1. In Figure 3.1 the deformation gradient $\boldsymbol{F}$ maps a Lagrangian line element $\mathrm{d}\boldsymbol{X}$ onto its Eulerian counterpart $\mathrm{d}\boldsymbol{x} = \boldsymbol{F}\mathrm{d}\boldsymbol{X}$. The anisotropic micro-structure of the material point $\boldsymbol{X}$ is rendered by UD fibers with the unit vector $\boldsymbol{f}_0$. Likewise, the anisotropic micro-structure of the spatial point $\boldsymbol{x}$ is described by $\boldsymbol{f}$, as the spatial counterpart of $\boldsymbol{f}_0$. Thus,

$$\boldsymbol{\varphi}_t(\boldsymbol{X}) : \begin{cases} \mathcal{B} \times \mathcal{T} & \rightarrow \quad \mathcal{S}, \\ (\boldsymbol{X}, t) & \mapsto \quad \boldsymbol{x} = \boldsymbol{\varphi}(\boldsymbol{X}, t). \end{cases} \tag{3.1}$$

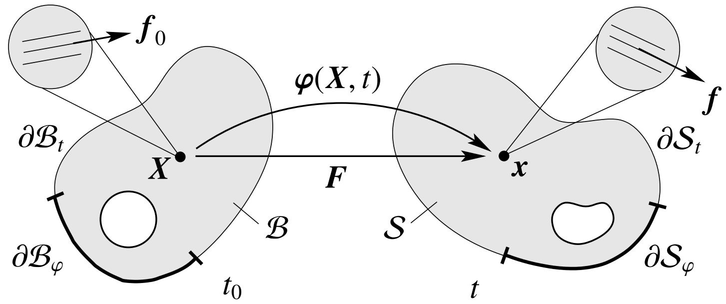

Figure 3.1: Nonlinear deformation of a solid. The reference configuration $\mathcal{B} \in \mathbb{R}^3$ and the spatial configuration $\mathcal{S} \in \mathbb{R}^3$; $\boldsymbol{\varphi} : \mathcal{B} \times \mathbb{R} \mapsto \mathbb{R}^3$ is the nonlinear deformation map which maps the material point position $\boldsymbol{X} \in \mathcal{B}$ onto the spatial position $\boldsymbol{x} = \boldsymbol{\varphi}(\boldsymbol{X}, t) \in \mathcal{S}$, at time $t \in \mathbb{R}_t$.

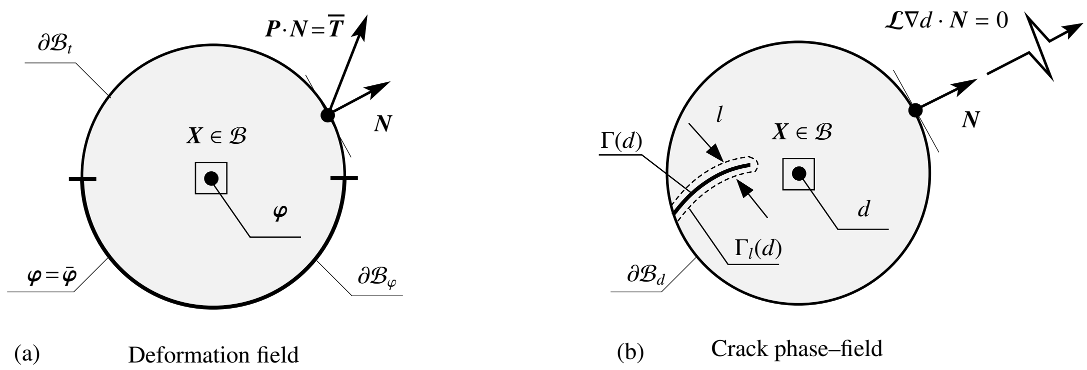

Figure 3.2: Multi-field problem: (a) mechanical problem of deformation along with Dirichlet and Neumann-type boundary conditions, that is $\boldsymbol{\varphi} = \overline{\boldsymbol{\varphi}}$ and $\boldsymbol{P} \cdot \boldsymbol{N} = \overline{\boldsymbol{T}}$, respectively; (b) evolution of the crack phase–field problem with the Neumann-type boundary condition $\mathcal{L}\nabla d \cdot \boldsymbol{N} = 0$.

Along with the deformation field given in equation 3.1, the basic geometric mapping for the crack phase–field d is expressed by

$$d : \begin{cases} \mathcal{B} \times \mathcal{T} & \rightarrow \quad [0, 1], \\ (\boldsymbol{X}, t) & \mapsto \quad d(\boldsymbol{X}, t), \end{cases} \tag{3.2}$$

which interpolates between the intact ($d = 0$) and the ruptured ($d = 1$) state of the material. The mapping of the crack phase–field happens in the Lagrangian domain, since the strain at failure not high for FRP composites, it gives sufficiently good results.

3.2 Geometric Representation of the Ginzburg Landau Phase–Field Approach

Before discussing the 3D phase–field approach for the brittle fracture of anisotropic solids, the formulation for cracks in one–dimensional (1D) solids and its extension to 3D isotropic solids is discussed briefly with reference to the works [34], [35], [36], [36].

3.2.1 Ginzburg–Landau Type Phase–Field Approach for Brittle Fracture of Isotropic Solids

A sharp crack surface topology at a frozen time t is defined by $\Gamma(d) \subset \mathbb{R}^2$ in the solid $\mathcal{B}$ through a surface integral $\Gamma(d) = \int_\Gamma \mathrm{d}A$. The hallmark of the crack phase–field approach is that it circumvents the cumbersome task of tracking such discontinuities and it approximates the surface integral by a volume integral, thereby creating a regularized crack surface $\Gamma_l(d)$ shown in Figure 3.2(b), whose definition is given in coming sections.

Phase–field approach in 1D setting

Infinitely long 1D bar ($L = [-\infty, +\infty]$) with a cross section of Γ is assumed to have a crack at its origin $x = 0$. Since the cross section of the bar is Γ, it represents the fully cracked surface. The whole domain is defined as $\mathcal{B} = \Gamma \times L$. The sharp crack topology is described by an assisting crack phase–field variable $d(x)$ equal to Kronecker delta function $\delta(x)$

$$d(x) := \delta(x) : \begin{cases} 1 & \text{for} \quad x = 0, \\ 0 & \text{otherwise,} \end{cases} \tag{3.3}$$

where $d = 0$ and $d = 1$ mark the unbroken (intact) and the broken (cracked) state of the solid without any intermediate state. On the other hand, regularized or diffusive crack topology

$$d(x) = e^{-|x|/l}, \tag{3.4}$$

smears out the crack over the axial domain L, creating the intermediate states between fully cracked and intact states as shown in the Figure 3.3. The l parameter in 3.4 is defined as the length–scale parameter, and it controls the breadth of the crack. When

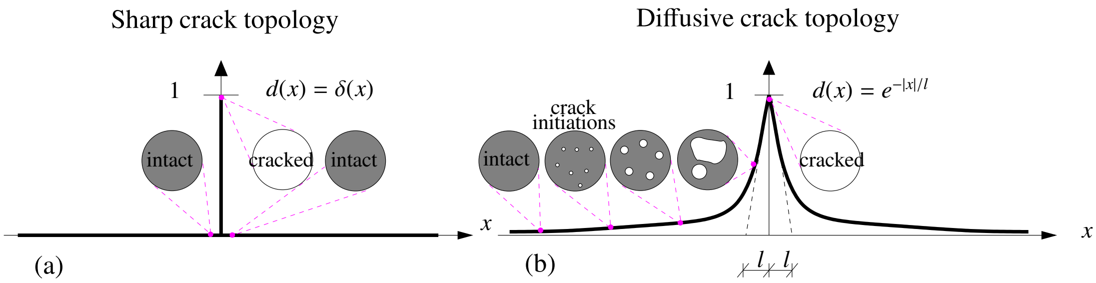

Figure 3.3: Sharp and regularized crack topology. (a) Sharp crack at $x = 0$ modelled by Kronecker delta function $d(x) = \delta(x)$, (b) regularized crack topology at $x = 0$ described by $d(x) = e^{-|x|/l}$ with a length scale parameter l which controls the breadth of crack .

l becomes smaller and smaller and vanishes ($l \to 0$) the equation 3.4 becomes same as the equation 3.3.

Noting that the equation 3.4 is the solution of the homogeneous differential equation

$$d(x) - l^2 d''(x) = 0 \tag{3.5}$$

with the essential boundary conditions of

$$d(0) = 1, \qquad d(\pm\infty) = 0, \tag{3.6}$$

the equation 3.5 can be regarded as the Euler-Lagrange equation of the variational principle

$$d = \text{Arg}\left\{ \inf_{d \in \mathcal{W}_d} I(d) \right\}. \tag{3.7}$$

The potential function $I(d)$ is given as

$$I(d) = \frac{1}{2} \int_{\mathcal{B}} (d^2 + l^2 d'^2) \mathrm{d}V, \tag{3.8}$$

which can be constructed by integrating a Galerkin– type weak form of the differential equation 3.5. If the solution 3.4 put into equation 3.8, the potential gives

$$I(d = e^{-|x|/l}) = l\Gamma \tag{3.9}$$

with $\mathrm{d}V = \Gamma \mathrm{d}x$, which provides a relation between $I(d)$ and the crack surface Γ. As a result, a new functional is introduced

$$\Gamma_l(d) := \frac{1}{l} I(d) = \frac{1}{2l} \int_{\mathcal{B}} (d^2 + l^2 d'^2) \mathrm{d}V \tag{3.10}$$

and define as the regularized crack functional.

Phase–field approach in 3D setting

The 3D formulation of the regularized crack functional in solids can be derived similar to 1D setting, so the regularized crack surface function in 3D setting is defined as:

$$\begin{aligned} \Gamma_l(d) &= \int_{\mathcal{B}} \gamma(d, \nabla d) \mathrm{d}V \quad \text{where} \\ \gamma(d, \nabla d) &= \frac{1}{2l}(d^2 + l^2 \nabla d \cdot \nabla d)\,, \end{aligned} \tag{3.11}$$

designates the *isotropic crack surface density* function. The deformable domain for the concerning problem is associated with the deformation field as given in Figure 3.2(a). For a non-deformable domain, the gradient operator can simply be taken as $\nabla_x(\bullet) = \nabla_X(\bullet) = \nabla(\bullet)$.

3.2.2 Ginzburg–Landau Type Phase–Field Approach for Brittle Fracture of Anisotropic Solids

The approximation given in equation 3.11 can be extended to a class of anisotropic materials

$$\begin{aligned} \Gamma_l(d) &= \int_{\mathcal{B}} \gamma(d, \nabla d; \boldsymbol{\mathcal{L}}) \mathrm{d}V, \quad \text{where} \\ \gamma(d, \nabla d; \boldsymbol{\mathcal{L}}) &= \frac{1}{2l}(d^2 + \nabla d \cdot \boldsymbol{\mathcal{L}} \nabla d)\,, \end{aligned} \tag{3.12}$$

is the *anisotropic crack surface density* function with the condition $\gamma(d, \boldsymbol{Q}\nabla d) = \gamma(d, \nabla d)$, $\forall \boldsymbol{Q} \in \mathcal{G} \subset \mathcal{SO}(3)$, where $\mathcal{G}$ designates a symmetry group as a subset of $\mathcal{SO}(3)$. The second-order anisotropic structure tensor $\boldsymbol{\mathcal{L}}$ is given as

$$\boldsymbol{\mathcal{L}} = l^2(\boldsymbol{I} + \omega_{\mathrm{f}0} \boldsymbol{f}_0 \otimes \boldsymbol{f}_0), \tag{3.13}$$

which aligns the crack with the orientation of fibers in the continuum, see Figure 3.4. Therein, the anisotropy parameter (or in longer version, the anisotropic geometric resistance parameter) ω_{f_0} regulates the geometric anisotropy for the crack topology by scattering the length scale parameter anisotropically over the domain. For isotropic solids $\omega_{\mathrm{f}_0} = 0$, whereas for a general anisotropic continuum, it must lie in an open range, i.e. $-1 < \omega_{\mathrm{f}_0} < \infty$ in order to satisfy the ellipticity condition for $\Gamma_l(d)$, see Gültekin et al. [24] for an elaborate discussion.

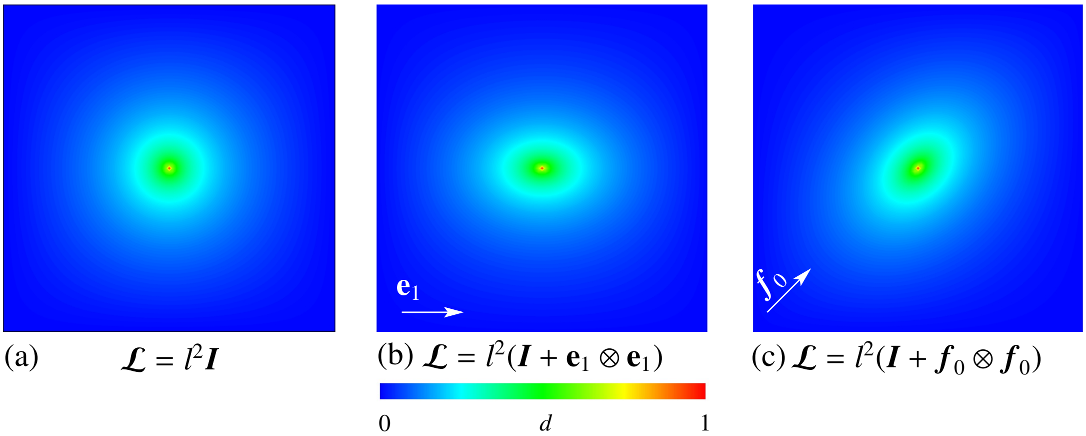

Figure 3.4: Damage field on a square block: (a) isotropic damage field, (b) anisotropic damage field with fiber orientation $\theta = 0°$ stated by the unit base vector $\boldsymbol{e}_1$, (c) anisotropic damage field with fiber orientation $\theta = 45°$ given by the unit vector $\boldsymbol{f}_0$.

3.3 Euler–Lagrange Equations of the Phase–Field Problem

From a purely geometrical perspective, the boundary of the domain under interest can be decomposed into Dirichlet and Neumann-type boundaries such that $\partial\mathcal{B} = \partial\mathcal{B}^d \cup \partial\mathcal{B}^q$ and $\partial\mathcal{B}^d \cap \partial\mathcal{B}^q = \emptyset$. By considering equation 3.12, we can state the minimization principle as

$$d(\boldsymbol{X}) = \text{Arg}\left\{\inf_{d \in \mathcal{W}} \Gamma_l(d)\right\}, \tag{3.14}$$

along with the Dirichlet–type boundary constraint

$$\mathcal{W} = \{d \mid d(\boldsymbol{X}) \in \mathcal{B} \quad \wedge \quad d = \hat{d} \quad \text{on} \quad \partial\mathcal{B}^d\}\,. \tag{3.15}$$

Whilst an already existing crack is given by $\hat{d} = 1$, the intact state is described by $\hat{d} = 0$. Although the boundary value problem admits any meta-states $\hat{d} \in [0, 1]$ on $\partial\mathcal{B}^d$, we confine ourselves for the two ideal states. The Euler-Lagrange equations are obtained after employing the minimization principle as the first variation of the regularized crack surface $\delta\Gamma_l(d)$ to be equal to zero. Applying the minimization to equation 3.11

$$\begin{aligned}\delta\Gamma_l(d) &= \partial_d\Gamma_l(d)\delta d + \partial_{\nabla d}\Gamma_l(d)\nabla\delta d \\ &= \frac{1}{l}\int_{\mathcal{B}}(d\delta d + \underbrace{l^2\nabla d \cdot \nabla\delta d}_{(*)})\mathrm{d}V = 0,\end{aligned} \tag{3.16}$$

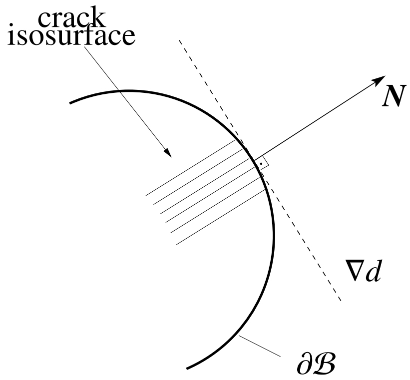

Figure 3.5: Crack isosurface formed perpendicular to the surface for isotropic material.

where $(*)$ can be written by the product rule

$$\nabla \cdot (\nabla d \delta d) = \nabla \cdot \nabla d \delta d + \nabla d \cdot \nabla \delta d \quad \rightarrow \quad \mathrm{DIV}(\nabla d \delta d) = \Delta d \delta d + \nabla d \cdot \nabla \delta d, \quad (3.17)$$

and Δd is the Laplacian of the phase–field, then inserting equation 3.17 into 3.16 gives

$$\begin{aligned} \delta\Gamma_l(d) &= \frac{1}{l}\int_{\mathcal{B}}(d\delta d + l^2\mathrm{DIV}(\nabla d\delta d) - l^2\Delta d\delta d)\mathrm{d}V \\ &= \frac{1}{l}\int_{\mathcal{B}}\underbrace{(d - l^2\Delta d)}_{=0}\delta d\mathrm{d}V + \underbrace{l\int_{\mathcal{B}}\mathrm{DIV}(\nabla d\delta d)\mathrm{d}V}_{(**)}, \end{aligned} \quad (3.18)$$

and applying the Gauss theorem to $(**)$

$$\int_{\mathcal{B}}\mathrm{DIV}(\nabla d\delta d)\mathrm{d}V = \int_{\partial\mathcal{B}}(\nabla d\delta d)\cdot \boldsymbol{N}\mathrm{d}A = \int_{\partial\mathcal{B}}(\nabla d\cdot\boldsymbol{N})\delta d\mathrm{d}A, \quad (3.19)$$

with the $\boldsymbol{N}$ which is the outward normal on $\partial\mathcal{B}$ leads the Euler–Lagrange equations for the 3D isotropic solid

$$\begin{aligned} \frac{1}{l}[d - l^2\Delta d] = 0 \quad &\text{in } \mathcal{B}, \\ \nabla d\cdot\boldsymbol{N} = 0 \quad &\text{on } \partial\mathcal{B}^q. \end{aligned} \quad (3.20)$$

Figure 3.5 demonstrates the crack isosurface perpendicular to the surface for an isotropic solid. Finally, by replacing equation 3.11 with 3.12 the Euler-Lagrange equations of an anisotropic solid is derived in a similar manner

$$\begin{aligned} \frac{1}{l}[d - \mathrm{DIV}(\boldsymbol{\mathcal{L}}\nabla d)] = 0 \quad &\text{in } \mathcal{B}, \\ \boldsymbol{\mathcal{L}}\nabla d\cdot\boldsymbol{N} = 0 \quad &\text{on } \partial\mathcal{B}^q. \end{aligned} \quad (3.21)$$

Solution of the first equations in 3.20 and 3.21 gives the diffusive crack topology and the divergence term interpolates d between the intact and the ruptured state of the material. And the second equation in 3.20 and 3.21 is the Neumann-type boundary condition and $\boldsymbol{N}$ denotes the unit surface normal oriented outward in the reference configuration.

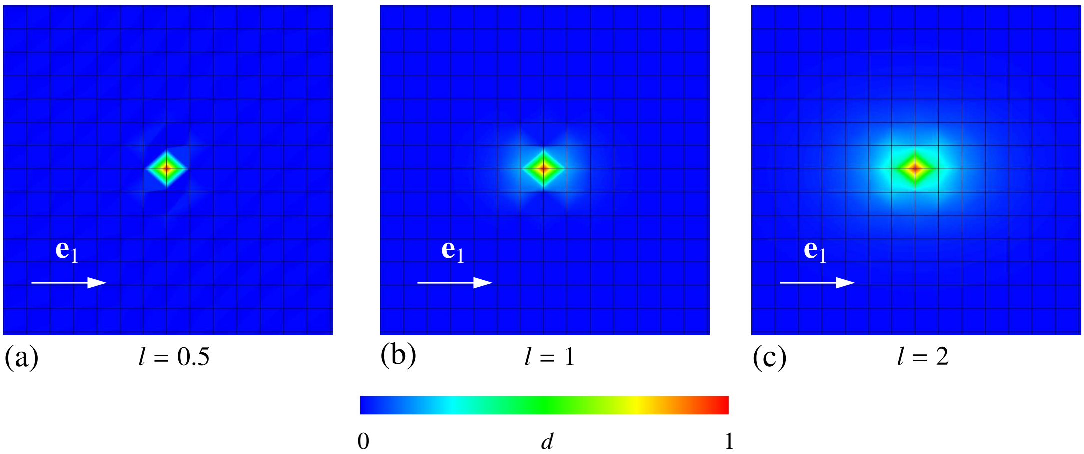

Figure 3.6: Damage field on a 14×14 square block with a single fiber family with $d = 1$ in the middle point and element size $h = 1$: (a) $l = 0.5$, (b) $l = 1$ and for (c) $l = 2$, along with $w_{f_0} = 1$ for all three cases .

Regularization of crack topology for a numerical model problem

We consider a continuum with a sharp crack surface Γ as depicted in Figure 3.2 with Dirichlet condition $d = 1$ on the crack surface Γ, and $\nabla d \cdot \boldsymbol{N} = 0$ on the boundary $\partial\mathcal{B}$ for the crack phase–field. The finite element solution of the crack phase–field d in the domain $\mathcal{B}$ could be done by the linear solution procedure provided in Gültekin et al. [24] for the different values of the length scale parameter l. It is important to determine the adequate element mesh size h in order to resolve the length scale. In the studies of Miehe et al. [34] it is shown that the element size h should be smaller than $l/2$, so that the regularize crack surface $\Gamma_l(d)$ approximates the sharp crack surface Γ closely enough with the finite element approximation. Therein, it is reported that mesh convergence is achieved for $l \geq 2h$.

To illustrate only the visual resolution, the phase–field problem is solved in the purely geometrical context for a 2–D square block (14×14) with $\hat{d} = 1$ at the single centroidal point and $\mathcal{L}\nabla d = 0$ on the sides of the block. The square block has horizontal

$$\mathcal{L} = l^2(\boldsymbol{I} + \omega_{\mathrm{f}_0}\mathbf{e}_1 \otimes \mathbf{e}_1) = l^2 \begin{bmatrix} 1 + \omega_{\mathrm{f}_0} & 0 & 0 \\ 0 & 1 & 0 \\ 0 & 0 & 1 \end{bmatrix}$$

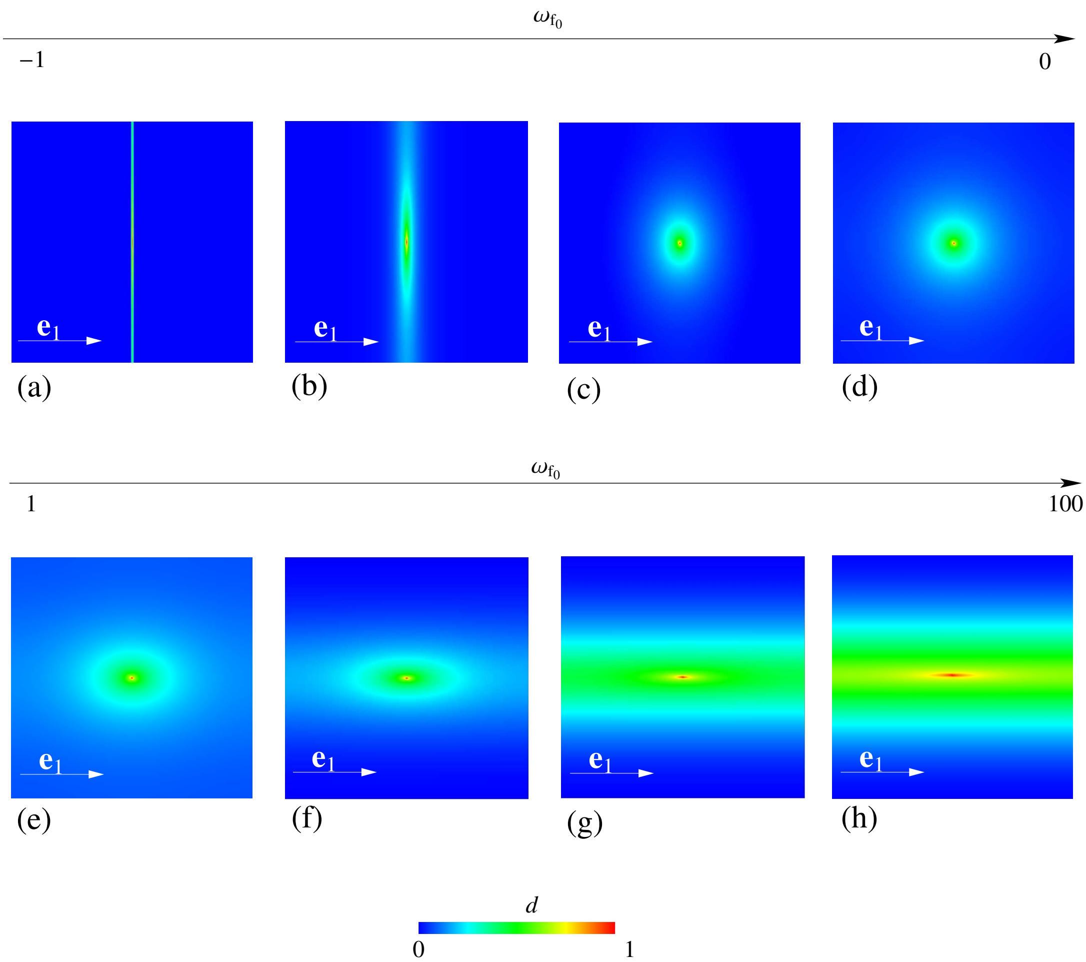

Figure 3.7: Damage field on a 100×100 square block: (a) $\omega_{\mathrm{f}_0} = -1$, (b) $\omega_{\mathrm{f}_0} = -0.99$, (c) $\omega_{\mathrm{f}_0} = -0.5$, (d) $\omega_{\mathrm{f}_0} = 0$, (e) $\omega_{\mathrm{f}_0} = 1$, (f) $\omega_{\mathrm{f}_0} = 5$, (g) $\omega_{\mathrm{f}_0} = 30$, (h) $\omega_{\mathrm{f}_0} = 100$, with fiber orientation $\theta = 0°$ stated by the unit base vector $\boldsymbol{e}_1$, $h = 1$ and, length scale parameter $l = 60$.

fiber orientation and is discretized with element size of $h = 1$. The anisotropy parameter taken as $\omega_{\mathrm{f}_0} = 1$ and the problem is solved for three different l values which are $l = h/2$, $l = h$ and $l = 2h$. Figure 3.6 shows the resulting damage field resolutions of the three cases, the resolution which can demonstrate the affect of existing fibers on the damage field is achieved for $l/h = 2$.

Followed by, 2–D square block (100×100) is solved to demonstrate the effect of var-

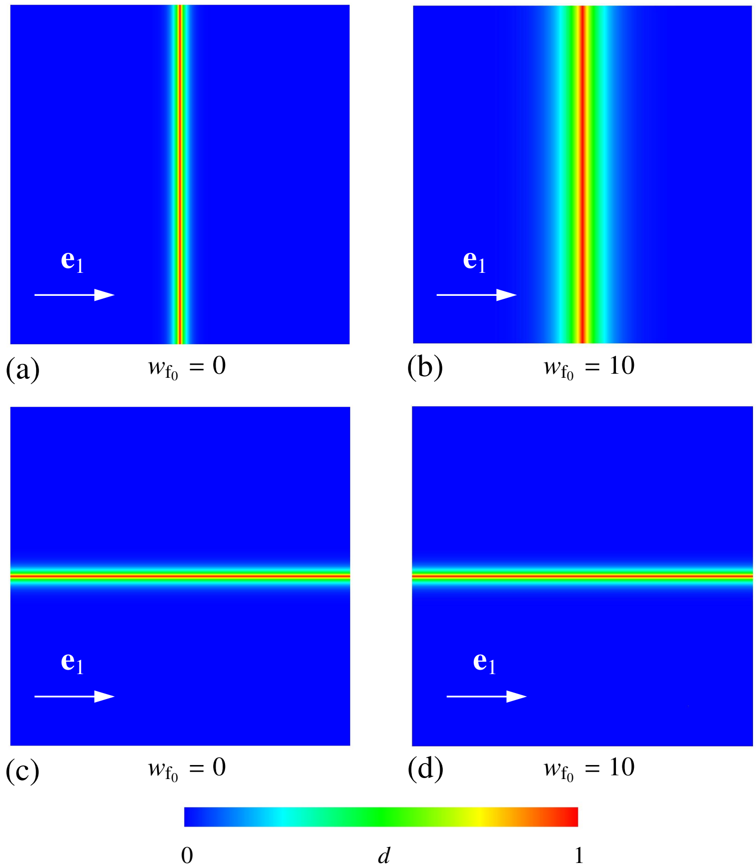

Figure 3.8: Damage field on a square block with a single fiber family whose orientation is characterized by the unit base vector $\boldsymbol{e}_1$: (a),(b) for a vertical centroidal crack; (c),(d) for a centroidal horizontal crack where $w_{f_0} = 0$ in the first column and $w_{f_0} = 10$ in the second column.

ious structure tensors $\boldsymbol{\mathcal{L}}$ associated with different fiber orientations and the resulting damage fields are depicted in Figure 3.4. And by setting the fiber orientation to $\boldsymbol{e}_1$, $h = 1$, and $l = 60$, the same problem is solved with different ω_{f_0} values which cover the whole range of ω_{f_0} and its limit value -1 which turns the elliptical damage surface in to a line, and the damage fields related to these values are shown in Figure 3.7. For positive values of ω_{f_0}, the damage field smears in the direction of fibers (see Figure 3.7 (e), (f), (g), (h)), however, for negative values of ω_{f_0} the situation is the vice versa and the damage field smears in the transverse direction to fibers (see Figure 3.7 (b), (c)), and when $\omega_{f_0} = -1$, the non-local part of the $\boldsymbol{\mathcal{L}}$ becomes zero (disappear) and the function turns into Dirac delta function and the damage field becomes a vertical line, which is transverse to fiber direction and not elliptical anymore.

In order to demonstrate the influence of w_{f_0} with line cracks, four representative cracks for two different anisotropy factors, namely $w_{f_0} = 0$ in Figure 3.8(a),(c) and $w_{f_0} = 10$ in Figure 3.8(b),(d) are depicted. The introduced centroidal cracks ($\hat{d} = 1$) are vertical in the first and horizontal in the second row. When the anisotropy parameter equals to zero, i.e $w_{f_0} = 0$, the crack smears isotropically so that the geometric resistance to crack propagation is identical in all directions. However, $w_{f_0} = 10$ smears the crack considerably more in the transverse plane towards the fiber direction $\boldsymbol{e}_1$, see Figure 3.8(b), whereas the minimum smearing occurs around the cracks parallel to the fiber direction, see Figure 3.8(d), as observed in the second column. This means that cracks propagating across the fibers are penalized and the crack propagating along the fibers are favored. This is due to the fact that the energy threshold for the cracks propagating across the fibers are higher for $w_{f_0} > 0$. The converse applies for $-1 < w_{f_0} < 0$.

CHAPTER 4

GOVERNING EQUATIONS OF THE ANISOTROPIC FRACTURE

This chapter deals with the coupled equations of the elastic–fracture problem for finite and small strains, where the classical balance of linear momentum is accompanied by the evolution equation of the crack phase–field; the strong forms of the boundary–value problem are presented.

4.1 Rate–Dependent Variational Formulation Based on Power Balance

4.1.1 Finite Strain Setting

As a point of departure, the viscous rate–type potential Π_η is introduced as

$$\Pi_\eta = \mathcal{E} + \mathcal{D}_\eta - \mathcal{P}. \tag{4.1}$$

The first term $\mathcal{E}$ on the right–hand side of equation 4.1 represents the rate of energy storage functional, which is the time derivative of the energy storage functional E of an anisotropic solid i.e.

$$E(\boldsymbol{\varphi}, d) := \int_{\mathcal{B}} \Psi(\boldsymbol{g}, \boldsymbol{F}, \boldsymbol{A}_f; d)\mathrm{d}V. \tag{4.2}$$

The time derivative of function 4.2 gives

$$\mathcal{E}(\dot{\boldsymbol{\varphi}}; \dot{d}) = \int_{\mathcal{B}} (\boldsymbol{P} : \dot{\boldsymbol{F}} - f\dot{d})\mathrm{d}V, \tag{4.3}$$

where the work conjugate variables to $\boldsymbol{\varphi}$ and d are the first Piola–Kirchhoff stress tensor $\boldsymbol{P}$ and the scalar energetic force f, respectively, i.e.

$$\boldsymbol{P} = \partial_{\boldsymbol{F}} \Psi(\boldsymbol{g}, \boldsymbol{F}, \boldsymbol{A}_f; d), \qquad f = -\partial_d \Psi(\boldsymbol{g}, \boldsymbol{F}, \boldsymbol{A}_f; d). \tag{4.4}$$

The free–energy function Ψ defined in (4.4) characterizes a degrading continuum with

$$\Psi(\boldsymbol{g}, \boldsymbol{F}, \boldsymbol{A}_f; d) := g(d)\Psi_0(\boldsymbol{g}, \boldsymbol{F}, \boldsymbol{A}_f), \tag{4.5}$$

where Ψ_0 is the effective free–energy function of the hypothetically intact solid. In (4.5), a monotonically decreasing quadratic degradation function, i.e.

$$g(d) := (1 - d)^2, \tag{4.6}$$

describes the degradation of the solid with the evolving crack phase–field parameter d together with the following growth conditions:

$$g'(d) \leq 0 \quad \text{with} \quad g(0) = 1,\ g(1) = 0,\ g'(1) = 0. \tag{4.7}$$

The first condition ensures degradation, while the second and third condition set the limits for the intact and the ruptured state, and the final condition ensures the saturation at $d \to 1$. Having determine the degradation function $g(d)$, the scalar energetic force f is defined as follows:

$$f = -\partial_d[g(d)\Psi_0(\boldsymbol{g}, \boldsymbol{F}, \boldsymbol{A}_f)] = -\partial_d g(d)\Psi_0(\boldsymbol{g}, \boldsymbol{F}, \boldsymbol{A}_f) = 2(1 - d)\Psi_0 \tag{4.8}$$

The second term $\mathcal{D}_\eta$ on the right–hand side of equation 4.1 is a viscous regularized dissipation functional due to fracture, i.e.

$$\mathcal{D}_\eta(\dot{d}, \beta; d) = \int_{\mathcal{B}} [\beta\dot{d} - \frac{1}{2\eta}\langle\chi(\beta; d, \nabla d)\rangle^2]\mathrm{d}V, \tag{4.9}$$

where the artificial viscosity $\eta \geq 0$ regulates the scalar viscous over–stress χ, which reads

$$\chi(\beta; d, \nabla d) = \beta - g_c[\delta_d\gamma(d, \nabla d; \boldsymbol{\mathcal{L}})], \tag{4.10}$$

with local driving force β and the variational derivative of the crack surface density function

$$\delta_d\gamma = \frac{1}{l}[d - \mathrm{DIV}(\boldsymbol{\mathcal{L}}\nabla d)]. \tag{4.11}$$

The Macaulay brackets in (4.9) filter out the positive values, $\chi > 0$, while g_c in (4.10) stands for the critical fracture energy.

Finally, the last term $\mathcal{P}$ on the right–hand side of (4.1) denotes the (classical) external power functional acting on the body according to

$$\mathcal{P}(\dot{\boldsymbol{\varphi}}) = \int_{\mathcal{B}} \rho_0\boldsymbol{B} \cdot \dot{\boldsymbol{\varphi}}\mathrm{d}V + \int_{\partial\mathcal{B}_t} \overline{\boldsymbol{T}} \cdot \dot{\boldsymbol{\varphi}}\mathrm{d}A, \tag{4.12}$$

where ρ_0, $\boldsymbol{B}$ and $\overline{\boldsymbol{T}}$ represent the material density, the prescribed body force and the surface traction, respectively. Enforcing the Gauss theorem to the second term in equation 4.12 gives

$$\int_{\partial\mathcal{B}_t} \overline{\boldsymbol{T}} \cdot \dot{\boldsymbol{\varphi}} \mathrm{d}A = \int_{\partial\mathcal{B}_t} (\boldsymbol{PN}) \cdot \dot{\boldsymbol{\varphi}} \mathrm{d}A = \int_{\mathcal{B}} \mathrm{DIV}(\boldsymbol{P} \cdot \dot{\boldsymbol{\varphi}}) \mathrm{d}V = \int_{\mathcal{B}} [\boldsymbol{P} : \dot{\boldsymbol{F}} + \mathrm{DIV}(\boldsymbol{P}) \cdot \dot{\boldsymbol{\varphi}}] \mathrm{d}V. \tag{4.13}$$

By adding up all the given three functions Π_η is define as

$$\begin{aligned} \Pi_\eta &= \int_{\mathcal{B}} [\boldsymbol{P} : \boldsymbol{F} - f\dot{d} + \beta\dot{d} - \frac{1}{2\eta}\langle\chi\rangle^2 - \rho_0 \boldsymbol{B} \cdot \dot{\boldsymbol{\varphi}} - \boldsymbol{P} : \dot{\boldsymbol{F}} - \mathrm{DIV}(\boldsymbol{P}) \cdot \dot{\boldsymbol{\varphi}}] \mathrm{d}V \\ &= \int_{\mathcal{B}} [(\beta - f)\dot{d} - [\rho_0 \boldsymbol{B} + \mathrm{DIV}(\boldsymbol{P})] \cdot \dot{\boldsymbol{\varphi}} - \frac{1}{2\eta}\langle\chi\rangle^2] \mathrm{d}V, \end{aligned} \tag{4.14}$$

Now, with the rate–type potential Π_η at hand, mixed variational principle of the evolution problem is proposed as follows

$$\{\dot{\boldsymbol{\varphi}}, \dot{d}, \beta\} = \mathrm{Arg}\left\{ \inf_{\dot{\boldsymbol{\varphi}} \in \mathcal{W}_{\dot{\varphi}}} \inf_{\dot{d} \in \mathcal{W}_{\dot{d}}} \sup_{\beta \geq 0} \Pi_\eta \right\}, \tag{4.15}$$

with the admissible domains for the primary variables

$$\begin{aligned} \mathcal{W}_{\dot{\varphi}} &= \{\dot{\boldsymbol{\varphi}} \mid \dot{\boldsymbol{\varphi}} = \boldsymbol{0} \quad \text{on} \quad \partial\mathcal{B}_\varphi\}, \\ \mathcal{W}_{\dot{d}} &= \{\dot{d} \mid \dot{d} = 0 \quad \text{on} \quad \partial\mathcal{B}_d\}. \end{aligned} \tag{4.16}$$

The variation of the potential Π_η with respect to the fields $\{\dot{\boldsymbol{\varphi}}, \dot{d}, \beta\}$ yields the coupled field equations

$$\begin{aligned} &1: \quad \mathrm{DIV}(\boldsymbol{P}) + \rho_0 \boldsymbol{B} = \boldsymbol{0}, \\ &2: \quad \beta - f = 0, \\ &3: \quad \dot{d} - \frac{1}{\eta}\langle\chi\rangle = 0, \end{aligned} \tag{4.17}$$

then, an elimination is done using equations 4.8, 4.10 and 4.17

$$\beta = f = 2(1 - d)\Psi_0 \quad \text{and} \quad \chi = \beta - g_c \delta_d \gamma = \eta \dot{d}. \tag{4.18}$$

After substitution of the respective terms, strong form of the field equations are given as

$$\boxed{\begin{aligned} &1: \ \mathrm{DIV}\boldsymbol{P} + \rho_0 \boldsymbol{B} = \boldsymbol{0}, \\ &2: \ \eta\dot{d} = 2(1 - d)\overline{\mathcal{H}} - d + \mathrm{DIV}(\boldsymbol{\mathcal{L}}\nabla d). \end{aligned}} \tag{4.19}$$

The first equation in 4.19 simply describes the balance of linear momentum, whereas the latter states the evolution equation for the crack phase–field in which $\overline{\mathcal{H}}$ indicates the crack driving source term such that

$$\overline{\mathcal{H}} = \frac{\Psi_0}{g_c/l}. \tag{4.20}$$

The evolution of the phase–field parameter can be recast into the form

$$\boxed{\dot{d} = \frac{1}{\eta}[2(1-d)\bar{\mathcal{H}} - d + \nabla d \cdot \boldsymbol{\mathcal{L}} \nabla d],} \tag{4.21}$$

4.1.2 Small Strain Setting

The displacement field $\boldsymbol{u} = \boldsymbol{x} - \boldsymbol{X}$ is described at a material point $\boldsymbol{X} \in \mathcal{B} \subset \mathbb{R}^3$ and at time $t \in \mathcal{T}$, i.e.

$$\boldsymbol{u}(\boldsymbol{X}, t) : \begin{cases} \mathcal{B} \times \mathcal{T} & \to & \mathbb{R}^3, \\ (\boldsymbol{X}, t) & \mapsto & \boldsymbol{u}(\boldsymbol{X}, t). \end{cases} \tag{4.22}$$

The rate of energy storage functional $\mathcal{E}$ on the right–hand side of (4.1) in the small-strain setting reads

$$\mathcal{E}(\dot{\boldsymbol{u}}; \dot{d}) = \int_{\mathcal{B}} (\boldsymbol{\sigma} : \dot{\boldsymbol{\varepsilon}} - f\dot{d})\mathrm{d}V, \tag{4.23}$$

where the stress tensor $\boldsymbol{\sigma}$ is the work conjugate variable of the small-strain measure $\boldsymbol{\varepsilon} = \operatorname{sym} \nabla \boldsymbol{u}$. In equation 4.23, the energetic force f appears as the work conjugate of the damage variable d. The stress tensor $\boldsymbol{\sigma}$ and the scalar energetic force f are then expressed as

$$\boldsymbol{\sigma} = \partial_{\boldsymbol{\varepsilon}} \Psi(\boldsymbol{\varepsilon}, \boldsymbol{A}; d), \qquad f = -\partial_d \Psi(\boldsymbol{\varepsilon}, \boldsymbol{A}; d). \tag{4.24}$$

The term f can also be interpreted as the local crack driving force. The free–energy function Ψ in equation 4.24 characterizes a degrading continuum with

$$\Psi(\boldsymbol{\varepsilon}, \boldsymbol{A}; d) := g(d)\Psi_0(\boldsymbol{\varepsilon}, \boldsymbol{A}), \tag{4.25}$$

where Ψ_0 is the effective free–energy function of the hypothetically intact solid. The regularized dissipation functional (equation 4.9) and the scalar viscous over–stress function (equation 4.10) remain unchanged. Finally, the (classical) external power functional $\mathcal{P}$ stated on the right–hand side of the equation 4.1 can now be written in the form

$$\mathcal{P}(\dot{\boldsymbol{u}}) = \int_{\mathcal{B}} \rho_0 \boldsymbol{B} \cdot \dot{\boldsymbol{u}} \mathrm{d}V + \int_{\partial \mathcal{B}_t} \overline{\boldsymbol{T}} \cdot \dot{\boldsymbol{u}} \mathrm{d}A, \tag{4.26}$$

where ρ_0, $\boldsymbol{B}$ and $\overline{\boldsymbol{T}}$ represent the material density, the prescribed body force and the surface traction, respectively. With the expressions for the rate–type potential Π_η at hand, a mixed variational principle of the evolution problem is proposed as follows

$$\{\dot{\boldsymbol{u}}, \dot{d}, \beta\} = \operatorname{Arg}\left\{ \inf_{\dot{\boldsymbol{u}} \in \mathcal{W}_{\dot{u}}} \inf_{\dot{d} \in \mathcal{W}_{\dot{d}}} \sup_{\beta \geq 0} \Pi_\eta \right\}, \tag{4.27}$$

with the admissible domains for the primary variables

$$\begin{aligned} \mathcal{W}_{\dot{u}} &= \{\dot{\boldsymbol{u}} \mid \dot{\boldsymbol{u}} = \boldsymbol{0} \quad \text{on} \quad \partial\mathcal{B}_u\}, \\ \mathcal{W}_{\dot{d}} &= \{\dot{d} \mid \dot{d} = 0 \quad \text{on} \quad \partial\mathcal{B}_d\}. \end{aligned} \tag{4.28}$$

Afterwards, the variation of the potential Π_η with respect to the fields $\{\dot{\boldsymbol{u}}, \dot{d}, \beta\}$ and substitution of the respective terms (see Miehe et al. [34] for more details) we obtain the strong form of the field equations, i.e.

$$\boxed{\begin{aligned} &1\text{:}\;\; \mathrm{DIV}\boldsymbol{\sigma} + \rho_0 \boldsymbol{B} = \boldsymbol{0}, \\ &2\text{:}\;\; \eta \dot{d} = 2(1-d)\overline{\mathcal{H}} - d + \mathrm{DIV}(\boldsymbol{\mathcal{L}} \nabla d). \end{aligned}} \tag{4.29}$$

4.2 A Note on the Weak Formulation and Numerical Implementation

On the numerical side, a canonical Galerkin-type finite element procedure renders the weak forms of the coupled balance equations given in equation 4.19. The non-linearities due to the geometry and the constitutive law, as subsequently described, necessitates a linearization process employed on the weak forms. Afterwards, an identical temporal and spatial discretization scheme is employed for the deformation map and the crack phase–field. The field variables are appropriately discretized with isoparametric shape functions so as to transform the continuous integral equations of the nonlinear weighted-residuals and their linearizations to a set of coupled, discrete algebraic equations. Finally, this set of algebraic equations is solved by a one–pass operator–splitting algorithm in a Newton-type iterative solver that successively updates the history field described by the failure criterion, the crack phase–field and the deformation field. For a more elaborate numerical treatment of the respective problem, the readers are referred to, e.g., Gültekin et al. [23, 24].

CHAPTER 5

CONSTITUTIVE EQUATIONS OF THE MULTI–FIELD PROBLEM

In this chapter, (i) the constitutive equations that capture the nonlinear anisotropic response of a UD FRP composite and (ii) the related energy–based anisotropic failure criterion capturing the state of the material at which the cracking starts/propagates is described.

5.1 The Constitutive Model for the UD FRP Composites

The free–energy function of isotropic solids can be modeled through the three invariants I_1, I_2, I_3, which constitute the integrity basis of the deformation tensors $\boldsymbol{C}$ or $\boldsymbol{b}$, see e.g., Spencer [52]. For incompressible materials the two invariants I_1 and I_2 are enough to describe the isotropic deformation.

For transversely anisotropic solids, one can introduce the additional set of invariants I_4 and I_5 with the help of the structural tensors that satisfy the objectivity requirement under superimposed rigid body rotations, see e.g., Betten [7], Boehler [9] and Schröder & Neff [50]. In UD fiber–reinforced materials, the stored energy can be obtained in terms of a free energy of the unreinforced base matrix with the arguments I_1 and I_3 augmented by a storage function that involves the fourth invariant I_4 related to the fiber stretch. The latter function is also known as the *standard reinforcing model*, see Qiu & Pence [46]. A similar approach can be adopted for the modeling of soft biological tissues, see, e.g., Holzapfel et al. [28].

To characterize the local anisotropic mechanical response of a UD FRP composite, the free–energy function can be stated as

$$\Psi_0(\boldsymbol{g}, \boldsymbol{F}, \boldsymbol{A}_f) := \Psi_0^{\text{iso}}(J, I_1) + \Psi_0^{\text{ani}}(I_4). \tag{5.1}$$

For the isotropic part of the mechanical response of the compressible polymer matrix we adopt the generic compressible neo-Hookean free–energy function. Thus,

$$\Psi_0^{\text{iso}}(J, I_1) := \frac{\lambda}{2}(\ln J)^2 + \frac{\mu}{2}(I_1 - 2\ln J - 3). \tag{5.2}$$

For the anisotropic part we use the standard reinforcing model in the sense of Qiu & Pence [46], i.e.

$$\Psi_0^{\text{ani}}(I_4) := \frac{\mu_{\text{f}}}{4}(I_4 - 1)^2. \tag{5.3}$$

In equation 5.2, λ denotes the *Lamé's first constant*, whereas μ denotes the *Lamé's second constant* or the *shear modulus*. In the anisotropic term of the equation 5.3, μ_{f} stands for a stress-like material parameter associated solely with the fibrous content.

The Coleman–Noll procedure is exploited on the Clausius–Planck inequality, and the form of the free–energy function Ψ is used, as introduced in equation 4.5, so that the Kirchhoff stress tensor $\boldsymbol{\tau}$ can be retrieved as

$$\boldsymbol{\tau} := \boldsymbol{P}\boldsymbol{F}^{\text{T}} = 2\partial_{\boldsymbol{g}}\Psi = g(d)\boldsymbol{\tau}_0, \qquad \boldsymbol{\tau}_0 = 2\partial_{\boldsymbol{g}}\Psi_0. \tag{5.4}$$

Therein, $g(d)$ is a monotonically decreasing quadratic degradation function as provided in equation 4.6. For the relevant nonlinear continuum mechanics used see, e.g., Holzapfel [28]. By substituting equation 5.1 along with the equations 5.2 and 5.3 into the definition given in the equation 5.4_2 the stress expression for the intact material is obtained, i.e.

$$\begin{aligned} \boldsymbol{\tau}_0 &= \boldsymbol{\tau}_0^{\text{iso}} + \boldsymbol{\tau}_0^{\text{ani}} \\ \boldsymbol{\tau}_0^{\text{iso}} &= 2\partial_{\boldsymbol{g}}\Psi_0^{\text{iso}} = 2\lambda\ln J\frac{1}{J}\partial_{\boldsymbol{g}}J + \mu(\partial_{\boldsymbol{g}}I_1 - 2\frac{1}{J}\partial_{\boldsymbol{g}}J) \\ \boldsymbol{\tau}_0^{\text{ani}} &= 2\partial_{\boldsymbol{g}}\Psi_0^{\text{ani}} = \mu_{\text{f}}(I_4 - 1)\partial_{\boldsymbol{g}}I_4, \end{aligned} \tag{5.5}$$

where $\partial_{\boldsymbol{g}}J$, $\partial_{\boldsymbol{g}}I_1$ and $\partial_{\boldsymbol{g}}I_4$ are define as

$$\partial_{\boldsymbol{g}}J = \frac{1}{2}J\boldsymbol{g}^{-1} \quad , \quad \partial_{\boldsymbol{g}}I_1 = \boldsymbol{b} \quad , \quad \partial_{\boldsymbol{g}}I_4 = \boldsymbol{f}\otimes\boldsymbol{f} \tag{5.6}$$

with $\dfrac{\partial(*)}{\partial\boldsymbol{g}} = \boldsymbol{F}\dfrac{\partial(*)}{\partial\boldsymbol{C}}F^T$. After substituting equation 5.6 into 5.5 the stress expression for the intact material is defined as

$$\boldsymbol{\tau}_0 = \lambda\ln J\boldsymbol{g}^{-1} + \mu(\boldsymbol{b} - \boldsymbol{g}^{-1}) + 2\psi_4\boldsymbol{f}\otimes\boldsymbol{f}, \tag{5.7}$$

where the (deformation-dependent) constitutive function ψ_4 have been introduced by

$$\psi_4 := \partial_{I_4}\Psi_0 = \frac{\mu_{\mathrm{f}}}{2}(I_4 - 1). \tag{5.8}$$

The change in the Kirchhoff stress tensor is provided by the elasticity tensor here given in the spatial form as

$$\mathbb{C} := 4\partial^2_{\boldsymbol{gg}}\Psi = g(d)\mathbb{C}_0, \qquad \mathbb{C}_0 = 4\partial^2_{\boldsymbol{gg}}\Psi_0, \tag{5.9}$$

with

$$\begin{aligned}
&\mathbb{C}_0 = \mathbb{C}_0^{\mathrm{iso}} + \mathbb{C}_0^{\mathrm{ani}} \\
&\mathbb{C}_0^{\mathrm{iso}} = 2\partial_{\boldsymbol{g}}\tau_0^{\mathrm{iso}} = 2\lambda\frac{1}{J}\partial_{\boldsymbol{g}}J\boldsymbol{g}^{-1} + 2\lambda\ln J\partial_{\boldsymbol{g}}\boldsymbol{g}^{-1} + 2\mu(\partial_{\boldsymbol{g}}b - \partial_{\boldsymbol{g}}\boldsymbol{g}^{-1}) \\
&\mathbb{C}_0^{\mathrm{ani}} = 2\partial_{\boldsymbol{g}}\tau_0^{\mathrm{ani}} = 2\mu_{\mathrm{f}}\partial_{\boldsymbol{g}}I_4\boldsymbol{f}\otimes\boldsymbol{f}.
\end{aligned} \tag{5.10}$$

After the substitutions from equation 5.6 and the definition of $-\partial_{\boldsymbol{g}}\boldsymbol{g}^{-1} = \mathbb{I}_{\boldsymbol{g}^{-1}}$ with $\partial_{\boldsymbol{g}}b = 0$, the effective elasticity tensor $\mathbb{C}_0$ has the explicit expression

$$\mathbb{C}_0 = \lambda\boldsymbol{g}^{-1}\otimes\boldsymbol{g}^{-1} + 2(\mu - \lambda\ln J)\mathbb{I}_{\boldsymbol{g}^{-1}} + 4\psi_{44}\mathbb{M}, \tag{5.11}$$

where the symmetric fourth-order identity tensor $\mathbb{I}_{\boldsymbol{g}^{-1}}$ has the index representation $(\mathbb{I}_{\boldsymbol{g}^{-1}})^{ijkl} = (\delta^{ik}\delta^{jl} + \delta^{il}\delta^{jk})/2$. In addition, the constitutive function ψ_{44} reads

$$\psi_{44} := \partial_{I_4}\psi_4 = \frac{\mu_{\mathrm{f}}}{2}, \tag{5.12}$$

and the fourth-order structure tensor takes on the following form

$$\mathbb{M} := \boldsymbol{f}\otimes\boldsymbol{f}\otimes\boldsymbol{f}\otimes\boldsymbol{f}. \tag{5.13}$$

5.2 Linearization of the Constitutive Model: Small-Strain Setting

The linearized form of the free–energy function given in equation 5.1 can be represented as

$$\Psi_0(\boldsymbol{\varepsilon}, \boldsymbol{A}) := \Psi_0^{\mathrm{iso}}(\boldsymbol{\varepsilon}) + \Psi_0^{\mathrm{ani}}(\boldsymbol{\varepsilon}, \boldsymbol{A}). \tag{5.14}$$

The isotropic and the anisotropic parts take on the simple quadratic forms

$$\begin{aligned}
\Psi_0^{\mathrm{iso}}(\boldsymbol{\varepsilon}) &:= \frac{\lambda}{2}(\mathrm{tr}\,\boldsymbol{\varepsilon})^2 + \mu(\boldsymbol{\varepsilon} : \boldsymbol{\varepsilon}), \\
\Psi_0^{\mathrm{ani}}(I_4) &:= \mu_{\mathrm{f}}(\boldsymbol{\varepsilon} : \boldsymbol{A})^2.
\end{aligned} \tag{5.15}$$

The linear stress tensor $\boldsymbol{\sigma}_o := \partial_{\boldsymbol{\varepsilon}}\Psi_0$ of the intact solid can then be derived from the equation 5.15, i.e.

$$\boldsymbol{\sigma}_0 = \lambda(\operatorname{tr}\boldsymbol{\varepsilon})\mathbf{1} + 2\mu\boldsymbol{\varepsilon} + 2\mu_{\mathrm{f}}(\boldsymbol{\varepsilon} : \boldsymbol{A})\boldsymbol{A}. \tag{5.16}$$

The related elasticity moduli $\mathbb{C}_0 = \partial_{\boldsymbol{\varepsilon}}\boldsymbol{\sigma}_0$ of the intact solid can be derived as

$$\mathbb{C}_0 = \lambda\mathbf{1}\otimes\mathbf{1} + 2\mu\mathbb{I} + 2\mu_{\mathrm{f}}\boldsymbol{A}\otimes\boldsymbol{A}. \tag{5.17}$$

Therein, the fourth order symmetric identity tensor $\mathbb{I}$ has the following index representation ($\mathbb{I}^{ijkl} = (\delta^{ik}\delta^{jl} + \delta^{il}\delta^{jk})/2$. The proposed Ansatz is the simplest form of transverse isotropy with only one additional material parameter μ_{f} to describe the axial reinforcement due to UD fibers. This particular choice assumes identical shear response in the planes including the fibers and the transverse plane. It also excludes the coupling effect between the bulk response and the fiber reinforcement.

5.3 Energy–Based Anisotropic Failure Criterion

Following Gültekin et al. [23, 24], it is started with the assumption that two distinct failure processes govern the cracking of the ground matrix and the fibers, whereby the anisotropic structure tensor $\boldsymbol{\mathcal{L}}$ in equation 3.13 is additively decomposed as

$$\begin{gathered}\boldsymbol{\mathcal{L}} = \boldsymbol{\mathcal{L}}^{\mathrm{iso}} + \boldsymbol{\mathcal{L}}^{\mathrm{ani}} \quad \text{with} \\ \boldsymbol{\mathcal{L}}^{\mathrm{iso}} = l^2\boldsymbol{I}, \quad \text{and} \quad \boldsymbol{\mathcal{L}}^{\mathrm{ani}} = l^2\omega_{\mathrm{f}_0}\boldsymbol{f}_0\otimes\boldsymbol{f}_0.\end{gathered} \tag{5.18}$$

Next $g_{\mathrm{c}}^{\mathrm{iso}}$ and $g_{\mathrm{c}}^{\mathrm{ani}}$ are introduced corresponding to the critical fracture energies attributed to the ground–matrix (isotropic) and the fibrous content (anisotropic) of FRP, respectively, which homogenize the distinct mechanical resistance of the respective interactions against rupture. Hence, the crack driving source term given in equation 4.20 can be decomposed as

$$\overline{\mathcal{H}}^{\mathrm{iso}} = \frac{\Psi_0^{\mathrm{iso}}}{g_{\mathrm{c}}^{\mathrm{iso}}/l}, \qquad \overline{\mathcal{H}}^{\mathrm{ani}} = \frac{\Psi_0^{\mathrm{ani}}}{g_{\mathrm{c}}^{\mathrm{ani}}/l}. \tag{5.19}$$

For the rate–independent case for which $\eta \to 0$, the expressions defined in equations 5.18 and 5.19 engender distinct evolution equations of the crack phase–field in relation to the ground–matrix and the fibrous content, i.e.

$$
\begin{aligned}
2(1-d)\overline{\mathcal{H}}^{\text{iso}} &= d - \text{DIV}(\boldsymbol{\mathcal{L}}^{\text{iso}}\nabla d),\\
2(1-d)\overline{\mathcal{H}}^{\text{ani}} &= d - \text{DIV}(\boldsymbol{\mathcal{L}}^{\text{ani}}\nabla d).
\end{aligned} \tag{5.20}
$$

What remains is to superpose the two distinct failure processes in equation 5.20, which leads to the rate–independent evolution equation of the phase–field, i.e.

$$
\boxed{(1-d)\mathcal{H} = d - \frac{1}{2}\text{DIV}(\boldsymbol{\mathcal{L}}\nabla d),} \tag{5.21}
$$

along with the specific form of the dimensionless crack driving source term

$$
\boxed{\begin{aligned}
&\mathcal{H}(t) = \max\nolimits_{s\in[0,t]}\left[\langle\overline{\mathcal{H}}(s)-1\rangle\right],\\
&\overline{\mathcal{H}} = \overline{\mathcal{H}}^{\text{iso}} + \overline{\mathcal{H}}^{\text{ani}}.
\end{aligned}} \tag{5.22}
$$

Relation in equation 5.22 indicates an irreversible and positive crack driving source term such that the maximum positive value of $\overline{\mathcal{H}}(s) - 1$ is tracked down for the entire deformation history $s \in [0, t]$. The Macaulay brackets filter out the positive values for $\overline{\mathcal{H}}(s) - 1$ and keeps the solid intact until the failure surface is reached, which denotes the energetic criterion proposed by Gültekin et al. [23, 24]. Finally, in view of equation 5.21, we specify the rate–dependent case, i.e.

$$
\boxed{\underbrace{\eta\dot{d}}_{\text{Crack evolution}} = \underbrace{(1-d)\mathcal{H}}_{\text{Driving force}} - \underbrace{[d - \frac{1}{2}\text{DIV}(\boldsymbol{\mathcal{L}}\nabla d)]}_{\text{Geometric resistance}},} \tag{5.23}
$$

where the evolution of the crack is characterized by the balance between the crack driving force and the geometric resistance to the crack, see Miehe et al. [36]. A closer examination of equation 5.23 shows that the geometric resistance is directional dependent. In Figure 3.8, for instance, the energy threshold ratio of the crack in the direction $\boldsymbol{f}_0$ to that in the transverse direction to $\boldsymbol{f}_0$ is $G_{\parallel}/G_{\perp} = \mathcal{L}_{11}/\mathcal{L}_{22} = (w_{\text{f}_0}+1)/1$ leading to an isotropic crack resistance for $w_{\text{f}_0} = 0$.

5.4 Extention of Constitutive Model to Two Fiber Family Composites

Although the main focus of this thesis is unidirectional fiber composites, in this section we extend our model to composites with two fiber families. Here we give only the kinematic relations, constitutive equations and the failure criteria. The numerical examples and the correlated results with the test data can be defined as future work.

Since there are two fiber families there will be two reference unit vectors which define as $\boldsymbol{f}_0$ and $\boldsymbol{f}'_0$, representing the mean fiber orientations related to each fiber family, and their Eulerian counterparts are written as

$$\boldsymbol{f} = \boldsymbol{F}\boldsymbol{f}_0 \quad \text{and} \quad \boldsymbol{f}' = \boldsymbol{F}\boldsymbol{f}'_0. \tag{5.24}$$

The Lagrangian structure tensors are defined as

$$\boldsymbol{A} = \boldsymbol{f}_0 \otimes \boldsymbol{f}_0 \quad \text{and} \quad \boldsymbol{A}' = \boldsymbol{f}'_0 \otimes \boldsymbol{f}'_0, \tag{5.25}$$

and we can express their Eulerian counterparts as

$$\boldsymbol{A}_f = \boldsymbol{f} \otimes \boldsymbol{f} \quad \text{and} \quad \boldsymbol{A}'_f = \boldsymbol{f}' \otimes \boldsymbol{f}'. \tag{5.26}$$

Then the invariants, that are employed to define the response of the anisotropic part, are given as

$$I_4 = \boldsymbol{f} \cdot \boldsymbol{g}\boldsymbol{f} \qquad \text{and} \quad I_6 = \boldsymbol{f}' \cdot \boldsymbol{g}\boldsymbol{f}', \tag{5.27}$$

which measure the squares of stretches along the two fiber families. Following, the anisotropic structure tensor $\boldsymbol{\mathcal{L}}$, defined in equation 3.13, is rewritten in a form that

$$\boldsymbol{\mathcal{L}} = l^2(\boldsymbol{I} + \omega_{\mathrm{f}_0}\boldsymbol{f}_0 \otimes \boldsymbol{f}_0 + \omega'_{\mathrm{f}_0}\boldsymbol{f}'_0 \otimes \boldsymbol{f}'_0), \tag{5.28}$$

which aligns the crack evolution in the direction of fibers by use of anisotropy parameters ω_{f_0} and ω'_{f_0}. These parameters regulate the geometric anisotropy for the crack topology by dispersing the length scale parameter anisotropically over the domain, see Figure 3.7.

The anisotropic free energy part which is defined for UD FRP composites can be rearranged in a form that contains the both fiber families as following

$$\Psi_0^{ani}(\boldsymbol{g}, \boldsymbol{F}, \boldsymbol{A}_f, \boldsymbol{A}'_f) := \hat{\Psi}_0^{\mathrm{ani}}(I_4) + \hat{\Psi}_0^{\mathrm{ani}}(I_6) = \frac{\mu_{\mathrm{f}}}{4}(I_4 - 1)^2 + \frac{\mu'_{\mathrm{f}}}{4}(I_6 - 1)^2, \tag{5.29}$$

where μ_{f} and μ'_{f} stand for the stress-like parameters associated with two different fiber families.

The anisotropic part of the dimensionless crack driving source term is modified in to the form given below

$$\overline{\mathcal{H}}^{\mathrm{ani}} = \frac{\hat{\Psi}_0^{\mathrm{ani}}(I_4)}{g_{\mathrm{c}}^{\mathrm{ani}}/l} + \frac{\hat{\Psi}_0^{\mathrm{ani}}(I_6)}{g_{\mathrm{c}}'^{\mathrm{ani}}/l}, \tag{5.30}$$

where $g_{\mathrm{c}}^{\mathrm{ani}}$ and $g_{\mathrm{c}}'^{\mathrm{ani}}$ are the critical fracture energies of the two fiber families. For identical fiber families, the crack driving source term simplify to

$$\overline{\mathcal{H}}^{\mathrm{ani}} = \frac{\hat{\Psi}_0^{\mathrm{ani}}(I_4) + \hat{\Psi}_0^{\mathrm{ani}}(I_6)}{g_{\mathrm{c}}^{\mathrm{ani}}/l}, \tag{5.31}$$

Table 5.1: General structure of the constitutive model in Eulerian configuration

1. *Free energy function*

$$\Psi = g(d)[\Psi_0^{\text{iso}}(J, I_1) + \Psi_0^{ani}(I_4)]$$
$$\Psi_0^{\text{iso}}(J, I_1) := \frac{\lambda}{2}(\ln J)^2 + \frac{\mu}{2}(I_1 - 2\ln J - 3)$$
$$\Psi_0^{\text{ani}}(I_4) := \frac{\mu_{\text{f}}}{4}(I_4 - 1)^2$$
$$g(d) = (1-d)^2 \quad J = det\boldsymbol{F} \quad I_1 = \text{tr}[\boldsymbol{b}] \quad \boldsymbol{b} = \boldsymbol{F}\boldsymbol{G}^{-1}\boldsymbol{F}^T\boldsymbol{C} \quad I_4 = \boldsymbol{f}\cdot\boldsymbol{g}\boldsymbol{f}$$

2. *Define* isotropic and anisotropic stresses

   i) Isotropic stress

$$\boldsymbol{\tau}_0^{\text{iso}} = 2\partial_{\boldsymbol{g}}\Psi_0^{\text{iso}} = 2\lambda\ln J\frac{1}{J}\partial_{\boldsymbol{g}}J + \mu(\partial_{\boldsymbol{g}}I_1 - 2\frac{1}{J}\partial_{\boldsymbol{g}}J)$$
$$\boldsymbol{\tau}_0^{\text{iso}} = \lambda\ln J\boldsymbol{g}^{-1} + \mu(\boldsymbol{b} - \boldsymbol{g}^{-1})$$
$$\frac{\partial(*)}{\partial\boldsymbol{g}} = \boldsymbol{F}\frac{\partial(*)}{\partial\boldsymbol{C}}F^T \quad \partial_{\boldsymbol{g}}J = \frac{1}{2}J\boldsymbol{g}^{-1} \quad \partial_{\boldsymbol{g}}I_1 = \boldsymbol{b}$$

   ii) Anisotropic stress

$$\boldsymbol{\tau}_0^{\text{ani}} = 2\partial_{\boldsymbol{g}}\Psi_0^{\text{ani}} = \mu_{\text{f}}(I_4 - 1)\partial_{\boldsymbol{g}}I_4$$
$$\boldsymbol{\tau}_0^{\text{ani}} = 2\psi_4\boldsymbol{f}\otimes\boldsymbol{f}$$
$$\partial_{\boldsymbol{g}}I_4 = \boldsymbol{f}\otimes\boldsymbol{f}$$

3. *Sum* up isotropic and anisotropic stresses

$$\boldsymbol{\tau}_0 = \boldsymbol{\tau}_0^{\text{iso}} + \boldsymbol{\tau}_0^{\text{ani}}$$
$$\boldsymbol{\tau} = g(d)\boldsymbol{\tau}_0$$

4. *Define* isotropic and anisotropic tangent moduli

   i) Isotropic tangent modulus

$$\mathbb{C}_0^{\text{iso}} = 4\partial^2_{\boldsymbol{gg}}\Psi_0^{\text{iso}} = 2\partial_{\boldsymbol{g}}\tau_0^{\text{iso}} = 2\lambda\frac{1}{J}\partial_{\boldsymbol{g}}J\boldsymbol{g}^{-1} + 2\lambda\ln J\partial_{\boldsymbol{g}}\boldsymbol{g}^{-1} + 2\mu(\partial_{\boldsymbol{g}}\boldsymbol{b} - \partial_{\boldsymbol{g}}\boldsymbol{g}^{-1})$$
$$\mathbb{C}_0^{\text{iso}} = \lambda\boldsymbol{g}^{-1}\otimes\boldsymbol{g}^{-1} + 2(\mu - \lambda\ln J)\mathbb{I}_{\boldsymbol{g}^{-1}}$$
$$-\partial_{\boldsymbol{g}}\boldsymbol{g}^{-1} = \mathbb{I}_{\boldsymbol{g}^{-1}} \quad \partial_{\boldsymbol{g}}\boldsymbol{b} = 0$$

   ii) Anisotropic tangent modulus

$$\mathbb{C}_0^{\text{ani}} = 4\partial^2_{\boldsymbol{gg}}\Psi_0^{\text{ani}} = 2\partial_{\boldsymbol{g}}\tau_0^{\text{ani}} = 2\mu_{\text{f}}\partial_{\boldsymbol{g}}I_4\boldsymbol{f}\otimes\boldsymbol{f}$$
$$\mathbb{C}_0^{\text{ani}} = 4\psi_{44}\mathbb{M}$$
$$\mathbb{M} := \boldsymbol{f}\otimes\boldsymbol{f}\otimes\boldsymbol{f}\otimes\boldsymbol{f}$$

5. *Sum* up isotropic and anisotropic moduli

$$\mathbb{C}_0 = \mathbb{C}_0^{\text{iso}} + \mathbb{C}_0^{\text{ani}}$$
$$\mathbb{C} = g(d)\mathbb{C}_0$$

CHAPTER 6

REPRESENTATIVE NUMERICAL EXAMPLES

In this chapter we demonstrate the utility of the proposed diffusive fracture model for FRP composites. For all examples, we first determine the material parameters by fitting them to the experimental data (curve fitting), then we perform the finite element analysis with the boundary and loading conditions of the respective problem. As a simulation tool we utilize the finite element program FEAP [18].

The proposed model is capable of capturing anisotropic fracture, which is illustrated for a spectrum of benchmark problems such as single edge–notched specimens with various fiber orientations subjected to Mode–I and Mode–II loadings. Although the strain levels remain small until the onset of cracking, the finite strain version of the theory is adopted in order to consider (i) the geometrical nonlinearities during the crack propagation phase, and (ii) the large strains observed around the crack tip. Additionally a (more) realistic test case of a UD laminate with an initial notch undergoing MMB is examined with two different mode mixture. In this example influence of anisotropy parameter ω_{f_0} is checked out on force-displacement response and also on the crack path. Finally, the transverse loading test case of a CFRP beam with $[0_5/90_3]_s$ configuration is considered. The beam is fixed at both ends and by the application of transverse load, it is exposed to shear forces that causes diagonal cracks in 90^o layup, and delamination at lower and upper interface. Analyses are inspected in detail to understand the crack initiations and the crack path, and compared with the test results. For this case, interfaces are modelled between the different orientation layups. Sensitivity of the crack path to phase–field parameters of the ply and the interface is examined with the repetitive computations of varying parameters.

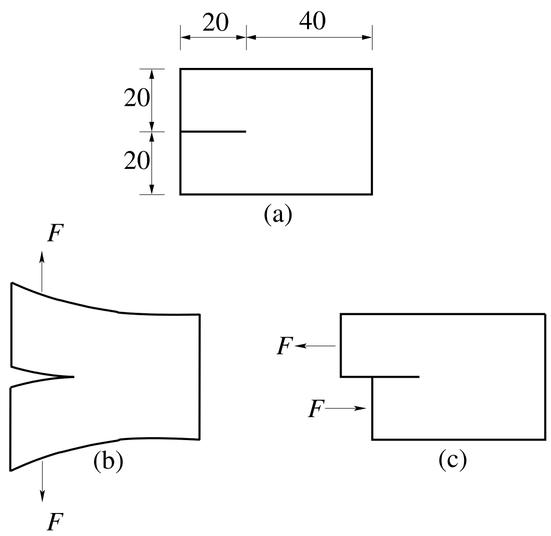

Figure 6.1: Single edge–notched specimen with Mode–I and Mode–II loading: (a) dimensions of the specimen with a notch; (b) Mode–I load case; (c) Mode–II load case. All dimensions are in millimeter.

6.1 Mode–I and Mode–II Tests for Single Edge–Notched Specimens with Various Fiber Orientations

A rectangular plate is considered with a horizontal notch placed in the middle of its height starting from the left edge. The dimensions of the specimen with the notch together with the Mode–I and Mode–II load cases are depicted in Figure 6.1. For a discretization with 15 000 standard displacement finite elements, an element size of $h = 0.4\,\mathrm{mm}$ is used over the whole domain and the length–scale parameter l is chosen to be 2.5 times the element size. For the analysis, the plane strain assumption is used, and only one element spans the thickness of the plate and it is constrained at positive and negative z direction . The anisotropy parameter ω_{f_0} is set to unity.

The material is chosen to be a UD AS4/3501-6 epoxy lamina with the (reference) fiber direction $[\boldsymbol{f}_0] = [1, 0, 0]$ (horizontal fibers). In order to test how the proposed framework captures experimental data, we make use of a set of data provided by Soden et al. [51], and simulate the model response at a single Gauss point from which the model parameters are obtained. To obtain the model parameters we use two test cases of the material; one is the tension in fiber direction and the other is the compression in transverse direction to fibers. Elasticity parameters of the material are determined

Table 6.1: Model parameters λ, μ, μ_f, $g_\mathrm{c}^\mathrm{iso}$ and $g_\mathrm{c}^\mathrm{ani}$ with related values and units.

Parameter	Value	Unit	Parameter	Value	Unit
λ	5.2×10^3	[MPa]	μ	4.04×10^3	[MPa]
μ_f	64.6×10^3	[MPa]	$g_\mathrm{c}^\mathrm{iso}$	5.5	[MPa mm]
$g_\mathrm{c}^\mathrm{ani}$	80.0	[MPa mm]	$\boldsymbol{f}_0$	$[1, 0, 0]$	[–]
l_ani	1	[mm]	l_iso	1	[mm]

from the slope of the stress–strain curves, while the isotropic and anisotropic phase–field parameters are obtained from the peak values of these curves. For the related values and units see Table 6.1. Figure 6.2 compares the model results with the experimental data of the AS4/3501-6 epoxy lamina. The numerical results agree favorably with the experimental data both under tensile and compressive loads, a gradually diminishing mechanical response under compression is observed upon reaching the ultimate stress value.

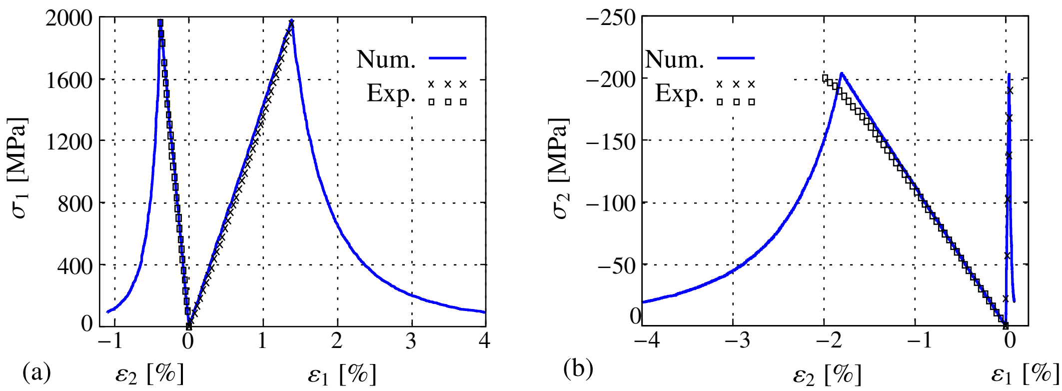

Figure 6.2: Numerical prediction versus experimental data for an AS4/3501-6 epoxy lamina – stress σ versus strain ε in the 1 (horizontal) and 2 (vertical) direction: (a) tension in the 1 direction; (b) compression in the 2 direction.

The analyses for the Mode–I and Mode–II tests are now conducted for six different fiber angles namely 0°, 15°, 30°, 45°, 60° and 90° (measured from the horizontal direction), which are shown in Figure 6.3. In the Mode–I test, an incremental load is applied at the beginning for every specimen to find out the node–specific displacements, which are considered as the node–specific displacement increments during the rest of the analysis, thereby retaining the smoothness of the surfaces on which the

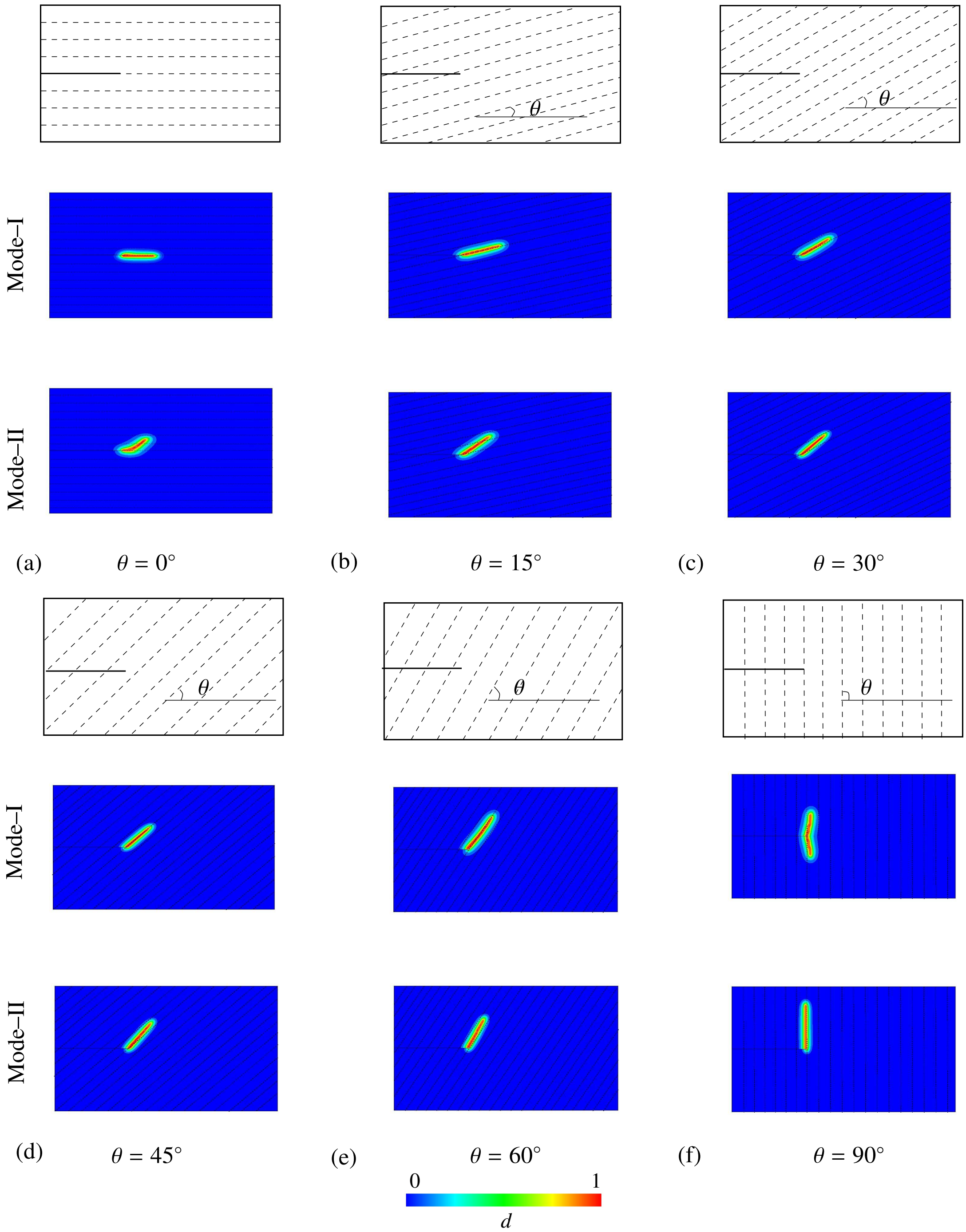

Figure 6.3: Evolution of the crack phase–field d for Mode–I and Mode–II tests in single edge–notched specimens with different fiber angles θ: (a) $\theta = 0°$; (b) $\theta = 15°$; (c) $\theta = 30°$; (d) $\theta = 45°$; (e) $\theta = 60°$; (f) $\theta = 90°$.

displacements are exerted. As for Mode–II the computations are performed with constant displacement increments. The crack patterns pertaining to Mode–I and Mode–II are illustrated in Figure 6.3, in which it can be seen that the propagation of the crack mostly follows the orientation of the fibers for all cases simulated.

The respective load–displacement curves are depicted in Figure 6.4. The curves attributed to Mode–I (M1) suggest that a 0° fiber angle exhibits the highest stiffness response, while a 90° fiber angle experiences the highest strength. Part of the reason for such a distinct behavior may be that the flanks of the domain act, in a sense, as a cantilever beam under bending due to Mode–I, thereby leading to a higher stiffness value for the fiber orientation characterized by 0° degree. As for a 90° fiber angle, the branching of the crack upon the onset probably causes the highest strength among the cases tested. However, both the stiffness and strength values are in favor of the 0° fiber angle when it comes to the Mode–II (M2) test. The crack needs to rupture more fibers on its way for a unit vertical distance.

Influence of element size h

In order to understand influence of the element size on the results, we perform additional Mode-I analyses with 0° fiber orientation by changing the mesh size around the tip of the horizontal notch, while keeping the length scale parameter constant. Analyses are conducted for five different element sizes h= 0.3, 0.2, 0.1, and 0.05. Material properties of the specimens are same as AS4/3501-6 epoxy lamina properties. For each case, the length scale parameter is set to $l = 0.6$, so that the condition $l \geq 2h$ is satisfied for all the cases. Figure 6.5 shows the related force–displacement curves of the analyses, the results starts to converge as mesh size reaches 0.1 where $l/h = 6$ around the notch tip. For the case $h = 0.3$ ($l/h = 2$) results are not very far from the converged results, and also there can be a little overshoot of failure load due to the chosen time step size.

6.2 Mixed–Mode Bending Test of a UD CFRP Beam

In this example the emphasis is on a thin rectangular CFRP with a notch in the middle subject to MMB. The information regarding the test apparatus, test procedure and the results are obtained from Crews & Reeder [14] and Naghipour et al. [43]. In MMB, the delamination of the CFRP occurs under combined influence of normal (Mode–I)

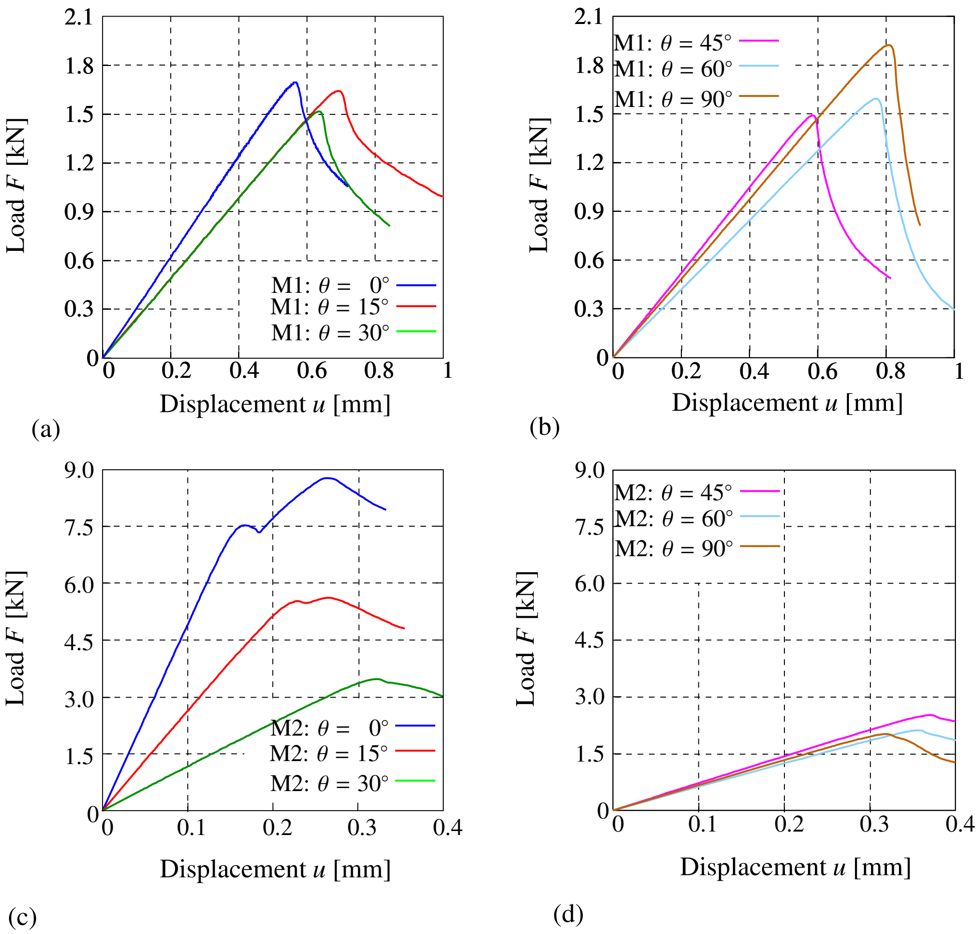

Figure 6.4: Relationships between load F and displacement u for Mode–I (M1) and Mode–II (M2) tests on single edge–notched specimens with various fiber angles, namely θ = 0°, 15°, 30°, 45°, 60° and 90°: (a),(b) Mode–I; (c),(d) Mode–II.

and shear/sliding (Mode–II) stresses. MMB tests make it possible to describe the delamination resistance of a CFRP specimen and to account for the effects of combined stresses by using a single test apparatus.

6.2.1 Problem Description

Experimental set-up and material characterization

A geometrical sketch of the MMB testing device consisting of a load F and a loading lever with length c is shown in Figure 6.6(a) in the undeformed configuration. Therein, a stands for the initial crack length (distance between the loading direction and the crack tip) acting as a delamination initiator, whereas L characterizes the spec-

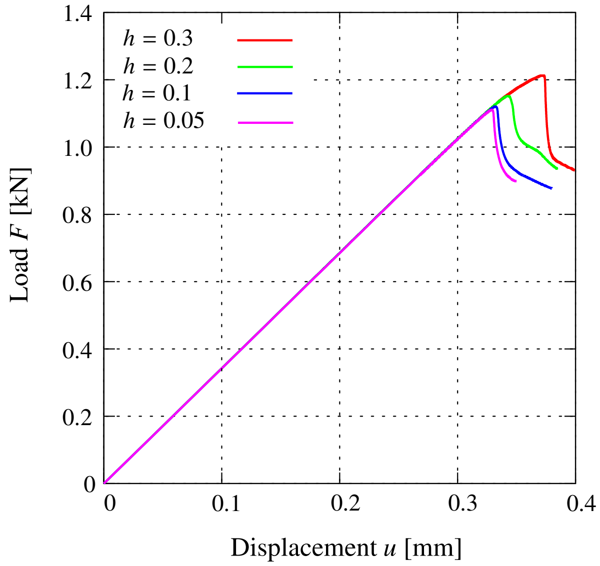

Figure 6.5: Load–displacement curves for different mesh sizes

imen half-span. In particular, the loading position c can be manipulated to generate a (pure) Mode–II loading case where F is directly above the beam mid-span ($c = 0$). By removing the loading lever and pulling up the hinge, one can achieve a (pure) Mode–I loading scenario.

A more detailed illustration of the loading acting on the hinge supports along with the superposition of the loads delineating Mode–I and Mode–II is shown in Figure 6.7.

It is worth to note that the relationship between the deflection δ_{c} at the specimen half-span, at the hinge δ_{hinge} and the total displacement δ_{MMB} that occurs at the loading point is

$$\delta_{\mathrm{MMB}} = \delta_{\mathrm{c}} + \frac{c}{L}\delta_{\mathrm{hinge}} \quad \text{with} \quad \delta_{\mathrm{hinge}} = \delta_{\mathrm{c}} + \delta_{\mathrm{Mode-I}}\,, \tag{6.1}$$

where $\delta_{\mathrm{Mode-I}}$ is the displacement at the hinge associated with Mode–I loading, see Figure 6.8 and for an illustration of the deformed state see Figure 6.6(b).

In accordance with the standards established by ASTM [1], Naghipour et al. [42] conducted mixed–mode experiments by using the MMB testing device set up according to Figure 6.6, and by applying a cross-head displacement rate of 0.5 mm/min. Therein, different mode mixtures were considered. The related lengths of the loading lever c for each mode mixture, namely 30% and 50%, are 98.5 mm and 65.0 mm, respectively, and the resulting load–displacement (F-δ_{MMB}) behavior of the UD layup

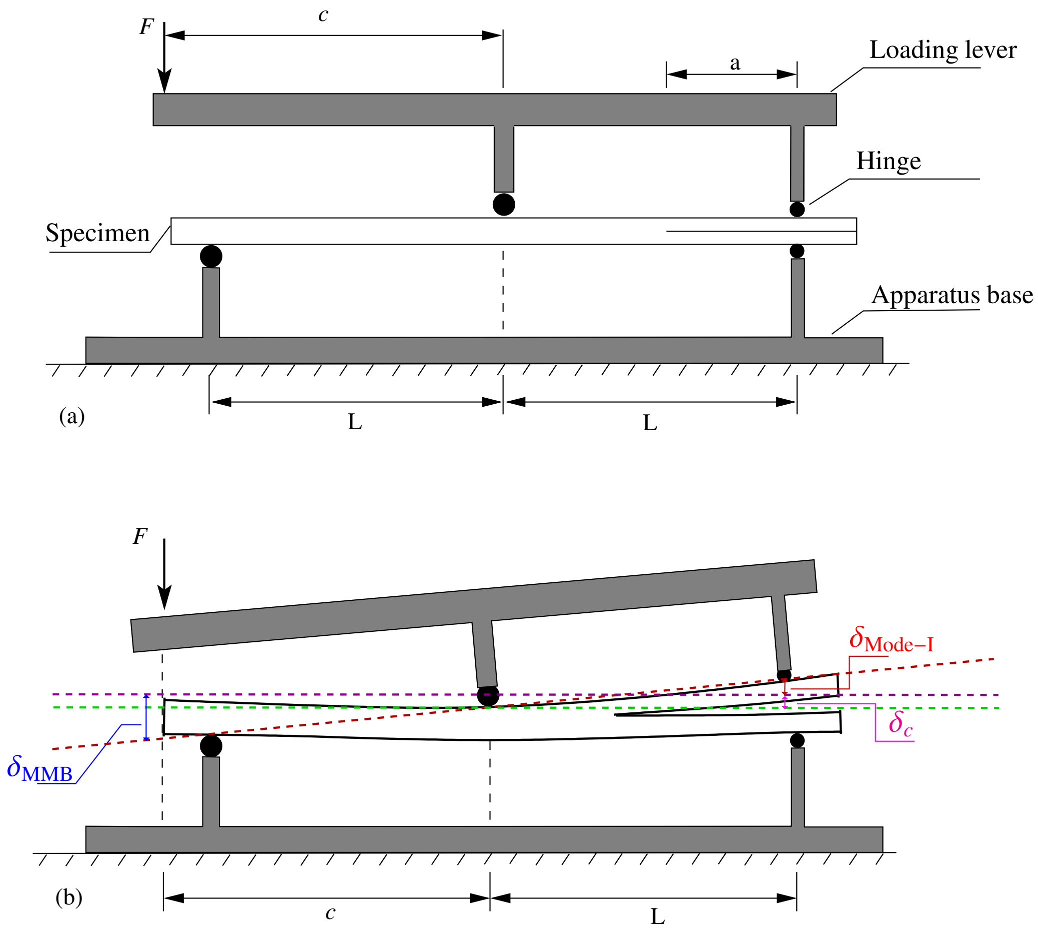

Figure 6.6: (a) Geometrical sketch of the MMB testing device with the specimen in the undeformed configuration; (b) in the deformed configuration with the corresponding displacements (reconstructed from Crews & Reeder [14].

is shown as dashed curves in Figure 6.9.

The used material for the test specimen is APC2-prepreg, which is composed of AS4-fibers (60% of the total volume) embedded in a polyether ether ketone (PEEK) matrix. Its material properties are given in Table 6.2. The material properties of the APC2 lamina are obtained at a Gauss point, which are summarized in Table 6.3, while the (reference) fiber direction is $[\boldsymbol{f}_0] = [1, 0, 0]$ (horizontal fibers). Figure 6.10 provides the fitting to the experimental data, i.e. the in–plane stress values pertaining to the fiber (horizontal) and transverse (vertical) directions, see Naghipour et al. [42].

Geometry and boundary conditions

The test specimen is composed of APC2-prepreg layers. Each prepreg layer possesses

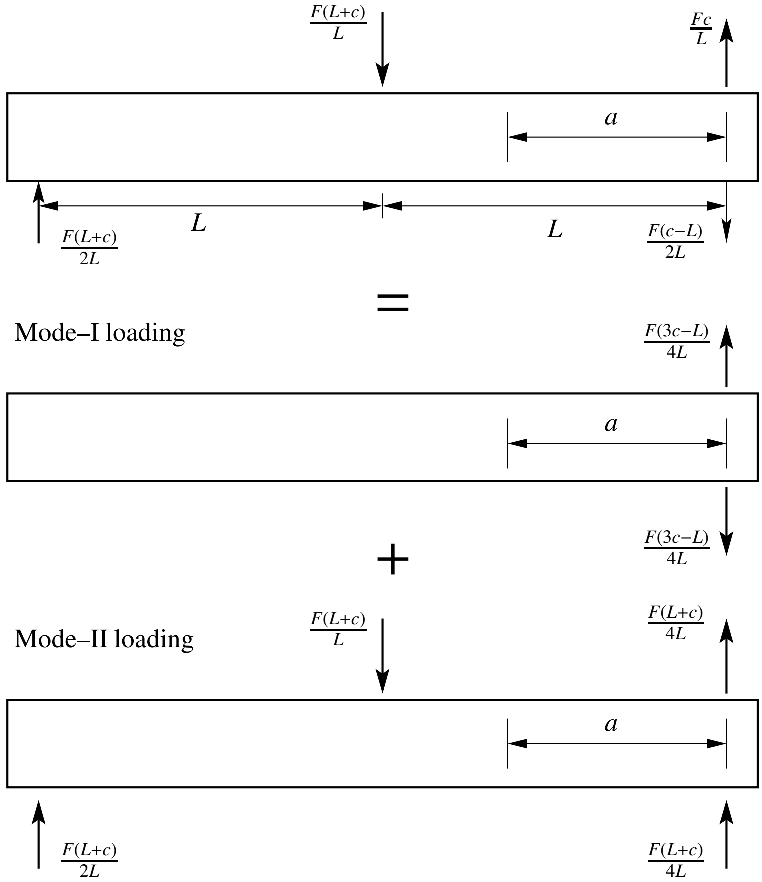

Figure 6.7: Illustration of loading of the MMB test specimen decomposed according to Mode–I and Mode–II cases (reconstructed from Crews & Reeder [14].

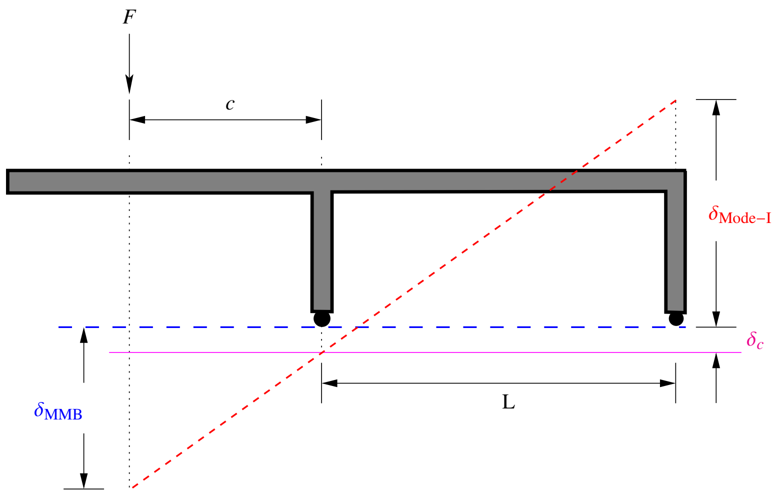

Figure 6.8: Displacements of the loading arm [42].

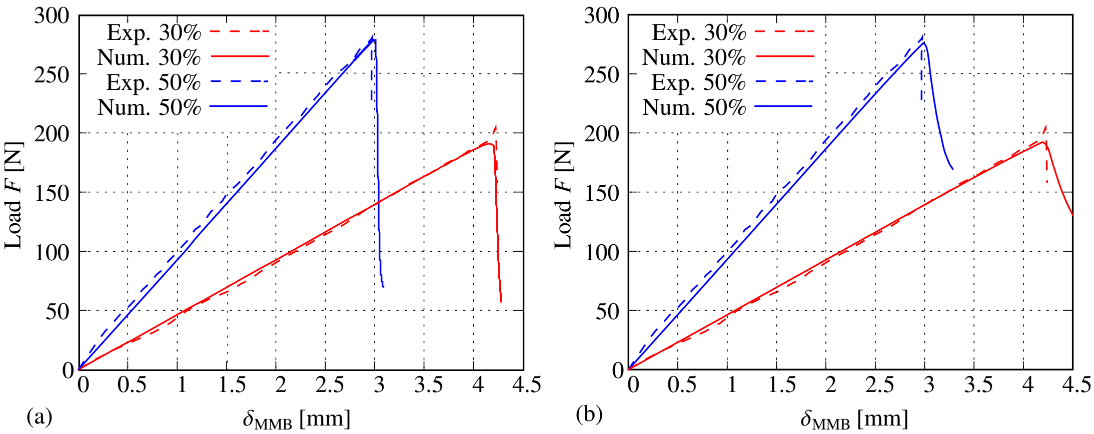

Figure 6.9: Experimental (dashed curves) and numerical (solid curves) results for the relationship between the load F and the loading point displacement δ_{MMB} for UD laminates with 30% and 50% MMs: (a) $\omega_{\mathrm{f}_0} = 1$; (b) $\omega_{\mathrm{f}_0} = 30$.

Table 6.2: Mechanical properties of an APC2 lamina (t:tension, c:compression,*is:in situ) [42]

Property	Value	Unit	Property	Value	Unit
E_{11}	138000	[MPa]	E_{22}	10500	[MPa]
ν_{12}	0.3	[–]	G_{12}	6300	[MPa]
G_{23}	3500	[MPa]	X_t	2070	[MPa]
X_c	1360	[Mpa]	Y_t, Y_t^{is}	86, 155*	[MPa]
Y_c	196	[Mpa]	S, S^{is}	147, 205.8*	[Mpa]

a thickness of 140 μm. In total, 24 carbon/PEEK UD laminae ($[0]_{24}$) are considered in the layup yielding a final specimen size of 25 mm width, 150 mm length and 3.12 mm thickness. Furthermore, a 50 mm film is placed as a delamination initiator in the mid–plane, as indicated in Figure 6.11.

In accordance with the loading descriptions characterized in Figure 6.6, an *in silico* replica of the specimen is made and then discretized. In order to better resolve the crack pattern the mesh is refined around the crack tip yielding a discretization of 6 000 brick elements with an effective element size of $h = 0.065$ mm in the refined zone. The length–scale l is considered to be 0.15 mm satisfying the empirical requirement that $l \geq 2h$. In other words, the length–scale parameter considered is greater than

Table 6.3: Model parameters λ, μ, μ_{f}, $g_{\mathrm{c}}^{\mathrm{iso}}$ and $g_{\mathrm{c}}^{\mathrm{ani}}$ of an APC2 lamina with related values and units.

Parameter	Value	Unit	Parameter	Value	Unit
λ	5.84×10^3	[MPa]	μ	3.61×10^3	[MPa]
μ_{f}	62.0×10^3	[MPa]	$g_{\mathrm{c}}^{\mathrm{iso}}$	1.82	[MPa·mm]
$g_{\mathrm{c}}^{\mathrm{ani}}$	33.0	[MPa·mm]	$\boldsymbol{f}_0$	$[1, 0, 0]$	[–]
l_{ani}	1	[mm]	l_{iso}	1	[mm]

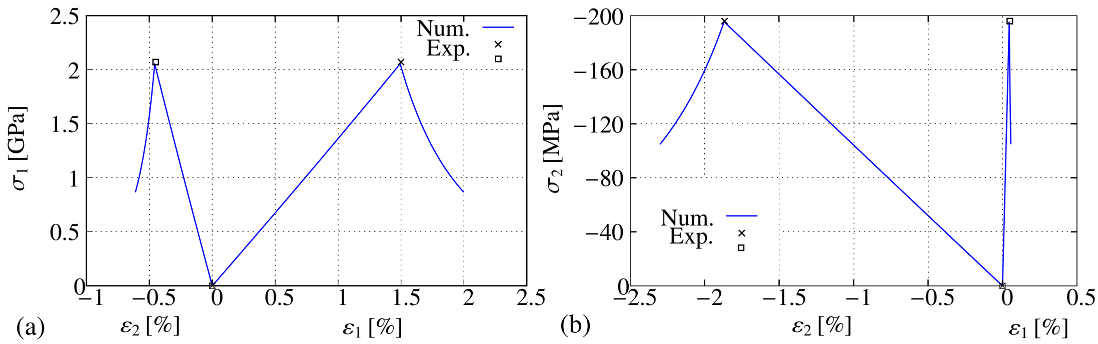

Figure 6.10: Numerical prediction versus experimental data for an APC2 lamina – stress σ versus strain ε in the 1 (horizontal) and 2 (vertical) direction: (a) tension in the 1 direction; (b) compression in the 2 direction.

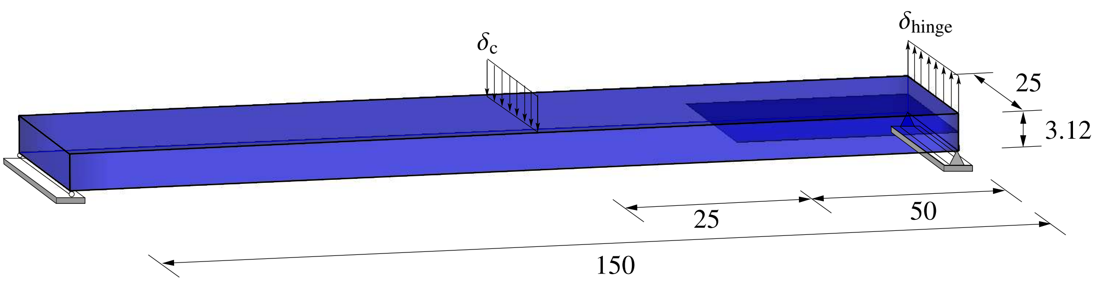

Figure 6.11: Dimensions of the specimen with a 50 mm film placed in the mid–plane serving as a delamination initiator. Also shown are the boundary conditions and displacement at the hinge and the middle of the specimen, i.e. δ_{hinge} and δ_{c}. All dimensions are in millimeters.

two times the minimum element size. Appropriate boundary conditions are applied to avoid rigid body motions, see Figure 6.11. In the analyses the plane strain assumption is applied with a single element used in the direction of the width by constraining at

Table 6.4: Lengths c, proportional loads and related displacements for each mode mixture.

Mode mixture	30%	50%
c [mm]	98.5	65.0
Hinge load [N]/displacement [mm]	1.58/2.14	1.04/1.34
Middle load [N]/displacement [mm]	2.58/1.0	2.04/1.0

positive and negative z direction. The applied load F and the chosen specimen half-span L are 1 N and 62.5 mm, respectively, from which the proportional loads exerted on the specimen are calculated. Afterwards, the displacement ratios corresponding to the calculated proportional loads are ascertained, and applied at the loading points, as depicted in Fig. 6.7. The lengths c, the proportional (hinge/middle) loads and the respective displacement ratios for each mode mixture are listed in Table 6.4.

To obtain the corresponding load–displacement (F–δ_{MMB}) curve from the points on which the loads are applied, the values of the displacements at the hinge δ_{hinge} and the middle δ_{c} of the specimen together with the related reaction forces are stored during each analysis. The applied load F is then calculated via the balance of moment with respect to the mid–point of the lever, i.e. $F = F_{\mathrm{hinge}}L/c$, for every time increment, where F_{hinge} is the reaction force at the hinge. In addition, equation 6.1 is exploited so as to compute the corresponding values of δ_{MMB}.

6.2.2 Results and Discussion

As a matter of fact, the analyses are carried out displacement–driven. The loading speed is 5 mm/min with the time increment $\Delta t = 0.5$ that runs until the onset of the macro–crack. From this point onward, the time increment is reduced to $\Delta t = 0.05$, which is followed by $\Delta t = 0.005$ during the crack propagation. The influence of time increment Δt is shown in Figure 6.12. Using large time steps causes the crack's starting point to be overshoot, so, at crack onset Δt should be taken as small as possible. The time step chosen should lead to an accurate and convergent result without sacrificing too much from computation time.

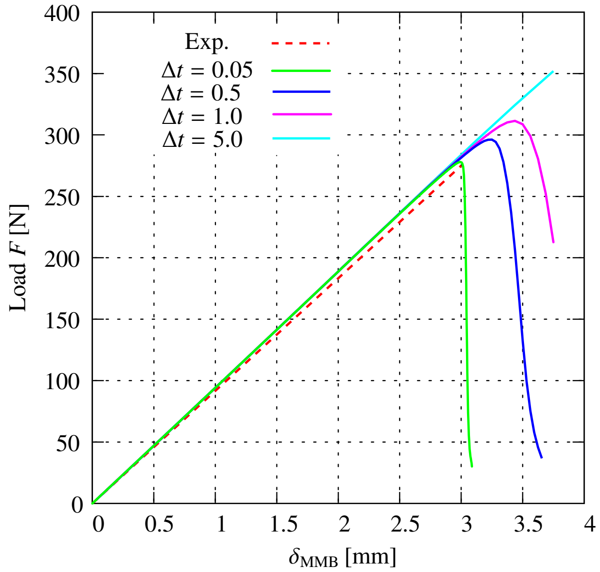

Figure 6.12: Force-displacement curve with respect to large and small time increments, and the influence of Δt on the crack initiation.

The anisotropic phase–field approach is examined for UD composite laminates by comparing the experimental data with the finite element results for the two different mode mixtures namely 30% and 50%, see Figure 6.9(a), where a slight anisotropy is incorporated into the phase–field model ($\omega_{\mathrm{f}_0} = 1$). A close examination indicates an agreement between the experimental and numerical results for the two mode mixture. The largely linear initial response of the UD laminate precedes with a rather abrupt decline, leading the fracture process zone to grow. The growth shows an inclined pattern towards the top of the specimen while rupturing several laminae on its way, as presented in Figure 6.13(a).

As following, sensitivity analyses are performed to determine the influence of the phase–field approach parameters on crack path and on load bearing capacity.

Influence of ω_{f_0}

To assess the influence of ω_{f_0} to evolution of damage and to the crack path, for the case of mode mixture 30% repeated analyses are performed with varying ω_{f_0} values. As shown in the Figure 6.14, increase of ω_{f_0} forces the crack to become parallel to the fiber direction so that cross–fiber cracking is suppressed and the failure mode is transformed from bridging (see Figure 1.1) to matrix cracking (see Figure 1.2). On

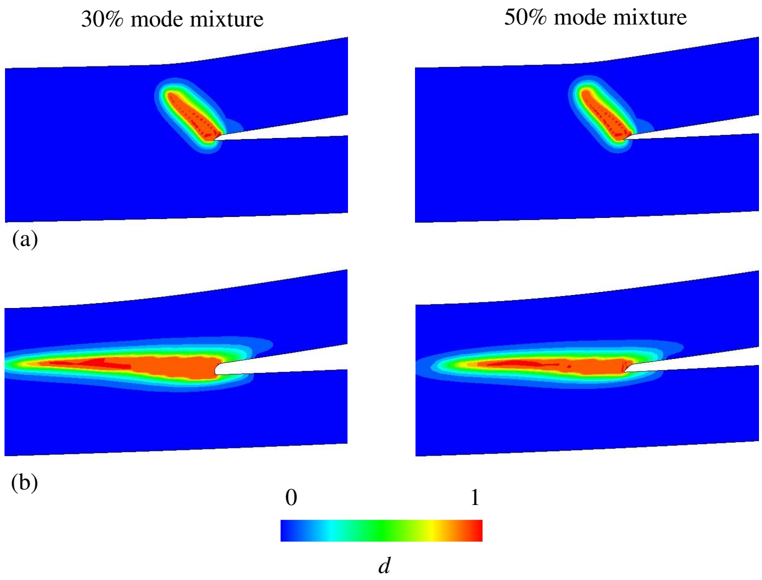

Figure 6.13: Evolution of the crack phase–field d with respect to the mode mixture of 30% (left panels) and 50% (right panels) for two anisotropy parameters: (a) $\omega_{\mathrm{f}_0} = 1$; (b) $\omega_{\mathrm{f}_0} = 30$.

the other hand, damage affected zone expands with the increase of ω_{f_0}, and then at very high ω_{f_0} values, which means very high anisotropic geometric resistance, the evolution of the crack becomes parallel to the fiber, and the damage affected zone begins to shrink relatively. The crack path, which changes depending on ω_{f_0}, also affects the force-displacement curve. As the force-displacement graphs in Figure 6.15 are examined, it is detected that as the amount of intervention to the direction of the crack increases, the amount of force needed for damage evolution increases. Also it is noticed that multiplication of the crack path which is seen for the case $\omega_{\mathrm{f}_0} = 5$, significantly increases the force required for crack formation so that the failure load for $\omega_{\mathrm{f}_0} = 5$ is greater than failure load for $\omega_{\mathrm{f}_0} = 15$.

Influence of $g_{\mathrm{c}}^{\mathrm{iso}}$ and $g_{\mathrm{c}}^{\mathrm{ani}}$

To demonstrate the effects of $g_{\mathrm{c}}^{\mathrm{iso}}$ and $g_{\mathrm{c}}^{\mathrm{ani}}$ for analysis with very high anisotropic geometric resistance, additional computations were performed for mode mixture 30% with $\omega_{\mathrm{f}_0} = 30$ by varying $g_{\mathrm{c}}^{\mathrm{iso}}$ and $g_{\mathrm{c}}^{\mathrm{ani}}$. Figure 6.16(b) shows the influence of $g_{\mathrm{c}}^{\mathrm{ani}}$ on the crack pattern, where lower $g_{\mathrm{c}}^{\mathrm{ani}}$ causes crack path changes and the evolution of the new crack path, resulting in increased force for fracture, see Figure 6.16(a). However, as depicted in Figure 6.17 calculations with different $g_{\mathrm{c}}^{\mathrm{iso}}$ values showed a direct

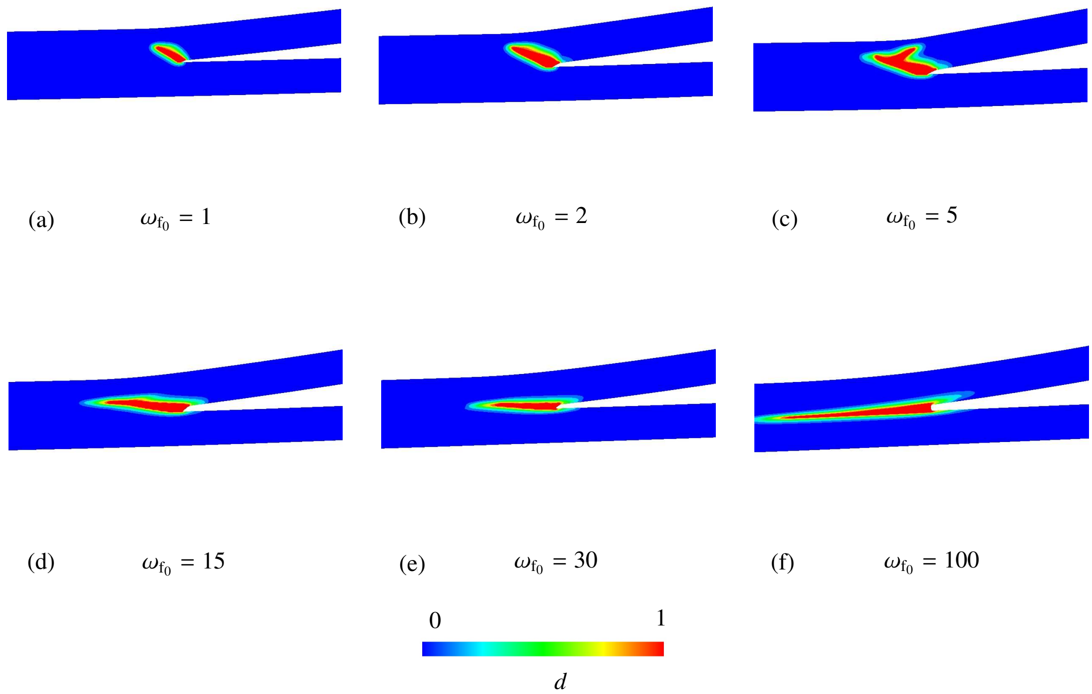

Figure 6.14: Effect of ω_{f_0} to evolution of the crack phase–field d is examined for the case of mode mixture 30% (a) $\omega_{f_0} = 1$; (b) $\omega_{f_0} = 2$, (c) $\omega_{f_0} = 5$, (d) $\omega_{f_0} = 15$, (e) $\omega_{f_0} = 30$, (f) $\omega_{f_0} = 100$

relationship between g_c^{iso} and the failure load. The main reason for this relationship is that, in cases of high anisotropic geometric resistance the crack is a matrix crack and with the decrease of g_c^{iso}, the force required for fracture starts to decrease. For this problem $g_c^{iso} = 0.73$ gives the best fit to experiment result, see Figure 6.17. With this new found g_c^{iso} value we conduct the analysis for mode mixture 50% with $\omega_{f_0} = 30$, whose force–displacement curve is given in Figure 6.9(b) and damage evolution in Figure 6.13(b).

Comparing the results of $\omega_{f_0} = 1$ and $\omega_{f_0} = 30$ for both mode mixtures namely 30% and 50%, it could be said that the simulations performed for $\omega_{f_0} = 30$ are primarily in line with those conducted for $\omega_{f_0} = 1$ during the initial phase of macro–cracking, giving rise to a sharp reduction in the load bearing capacity, as indicated in Figure 6.9(b). Nevertheless, the material tends to sustain a constant amount of load as the crack propagates further, while damaging the interlaminar medium between the lam-

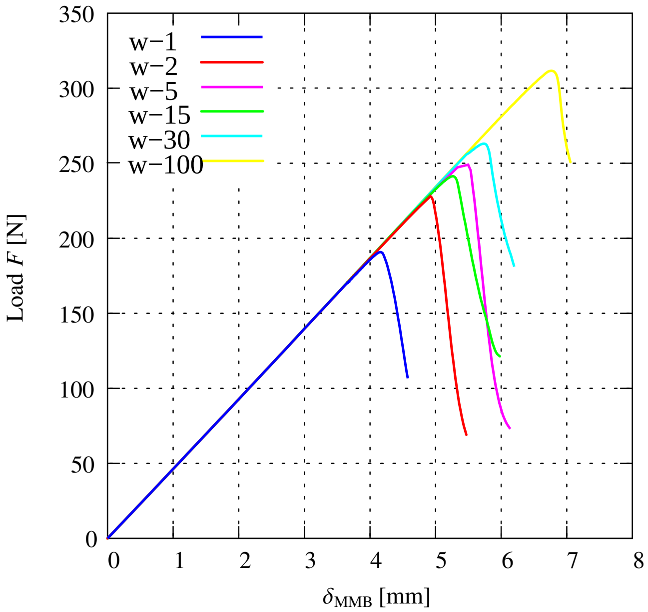

Figure 6.15: Influence of anisotropy parameter ω_{f_0} on force–displacement response. MMB case for mode mixture 30% is performed with respect to different anisotropy parameters.

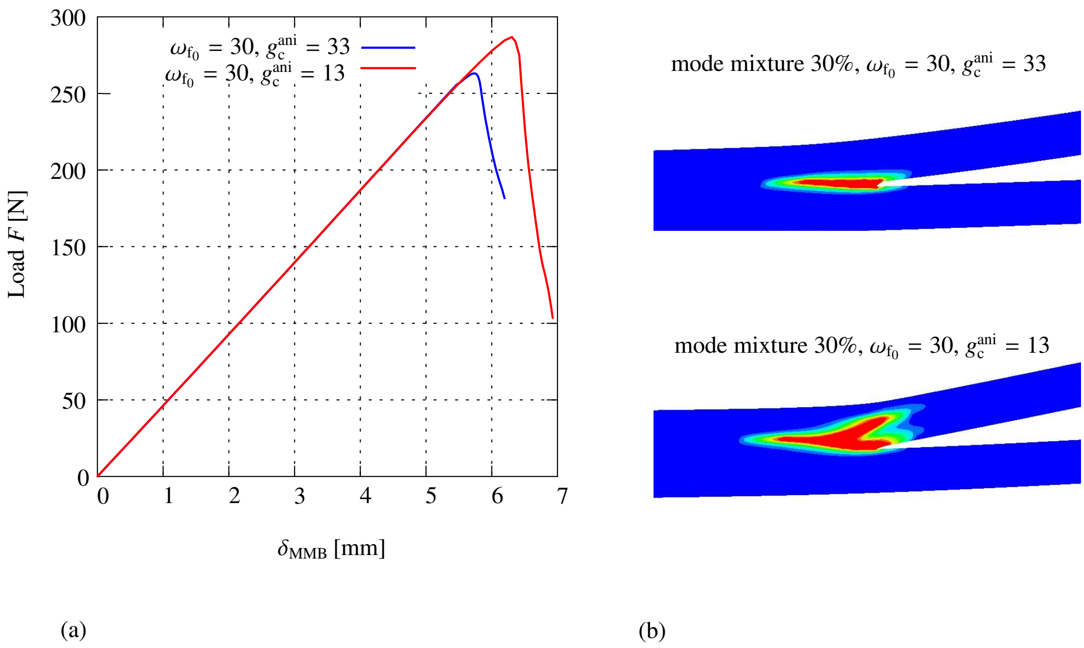

Figure 6.16: Influence of $g_{\mathrm{c}}^{\mathrm{ani}}$ for high anisotropic geometric resistance (ω_{f_0} = 30) (a) force displacement curves, (b) crack paths.

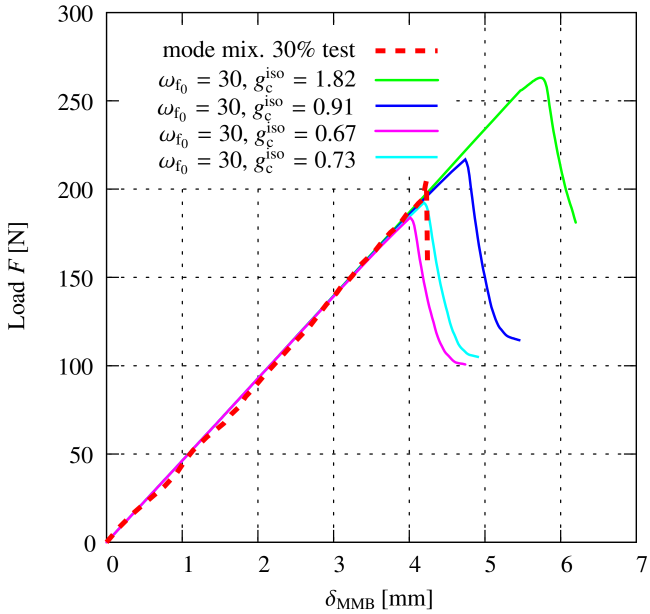

Figure 6.17: Influence of g_c^{iso} on failure load for high anisotropic geometric resistance ($\omega_{f_0} = 30$).

inae. The crack path starts to better trail the direction along which the reinforcing fibers are embedded, see Figure 6.13(b), which stands in sharp contrast to the former, i.e. $\omega_{f_0} = 1$.

If we are to assess the discrepancy created when a relatively strong anisotropic geometric resistance to cracking is assumed ($\omega_{f_0} = 30$), it is evident that the crack no longer cut across the laminae located on the top of each other, but starts to evolve at the interface between the laminae towards the right end of the specimen, thereby resembling peel tests, see, e.g., Gültekin et al. [24], where a relatively constant load drives the peeling of the specimen parallel to the fibers in the post–cracking phase. However, in the case of $\omega_{f_0} = 1$ the crack evolution is driven across the laminate until the top of the specimen, which eventually results in the failure of one of the arms. As a consequence, a more abrupt failure of the entire system occurs, which is seen in Figure 6.9(a).

6.3 Transverse Loading of a $[0_5/90_3]_s$ CFRP Beam

In this numerical example the CFRP beam in $[0_5/90_3]_s$ configuration with fixed ends is subjected to static transverse loading which causes matrix cracks in 90 degree plies and the delamination in the interfaces. The information relating the experimental setup, test procedure and the experimental results are obtained from thesis studies of Bozkurt [10].

6.3.1 Problem Description

In static loading test, the transverse load is applied to the CFRP beam by an experimental setting, which gives the opportunity to monitor side of the beam and observe the initiation and propagation of the crack sequence along with the damage formation inside the composite during transverse loading.

Experimental set-up and material characterization

A geometrical sketch of the fixture, test specimen, and the loading point is shown in Figure 6.18, where the beam is fixed at both sides by the fixtures and the load is applied by the cylindrical-head on the electromechanical testing machine controlled by displacement at a speed of 0.5mm/min.

The material of the test specimen is Hexcel 913/HTS UD prepreg, which is cured with autoclave processing after hand laid. Material properties of the Hexcel 913/HTS UD prepreg is given in Table 6.5.

The material parameters of the Hexcel 913/HTS lamina are obtained at a Gauss point by data fitting (see Figure 6.19) , which are summarized in Table 6.7, while the (reference) fiber direction is $[\boldsymbol{f}_0] = [1, 0, 0]$ (horizontal fibers), so that 1 is the horizontal, 2 is the vertical direction. And for the interface, ω_{f_0} and μ_{f} are simply set to zero, then the material parameters given in Table 6.8 are determined in similar manner by using material properties of Hexcel 913 epoxy matrix shown in Table 6.6.

Geometry and boundary conditions

In the test specimen there are 16 plies of Hexcel/3501-6 with a configuration $[0_5/90_3]_s$ yielding a final specimen size of 17 mm width, 100 mm length and 4.8 mm thickness

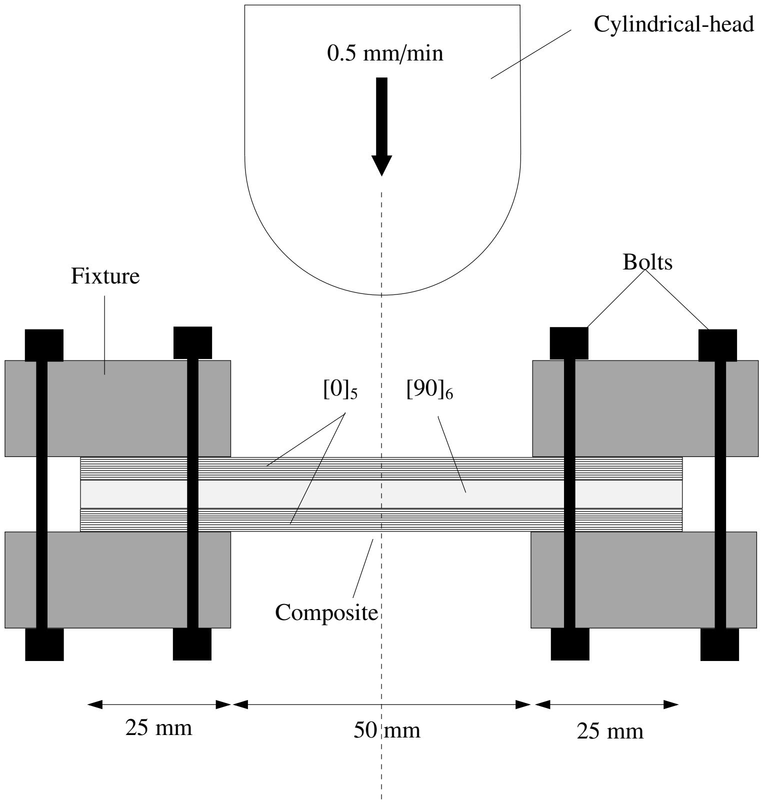

Figure 6.18: Geometrical sketch of the real fixture and the test specimen given in Bozkurt et al. [10].

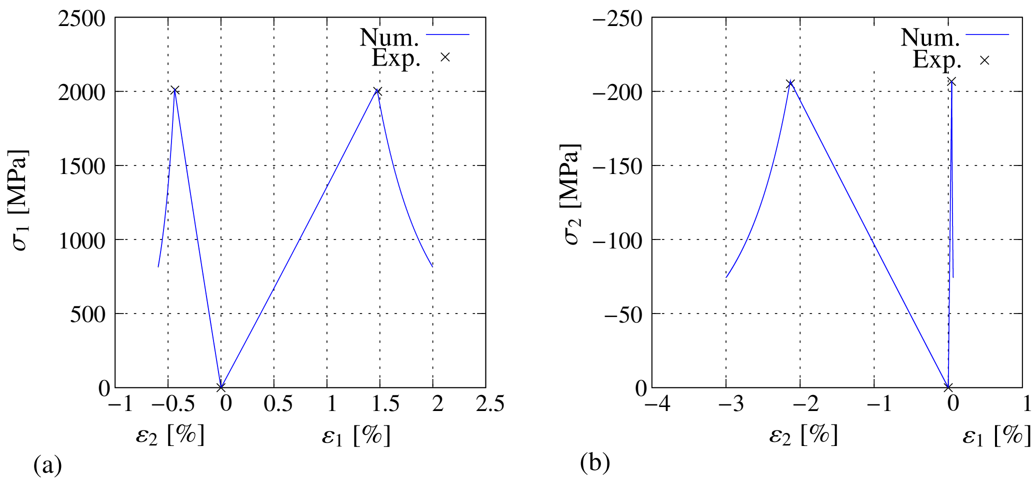

Figure 6.19: Numerical prediction versus experimental data for an Hexcel/3501-6 epoxy lamina (a) tension in the fiber direction; (b) compression in the transverse to fiber direction.

Table 6.5: Material properties of a Hexcel 913/HTS lamina with related values and units [10].

Parameter	Value	Unit	Parameter	Value	Unit
E_1	135	[GPa]	E_2	9.6	[GPa]
E_3	9.6	[GPa]	G_{12}	5.5	[GPa]
G_{13}	5.5	[GPa]	G_{23}	4.5	[GPa]
Y_T	60	[MPa]	Y_C	205	[MPa]
S_{12}	62.0	[MPa]	S_{13}	62.0	[MPa]

Table 6.6: Material properties of a Hexcel 913 epoxy with related values and units.

Property	Value	Unit
Tensile modulus	3.39	[GPa]
Tensile Strength	65.5	[MPa]

as depicted in Figure 6.20. In the test, the ends of the test sample are squeezed between the two plates, with a free area of 50 mm in the middle and the ends are fixed by tightening the bolts that attach the plates. The transverse force is applied from the middle by the cylindrical-head displacement rate of 0.5 mm/min. Force-displacement data is obtained from the load cell on the cylindrical-head.

The resulting load–displacement behavior of the $[0_5/90_3]$ layup is shown in Figure 6.21. Although the main purpose in Bozkurt's work is to provide a symmetrical de-

Table 6.7: Model parameters λ, μ, μ_f, g_c^{iso} and g_c^{ani} of a Hexcel 913/HTS lamina with related values and units.

Parameter	Value	Unit	Parameter	Value	Unit
λ	5.077×10^3	[MPa]	μ	3.384×10^3	[MPa]
μ_f	62.0×10^3	[MPa]	g_c^{iso}	2	[MPa·mm]
g_c^{ani}	24.0	[MPa·mm]	$\boldsymbol{f}_0$	$[1, 0, 0]$	[–]
l_{ani}	1	[mm]	l_{iso}	1	[mm]

Table 6.8: Model parameters λ, μ and g_c^{iso} of a Hexcel 913 epoxy with related values and units.

Parameter	Value	Unit
λ	5.476×10^3	[MPa]
μ	1.2×10^3	[MPa]
g_c^{iso}	0.62	[MPa·mm]

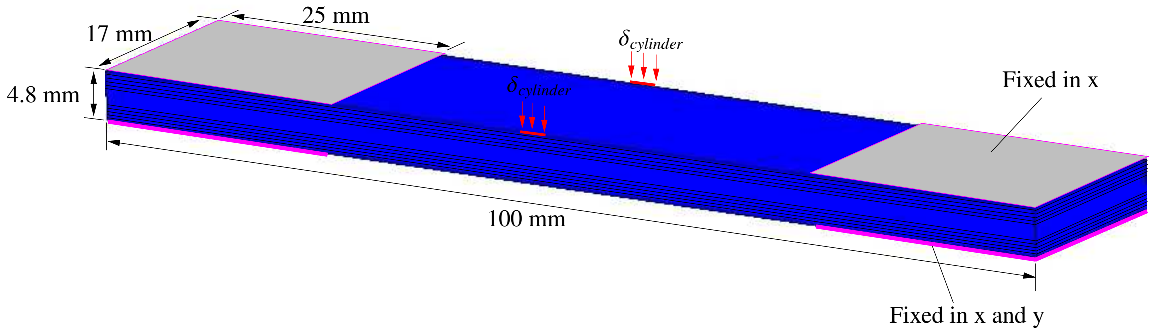

Figure 6.20: Test specimen dimensions and boundary conditions.

formation, the loading not seem to happen perfectly symmetric, and the crack formation occur at different times on the right and left side of the cylindrical head as shown in Figure 6.22. Accordingly, the force-displacement graph shows 2 peaks formed at different displacements.

In the beginning of the force–displacement curve there is a non-linear region where the stiffness is relatively low. This region may be caused due to initial gap or initial sliding of the specimen underneath the plates. To eliminate the non-linear part at the beginning of the curve, the linear part is interpolated and the starting point is moved to zero as shown in Figure 6.21.

For a discretization with 15 000 standard displacement finite elements, an element size of $h = 0.1$ mm is used in the mid portion of the beam, and interface whose thickness is taken as 0.05 mm is discretized with $h = 0.025$ mm. Higher element size is used in both ends of the beam. The length–scale parameter l is chosen to be 2.0 times the element size and taken as $l = 0.2$ mm. For the analysis, the plane

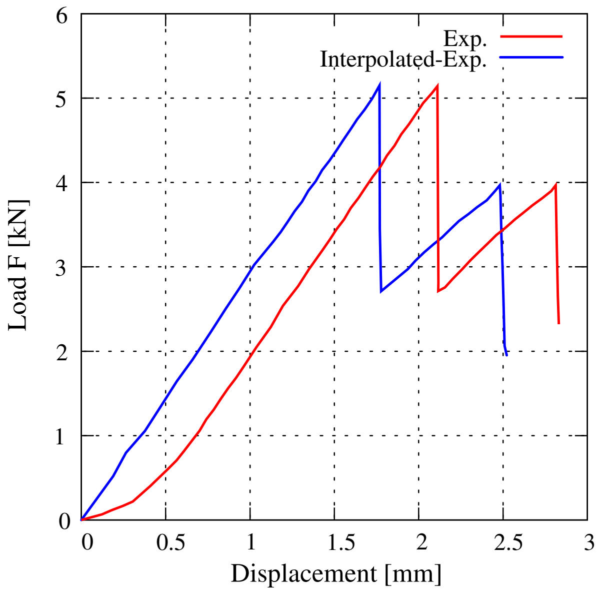

Figure 6.21: Force-displacement curve of $[0_5/90_3]$ test specimen under transverse load and the interpolated experiment curve.

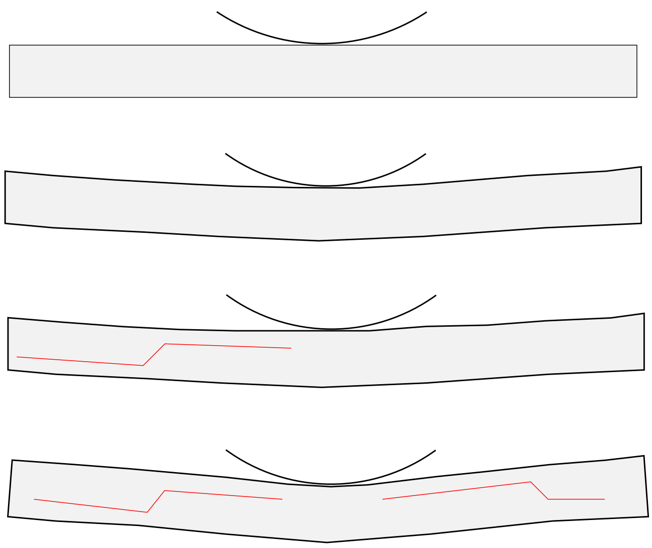

Figure 6.22: Sketch of crack formation in $[0_5/90_3]$ test specimen under transverse load based on the crack images in [10].

stress assumption is used, and only one element spans the thickness of the plate. The anisotropy parameter ω_{f_0} is set to unity. In the analysis beam is fixed in x and y directions at the lower boundary and only in x at the upper boundary as shown in Figure 6.20. Analysis is conducted displacement controlled in a same manner with the previous examples.

6.3.2 Results and Discussion

The analysis is carried out with displacement control. The loading speed is 0.5 mm / min, and the analysis is solved with a time increment of $\Delta t = 0.5$ until the damage parameter d reaches 0.05. From this point on, the time increment is reduced to $\Delta t = 0.001$ until the onset of the 45^o crack, followed by $\Delta t = 0.0001$ during crack propagation.

The first analysis gives much higher stiffness than the test results as show in Figure 6.23(a). Therefore primarily we focused on the possible causes of this difference. Bending stiffness of the beam highly depends on the end boundary conditions, the beam cross section and the beam length. In the analysis both ends are considered as fixed end, but in reality ends are squeezed between two plates with the possibility of slippage. Besides squeezing the beam can cause change in thickness. In order to take into account these possibilities, boundary conditions are relaxed by using springs in x and y directions at the fixed boundaries to satisfy the bending stiffness, the force displacement curve of the relaxed boundary conditions is given in 6.23(b). Then the second concern is the failure load. Analysis captures the failure load quite nicely but to understand the mechanism, fracture path is examined in detail. Evolution of the crack and its path is shown in Figure 6.24. Even though damage starts to evolve in the interface, the fracture ($d = 1$) happens at the lower end of the diagonal matrix crack, then interface and the matrix crack happen simultaneously. Additional computations are performed to determine the sensitivity of the failure load to critical fracture energies of the ground matrix and the interface.

Influence of interface g_c^{iso}

Analysis with relaxed boundary conditions are repeated by different values of interface critical fracture energy which is denoted as int-g_c^{iso}. Figure 6.25 shows the corresponding force–displacement curves with respect to different int-g_c^{iso}. The force required for fracture is decreased by the decrease of interface g_c^{iso} and elevated by the increase of it.

Influence of ground matrix g_c^{iso}

Figure 6.26 shows the effect of ground matrix critical fracture energy, denote as ply-

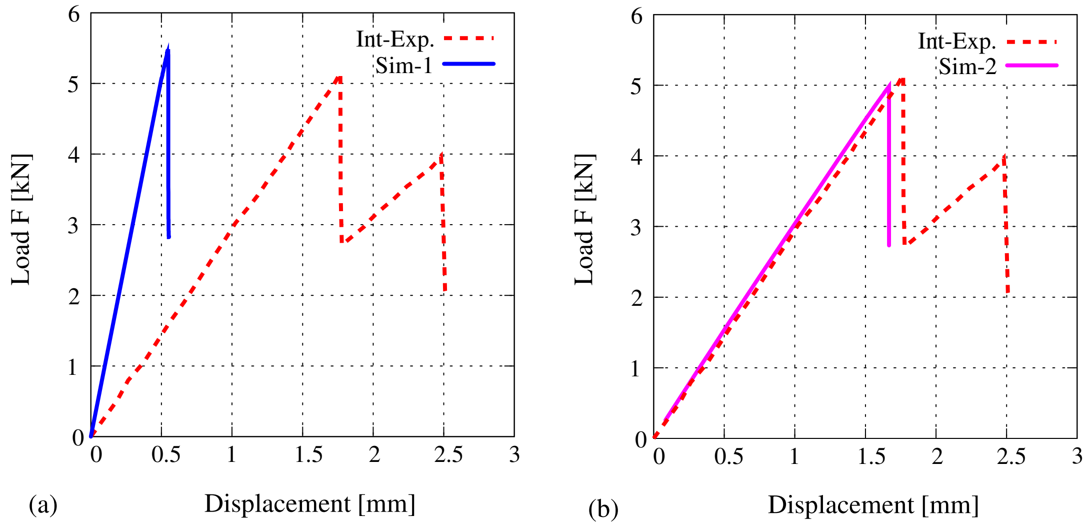

Figure 6.23: Force-displacement curve (a) simulation with fixed boundary conditions, (b) simulation with relaxed boundary conditions.

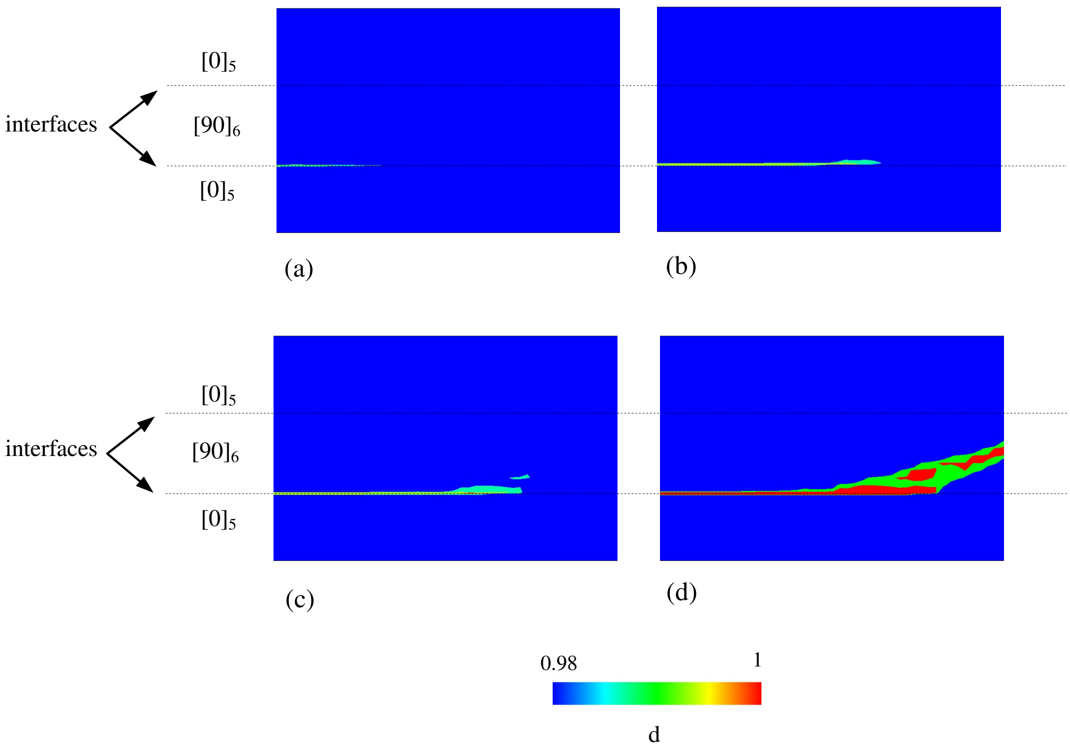

Figure 6.24: Evolution of the crack (d=1) in a sequence (a), (b), (c), (d)

g_c^{iso}, to the failure load. Although the ply-g_c^{iso} does not affect the force required for fracture, the ratio between ply-g_c^{iso} and int-g_c^{iso} affects the path and angle of the diag-

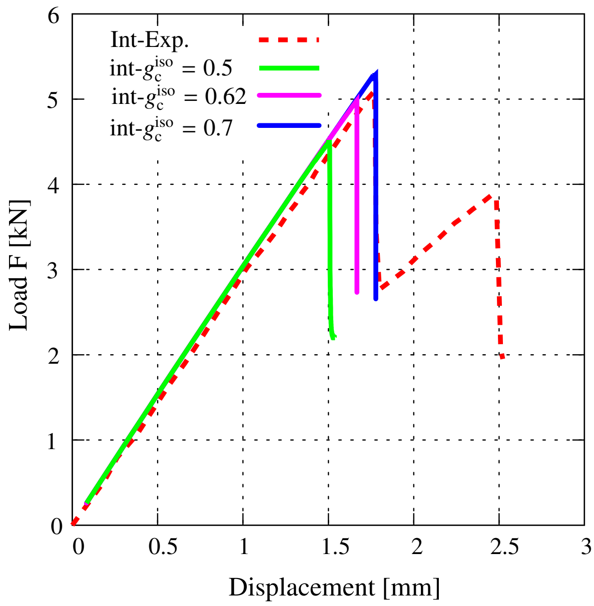

Figure 6.25: Force-displacement curve of $[0_5/90_3]$ beam with relaxed boundary conditions for different int-g_c^{iso}

onal matrix crack (see Figure 6.27).

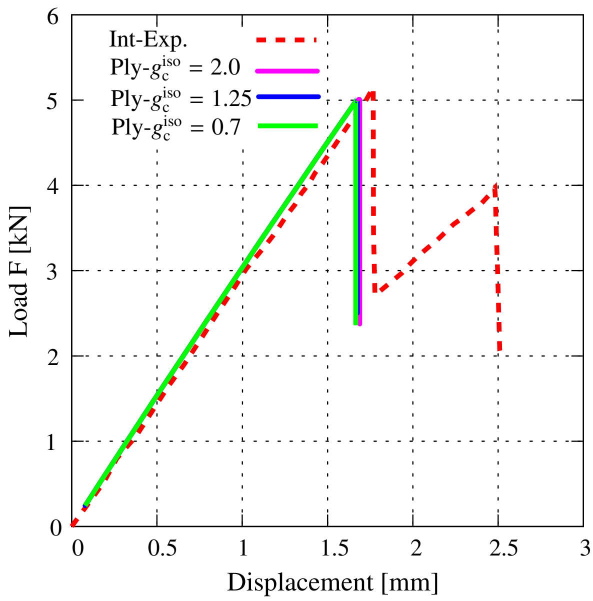

Figure 6.26: Force-displacement curve of $[0_5/90_3]$ beam with relaxed boundary conditions for different ply-g_c^{iso}

When Figure 6.27 is examined in detail, it is detected that the diagonal crack occurs

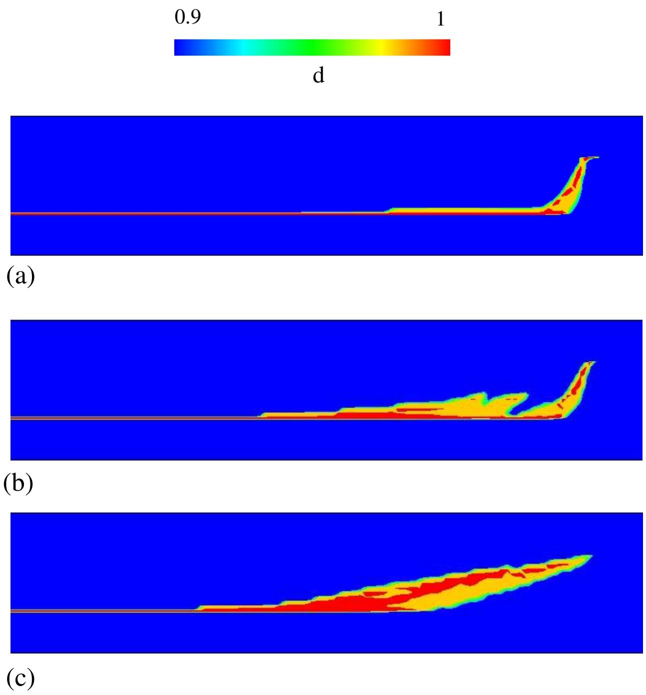

Figure 6.27: Influence of the ratio between ply-g_c^{iso} and int-g_c^{iso} to the crack path (a)Ply-g_c^{iso} = 2.0, (b)Ply-g_c^{iso} = 1.25, (c)Ply-g_c^{iso} = 0.7.

in close vicinity to the loading point, however, in the test results, it is clearly seen that the diagonal cracks occur at a certain distance from the loading point. In the analysis, the load is applied directly to the specimen without using any contact model for the cylindrical head and the composite, through a single point. This is thought to be effective in the formation of cracks close to the load application point.

The analysis is carried out with the updated ply material parameters that are given in table 6.9 and the relaxed boundary conditions ($K_x = 200, K_y = 1000$ at beam ends) that provide the best fit to the test data and give results similar to the test in terms of the shape and location of the diagonal crack. And the loading is compelled to be asymmetrical by shifting the loading axis by about 1 mm. The force-displacement curve obtained as a result of the changes is given in Figure 6.28. Curve captures quite nicely the first crack formation, the decrease in the amount of load beam can carry due to the crack, and the subsequent stiffness is consistent with the test result. However, in the analysis the second crack occurs at a higher load than the test.

The crack image resulting from the analysis is given in Figure 6.29. In the analy-

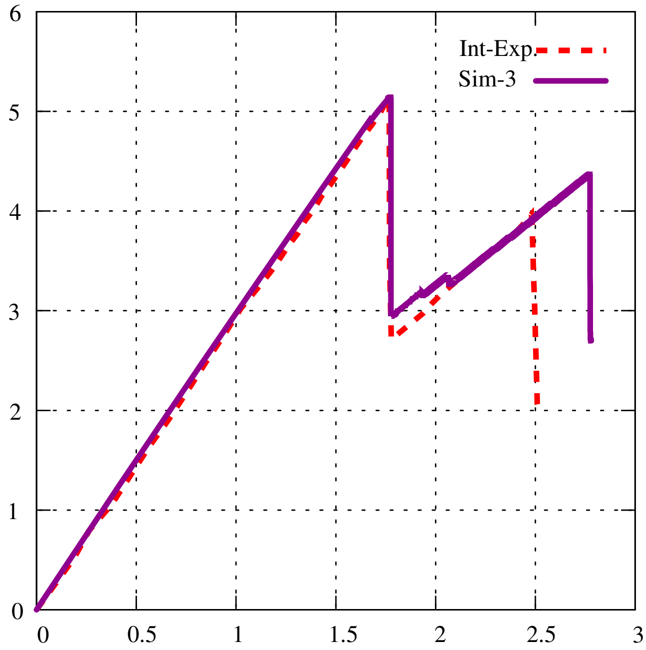

Figure 6.28: $[0_5/90_3]$ beam test data and the corresponding analysis result with relaxed boundary conditions and updated material parameters.

Table 6.9: Updated model parameters of a Hexcel 913/HTS lamina

Parameter	Value	Unit	Parameter	Value	Unit
λ	5.476×10^3	[MPa]	μ	1.2×10^3	[MPa]
μ_f	62.0×10^3	[MPa]	g_c^{iso}	2	[MPa·mm]
g_c^{ani}	24.0	[MPa·mm]	f_0	$[1, 0, 0]$	[−]

sis damage evolution begins at the lower interface, and then crack formation occurs simultaneously at the lower interface and in the 90 degree layer as diagonal crack. Later crack continues to evolve as a delamination in the upper and lower interfaces.

Even though the crack shape and the path in the analysis is very similar to the test results (see Figure 6.30) , the location of the 45 degree diagonal cracks are still closer to the load application axis compared to test results. And in the test the position of the second diagonal crack is farther from the load application axis compared to the first one. In analysis their position is nearly symmetric.

In order to determine the relation between position of the diagonal crack and the

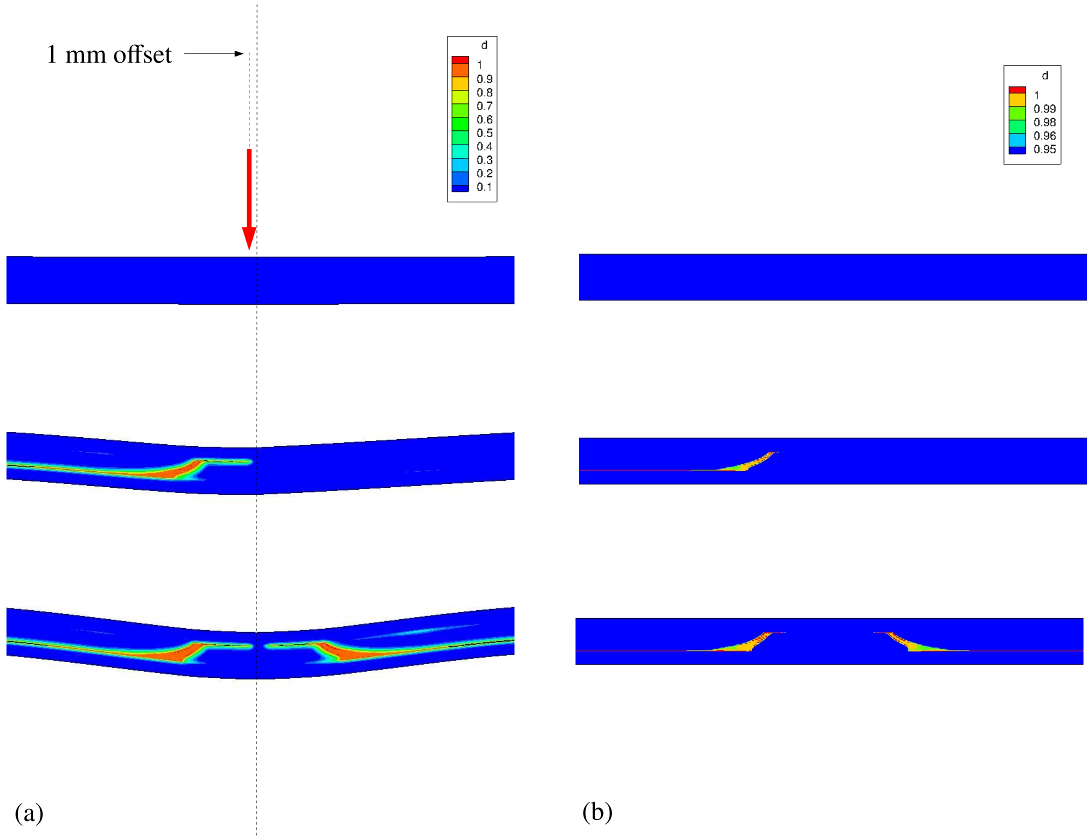

Figure 6.29: Evolution of the crack phase–field d for the asymmetric loading of the beam with 1 mm offset from the centreline. (a) deformed and (b) undeformed configuration .

amount of asymmetric loading, additional calculations are performed with increasing loading asymmetry, the result is shown in Figure 6.31. Although the location of the first diagonal crack does not change, the location and shape of the second diagonal crack have been found to be significantly affected by the amount of asymmetry of the loading.

Consequently, it could be said that the analysis gives promisingly good results with respect to test data, since we had to make some assumptions about the boundary conditions and the material parameters due to unknowns of the test conditions. To have more satisfactory results we need to have more information about the geometry and boundary conditions of the beam during the test.

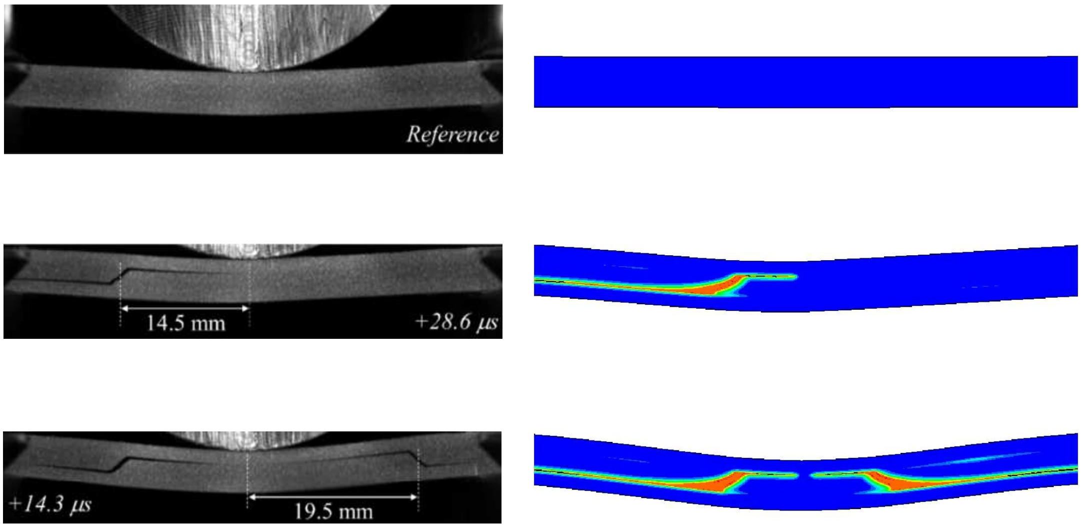

(a) (b)

Figure 6.30: Comparison with the real test results (a) test results from Bozkurt [10], (b) analysis results in the deformed configuration.

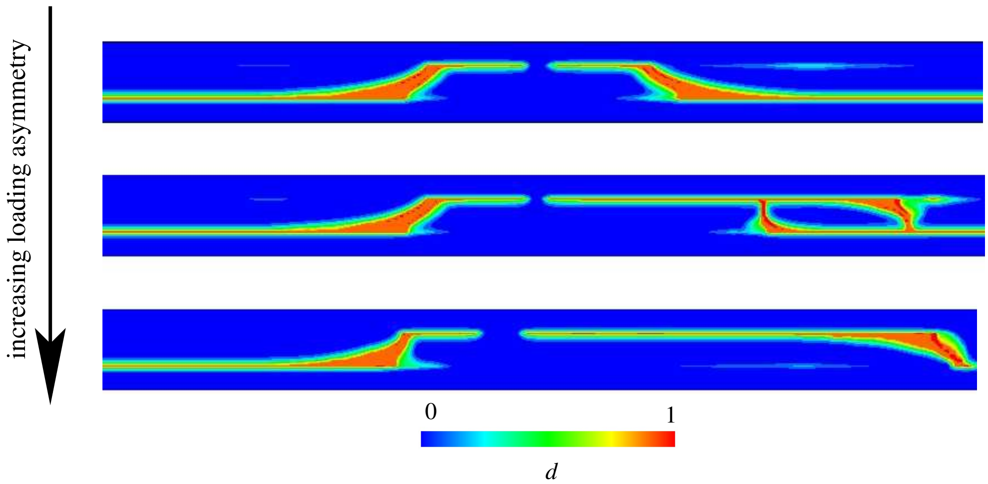

Figure 6.31: Evolution of the diagonal crack in relation with the increasing asymmetric loading.

CHAPTER 7

CONCLUDING REMARKS

This thesis presents the first attempt to model failure of engineered composite materials by making use of an anisotropic crack phase–field approach. A concise yet critical outline of previous contributions pertaining to strength–based and energy–based criteria for failure of composites is given. Subsequently, the basics of continuum mechanics and the kinematics of the mechanical field of the problem is defined. Then, the theoretical backbones of the anisotropic phase–field approach is reviewed along with the governing equations of the anisotropic fracture and the related constitutive equations of the multi–field problem. Energy based anisotropic failure criterion which relies on the superposition of the distinct fracture processes associated with the matrix and fibrous content, is described. The phase–field model of fracture is essentially modular consisting of two sub–problems emanating from the deformation field $\boldsymbol{\varphi}$ and the crack phase–field d.

The numerical examples and the discussions focus on the crack initiation via fitting to experimental data and the direction on which the crack finds its path through relevant tests, such as Mode–I, Mode–II, MMB and transverse loading of a beam. In particular, the first example scrutinizes the anisotropic fracture of a single–edged notch plate in response to Mode–I and Mode–II loadings by altering the orientation of fibers, while the second example offers an analysis of a UD CFRP laminate under MMB, touching upon different fracture zones in relation to the anisotropy parameter. The last example considers transverse loading of a composite beam having different ply orientations. Even though the quantitative results are obtained by relaxing the boundary conditions, this example is particularly important in terms of crack formation, shear induced diagonal matrix cracks in 90 degree layers, and the capture of delamination occurring between the layers in different orientation.

It is noteworthy that the fit of the anisotropic model with relatively few number of parameters shows a satisfactory coherence with experimental data. The proposed model serves a sound basis for more advanced analyses of crack initiation and propagation in UD FRP composites. However, some difficulties were also encountered in the analysis. Especially modelling the interface with very small elements negatively affected the analysis and lead to very long computation time. Therefore, it becomes important to integrate cohesive elements into the phase field model to be able to analyse more complex geometries. To have accurate and convergent results, the time step at the crack onset should be taken as small as possible and very small element size should be employed in the crack zones. Since the phase field can easily catch the branching of the crack and the changes of the crack path, the crack may evolve in a direction which is not predicted before and enter a coarsely meshed zone. In such cases, the model may need to be re-meshed in order to satisfy l / h ratio. In order to cope with all these difficulties, it is important to combine the automatic time stepping with the h-adaptive schemes, and activate the parallel processing in FEAP with the usage of high performance hpc cluster that will increase the solution speed.

As a final remark, our third example, which is the transverse loading of a composite beam, is a dynamic problem even if the loading is done at a very low speed. Although analyses are performed by the assumption that the problem is static, the inertias of the cylindrical head and composite beam are likely to affect the test results. Thus ,as a future-work, the code can be expanded to dynamic problems.

REFERENCES

[1] ASTM International. ASTM D6671-01 standards test method for mixed mode I–mode II interlaminar fracture toughness of unidirectional fiber reinforced polymer matrix composites. *ASTM International*, West Conshohocken, PA, USA, 2001.

[2] R. Alessi and F. Freddi. Phase-field modelling of failure in hybrid laminates. *Composite Structures*, 181:9–25, 2017.

[3] M. Ambati, T. Gerasimov and L. De Lorenzis. Phase–field modeling of ductile fracture. *Comput. Mech.*, 55:1017–1040, 2015.

[4] A. Arteiro, G. Catalanotti, J. Reinoso, P. Linde and P. P. Camanho. Simulation of the mechanical response of thin-ply composites: from computational micromechanics to structural analysis. *Arch. Comput. Meth. Engrg.*, 26:1445–1487, 2019.

[5] A. S. Argon. Fracture of composites. *Treatise Mater. Sci. Technol.*, 1:79–114, 1972.

[6] V. D. Azzi and S. W. Tsai. Anisotropic strength of composites. *Exp Mech.*, 5:283–288, 1965.

[7] J. Betten. Formulation of anisotropic constitutive equations. In J. P. Boehler (ed.), Applications of Tensor Functions in Solid Mechanics Springer-Verlag, Wien, CISM Courses and Lectures no. 292, 228–250, 1987.

[8] M. J. Borden, T. J. R. Hughes, C. M. Landis and A. Anvari. A phase–field formulation for fracture in ductile materials: Finite deformation balance law derivation, plastic degradation, and stress triaxiality effects. *Comput. Meth. Appl. Mech. Engrg.* 312:130–166, 2016.

[9] J. P. Boehler. A simple derivation of representations for non-polynomial con-

stitutive equations in some cases of anisotropy. *ZAMM – Zeitschrift für Angewandte Mathematik und Mechanik*, 59:157–167, 1979.

[10] M. O. Bozkurt. *Experimental and numerical investigation of damage induced by tranverse impact in composite beams an plates.* MSc.Thesis, Middle East Technical University, 2019.

[11] J. W. Cahn and J. E. Hilliard. Free energy of a nonuniform system. I. Interfacial free energy. *J. Chem. Phys.*, 28:258–267, 1958.

[12] American Chemistry Council. Plastics and Polymer Composites Technology Roadmap for Automotive Markets. March 2014

[13] J. D. Clayton and J. Knap. Phase field modeling of directional fracture in anisotropic polycrystals. *Comput. Mat. Sci.*, 98:158–169, 2015.

[14] J. H. Crews and J. R. Reeder. A mixed–mode bending apparatus for delamination testing. *NASA TM 100662*, 1988.

[15] R.G. Cuntze. Efficient 3D and 2D failure conditions for UD laminae and their application within the verification of the laminate design. *Compos. Sci. and Tech.*, 66:1081–1096, 2006.

[16] H. Dal, O. Gültekin, F. A. Denli and G. A. Holzapfel. Phase–field models for the failure of anisotropic continua. *Proc. Appl. Math. Mech.*, 17: 91–94, 2017.

[17] F. A. Denli, O. Gültekin, G. A. Holzapfel and H. Dal. A phase-field model for fracture of unidirectional fiber-reinforced polymer matrix composites. *Comput. Meth. Appl. Mech. Engrg.*, 65:1149–1166, 2020.

[18] R. L. Taylor. FEAP–Finite Element Analysis Program. *http://www.ce.berkeley/feap* , University of California, Berkeley, 2014.

[19] G. A. Francfort and J.-J. Marigo. Revisiting brittle fracture as an energy minimization problem. *J. Mech. Phys. Solids*, 46:1319–1342, 1998.

[20] E. Ghassemieh. Materials in Automotive Application, State of the Art and Prospects. University of Sheffield, UK, 2011.

[21] A. A. Griffith. The phenomena of rupture and flow in solids. *Philos. T. Roy. Soc. A*, 221:163–197, 1921.

[22] D. M. Grogan, S. B. Leen and C. M. Ó Brádaigh. An XFEM-based methodology for fatigue delamination and permeability of composites. *Composite Structures*, 107:205–218, 2014.

[23] O. Gültekin, H. Dal and G. A. Holzapfel. A phase-field approach to model fracture of arterial walls: Theory and finite element analysis. *Comput. Meth. Appl. Mech. Engrg.*, 312:542–566, 2016.

[24] O. Gültekin, H. Dal and G. A. Holzapfel. Numerical aspects of failure in soft biological tissues favor energy-based criteria: A Rate-dependent anisotropic crack phase–field model. *Comput. Meth. Appl. Mech. Engrg.*, 331:23–52, 2018.

[25] Z. Hashin. Failure criteria for unidirectional fiber composites. *J. Appl. Mech.*, 47:329–334, 1980.

[26] Z. Hashin. Finite thermoelastic fracture criterion with application to laminate cracking analysis. *J. Mech. Phys. Solids*, 44:1129–1145, 1996.

[27] R. Hill. *The mathematical theory of Plasticity*. New York: Oxford University Press, 1998.

[28] G. A. Holzapfel. *Nonlinear Solid Mechanics. A Continuum Approach for Engineering*. John Wiley & Sons, Chichester, 2000.

[29] G. A. Holzapfel, T. C. Gasser and R. W. Ogden. A new constitutive framework for arterial wall mechanics and a comparative study of material models. *J. Elasticity*, 61:1–48, 2000.

[30] L. Hollaway *Handbook of ploymer composites for engineers* Woodhead Publishing Ltd, Cambridge, England, 1994.

[31] B. Li, C. Peco and D. Millán, I. Arias and M. Arroyo. Phase-field modeling and simulation of fracture in brittle materials with strongly anisotropic surface energy. *Int. J. Numer. Meth. Engng.*, 102:711–727, 2015.

[32] P. K .Mallick. *Fiber-Reinforced Composites, Materials, Manufacturing, and Design*. Department of Mechanical Engineering University of Michigan-Dearborn, Michigan, Third Edition, 2007.

[33] J. E. Marsden and T. J. R. Hughes. *Mathematical Foundations of Elasticity*. Dover, New York, 1994.

[34] C. Miehe, F. Welschinger and M. Hofacker. Thermodynamically consistent phase-field models of fracture: Variational principles and multi-field FE implementations. *Int. J. Numer. Meth. Engng.*, 83:1273–1311, 2010.

[35] C. Miehe, M. Hofacker and F. Welschinger. A phase field model for rate-independent crack propagation: Robust algorithmic implementation based on operator splits. *Comput. Meth. Appl. Mech. Engrg.*, 199:2765–2778, 2010.

[36] C. Miehe, L. M. Schänzel and H. Ulmer. Phase field modeling of fracture in multi-physics problems. Part I. Balance of crack surface and failure criteria for brittle crack propagation in thermo-elastic solid. *Comput. Meth. Appl. Mech. Engrg.*, 294:449–485, 2015.

[37] C. Miehe, M. Hofacker, L. M. Schänzel and F. Aldakheel. Phase field modeling of fracture in multi-physics problems. Part II. Coupled brittle-to-ductile failure criteria and crack propagation in thermo-elastic-plastic solids. *Comput. Meth. Appl. Mech. Engrg.*, 294:486–522, 2015.

[38] C. Miehe, H. Dal, L. M. Schänzel, and A. Raina. A phase-field model for chemo-mechanical induced fracture in lithium-ion battery electrode particles. *Int. J. Numer. Meth. Engng.*, 106:683–711, 2016.

[39] R. von Mises. Mechanik der festen Körper im plastisch deformablen Zustand. *Göttin. Nachr. Math. Phys.*, 1:582–592, 1913.

[40] J. A. Nairn. The strain-energy release rate of composite microcracking–a variational approach. *J. Compos. Mater.*, 23:1106–1129, 1989.

[41] P. Naghipour, M. Bartsh and H. Voggenreiter. Simulation and experimental validation of mixed mode delamination in multidirectional CF/PEEK laminates under fatigue loading. *Int. J. Solids and Structures*, 48:1070–1081, 2011.

[42] P. Naghipour. *Numerical simulations and experimental investigations on quasi-static and cyclic mixed mode delamination of multidirectional CFRP laminates.* Ph.D. Thesis, University of Stuttgart, 2011.

[43] P. Naghipour, J. Schneider, M. Bartsch, J. Hausmann and H. Voggenreiter. Fracture simulation of CFRP laminates in mixed mode bending. *Eng. Frac. Mech.*, 76:2821–2833, 2009.

[44] T.-T. Nguyen, J. Réthéro, J. Yvonnet, and M.-C. Baietto. Multi-phase-field modeling of anisotropic crack propagation for polycrystalline materials. *Comput. Mech.*, 60:289–314, 2017.

[45] A. Puck and H. Schürmann. Failure analysis of FRP laminates by means of physically based phenomenological models. *Compos. Sci. and Tech.*, 58:1045–1067, 1998.

[46] G. Qiu and T. Pence. Remarks on the behavior of simple directionally reinforced incompressible nonlinearly elastic solids. *J. Elasticity*, 49:1–30, 1997.

[47] J. Reinoso, A. Arteiro, M. Paggi and P. P. Camanho. Strength prediction of notched thin ply laminates using finite fracture mechanics and the phase field approach. *Compos. Sci. and Tech.*, 58:205–216, 2017.

[48] V. L. Saponara, H. Muliana, G. A. Kardomateas, and R. Haj-Ali. Experimental and numerical analysis of delamination growth in double cantilever laminated beams. *Engineering Fracture Mechanics.*, 69: 687–699, 2001.

[49] C. Schreiber, C. Kuhn, and R. Müller. Phase field modeling of brittle fracture in materials with anisotropic fracture resistance. *PAMM*, 18:e201800113, 2018.

[50] J. Schröder and P. Neff. Invariant formulation of hyperelastic transverse isotropy based on polyconvex free energy functions. *Int. J. Solids Structures*, 40:401–445, 2003.

[51] P. D. Soden, M. J. Hinton and A. S. Kaddour. Lamina properties, lay-up configurations and loading conditions for a range of fibre reinforced composite laminates. In: M. Hinton, P. D. Soden and A.-S. Kaddour (eds.), Failure Criteria in Fibre–Reinforced Polymer Composites, Elsevier Ltd, 30–51, 2004.

[52] A. Spencer. *Deformations of Fibre–Reinforced Materials*. Oxford University Press, 1972.

[53] S. Teichtmeister, D. Kienle, F. Aldakheel, and M.-A. Keip. Phase-field modeling of fracture in anisotropic brittle solids. *Int. J. Non-Linear Mech.*, 97:1–21, 2017.

[54] R. Talreja and C. V. Singh. *Damage and Failure of Composite Materials*. Cambridge University Press, New York, 2012

[55] R. Talreja. Assessment of the fundamentals of failure theories for composite materials. *Compos. Sci. and Tech.*, 105:190–201, 2014.

[56] S. W. Tsai and E. M. Wu. General theory of strength for anisotropic materials. *J. Compos. Mater.*, 5:58–80, 1971.

[57] A. Turon, C. G. Dávila, P. P. Camanho and J. Costa. An engineering solution for mesh size effects in the simulation of delamination using cohesive zone models. *Eng. Frac. Mech.*, 74:1665–1682, 2007.

[58] Y. Wang and H. Waisman. Progressive delamination analysis of composite materials using XFEM and a discrete damage zone mode. *Comput. Mech.*, 55:1–26, 2015.

[59] W. E. Wolfe and T. S. Butalia. A strain-energy based failure criterion for non-linear analysis of composite laminates subjected to biaxial loading. *Compos. Sci. and Tech.*, 58:1107–1124, 1998.

[60] Q. Yang and B. Cox. Cohesive models for damage evolution in laminated composites. *Int. J. Fracture*, 133:107–137, 2005.

[61] S. Yazdani, W. J. H. Rust and P. Wriggers. An XFEM approach for modelling delamination in composite laminates. *Composite Structures*, 135:353–364, 2016.

[62] L. Zhao, Y. Gong, J. Zhang, Y. Chen and B. Fei. Simulation of delamination growth in multidirectional laminates under mode I and mixed mode I/II loadings using cohesive elements. *Composite Structures*, 116:509–522, 2016.

VITA

PERSONAL INFORMATION

Name and Surname:	Funda Aksu Denli
Nationality:	Turkish
Date of Birth:	27.07.1981
Place of Birth:	Adapazarı
Marital Status:	Married
email:	fundaaksu@gmail.com

EDUCATION

Degree	**Institution**	**Year of Graduation**
M.Sc.	Stuttgart University COMMAS	2006
B.Sc.	Marmara University Mechanical Engineering	2004
High School	Private Tansel High School	1999

EXPERIENCE

Years	**Company / Institution**	**Role**
2014-present	Roketsan A.S.-Turkey	Lead Engineer
2006-2014	FIAT-Turkey, FIAT-Italy	Senior Virtual Analysis Engineer
2005-2006	DYNAmore GmbH	M.Sc. Student and Intern

KEY PAPERS AND PRESENTATIONS

- **Aksu Denli, F.**; Gültekin, O. ; Holzapfel, G.A.; Dal, H. *A phase-field model for fracture of unidirectional fiber-reinforced polymer matrix composites*, Comput. Meth. Appl. Mech. Engrg., 65:1149–1166, 2020.
- **Aksu Denli, F.**; Dal, H.; Gültekin, O. *A Phase Field Approach to Viscoelas-*

tic Fracture in Rubbery Polymers 1st International Workshop on Plasticity, Damage and Fracture of Engineering Materials, 22-23 August 2019, Ankara, Turkey.

- Dal, H.; Badienia Y.; Açıkgöz, K.; **Aksu Denli, F.** *A comparative study on hyperelastic constitutive models on rubber: State of the art after 2006* In book: Constitutive Models for Rubber XI, 2019.

- **Aksu Denli, F.**; Dal, H. *A rate-dependent phase field approach for the failure of rubberlike materials* , 6th European Conference on Computational Mechanics, 11-15 June 2018, Glasgow, UK

- Dal, H.; Gültekin, O.; **Aksu Denli, F.**; Holzapfel, A.G. *Phase-Field Models for the Failure of Anisotropic Continua*, Proc. Appl. Math. Mech., 17: 91–94, 2017.

- Dal, H.; Badienia Y.; Açıkgöz, K.; **Aksu Denli, F.** *A Novel Parameter Identification Toolbox for the Selection of Hyperelastic Constitutive Models from Experimental Data*, Proceedings of the 7th GACM Colloquium on Computational Mechanics for Young Scientists from Academia and Industry October 11-13, 2017 in Stuttgart, Germany.